UNIVERSITÀ DEGLI STUDIO DI TORINO
Scuola di Dottorato

CHARACTERIZATION AND TEST OF LGAD STRIP SILICON DETECTORS TO COUNT THE NUMBER OF PROTONS OF THERAPEUTIC BEAMS

Omar Hammad Ali

2016-2019

Università degli Studi di Torino
Scuola di Dottorato

Dottorato in Fisica ed Astrofisica

CHARACTERIZATION AND TEST OF LGAD STRIP SILICON DETECTORS TO COUNT THE NUMBER OF PROTONS OF THERAPEUTIC BEAMS

Omar Hammad Ali

Tutor: **Prof. Vincenzo Monaco**

Reviewers: **Prof. Andrea Lavagno**
Prof. Chiara La Tessa

2016-2019

To my beloved parents, sisters and brother

Acknowledgements

I am very lucky to have been given the opportunity to work with a great group of people here at the University of Turin. I would like to express my gratitude to my supervisory, Prof. Vincenzo Monaco for his support, guidance, enlightening questions and comments.

I deeply appreciate Prof. Roberto Cirio, who consistently supported me and gave me a lot of valuable suggestions and motivations. All these years, he was an amazing director of study and a wise headman. They have been a great team to work and share moments with.

My sincere thanks also go to Prof. Roberto Sacchi, Dr. Anna Vignati, Dr. Simona Giordanengo and Dr. Federico Fausti who instructed and encouraged me on my research work.

It was an honor for me to work in projects of the Istituto Nazionale di Fisica Nucleare (INFN) especially within the MoVe-IT project, financed by the Commissione Scientifica 5 of INFN.

The work is also inserted in the activities of the Dipartimento di Eccellenza dell'Universita' di Torino.

It was a great pleasure collaborating with the UFSD group of INFN Torino CNAO, TIFPA and FBK. Thanks for the members that help and facilitate accessing to their laboratories and facilities.

I shall not conclude without thanking my loving family for being so supportive and making me happy even from a long distance.

ABSTRACT

This study is part of an INFN project called MoVe-IT (Modeling and Verification for Ion beam Treatment planning) which goal is to explore and implement the biological impact of target nuclei fragmentation, relative biological effectiveness (RBE), intra-tumor heterogeneity, in radiobiological models used in treatment planning systems (TPS) for ion beam therapy. The project includes the development of dedicated devices for dose verification, accounting for a wide range of complex physical and biological effects.
In particular, the medical physics group of Torino University and INFN is mainly involved in the development of innovative devices for online beam monitoring in radiobiological experiments. These new devices are based on solid state detectors which should overcome the limitations of ionization chambers typically used for beam monitoring in ion therapy and enhance treatment delivery in the future.

Planar gas-filled Ionization Chambers (IC) are the most commonly used detectors in radiotherapy and hadron therapy centers. They have the virtue of being partially transparent so that the incident beam can be monitored without significant degradation of the beam quality. ICs are simple, radiation-hard, and easily constructed. However, their operation is based on the collection of the charge created by the interaction of charged particles in the gas, which depends on the beam energy. The relevant information needed in a radiation therapy application is the beam fluence rate or the number of delivered particles, which can be determined by ICs only if the beam energy is known in advance and after proper calibration procedures. The charge collection time of gas detectors is relatively long, of the order of 100's of μs, preventing their use in delivery modalities with fast changes of the beam conditions. In addition, the amount of electrical charge produced in an IC by a single ionizing radiation event is very small, and the corresponding limited sensitivity of ICs does not allow to monitor low doses.

Solid state detectors are promising alternatives to overcome the limitations of ICs in terms of speed and sensitivity, as they can be used to detect single particles with fast response time and excellent spatial resolution. When employed in counting mode the number of delivered particles can be measured without the need of a prior knowledge of the beam energy or any calibration procedure. The detection of single particles and the counting of their number with the required clinical tolerance (error less than 1 %) at high fluxes can be obtained only by using fine segmented detectors with small active thickness, to keep the charge collection time and the signal duration small.

Recent developments in silicon technology have produced novel detectors (Low-Gain Avalanche Diodes, LGAD) where an additional dopant layer provides a moderate internal charge multiplication mechanism to increase the signal-to-noise ratio without affecting the dead time. The enhanced signal from LGAD sensors can compensate the reduced charge produced in thin thickness and are therefore optimal to build thin segmented detectors with short signal duration needed for particle counting applications.

This work focuses on the study of the properties of dedicated LGAD detectors segmented in strips that will be used to build a prototype device for clinical proton beam monitoring in radiobiological experiments. In particular, Ultra Fast Silicon Detectors (UFSD), i.e. LGAD sensors optimized for time resolution, are employed, Dedicated UFSD structures, a custom readout electronics and the prototype device have been designed to count the number of protons in an area of 3x3 cm^2 with fluence rates up to 10^8 $cm^{-2}s^{-1}$ with an error less than 1 %. The detectors were characterized in laboratory and with therapeutic beams. In particular their working conditions and their counting capabilities have been studied at high beam fluxes where counting inefficiencies appear due to the superposition of signals from multiple particles close in time. Algorithms based on logical correlations of signals from two sensor channels have been developed and applied to correct these counting inefficiencies at high beam rates, showing that proper segmented UFSD sensors are able to count the number of beam particles with the required precision up to a few hundreds MHz/cm^2, close to the typical particle rates employed in the clinical practice.

The results of this thesis work demonstrate the capability of solid-state detectors to be employed as beam monitoring detectors. In particular the requirements for radiobiological applications of the MoVe-IT project have been met, allowing to complete the construction of the prototype device in the next months.
Several issues are still pending for an application in the clinical practice, like the need of finer segmentations to cope with the high fluxes of therapeutic beams and the radiation hardness of LGAD sensors needed to work for a reasonable amount of time before their substitution. These aspects require further studies and technological steps, with a complexity and cost scale above the limitations of the current project.

The thesis is organized as follows:

In Chapter 1 the dose distribution modalities adopted in charged particle therapy are described, focusing in particular on the role of the Dose Distribution System (DDS) which assures that the beam irradiation follows

the prescriptions of the Treatment Planning System to guarantee a proper dose distribution. The DDS relies on online measurements of the beam direction, profile and flux obtained with beam monitoring detectors positioned along the beam direction before the patient. This chapter includes a description of solid-state detecting sensors, and of their advantages and limitation for beam monitoring in single particle counting mode. LGAD detectors are introduced.

Chapter 2 describes the LGAD strip detectors and the front-end electronics developed for a prototype of a single particle counting device, and the simulations performed within this thesis work to optimize the design of the readout electronics.

Chapter 3 contains a detailed description of the basic tests of the LGAD silicon sensors performed in laboratory, consisting of basic characterization studies preliminary to the tests on therapeutic beams.

Chapter 4 contains a description of the setup prepared to test the sensors at two treatment facilities in Italy, the Centro Nazionale di Adroterapia Oncologica (CNAO, Pavia) and the Proton Therapy Center (PTC) of TIFPA (Trento), which are partners in the MoVe-IT project. This chapter shows the results of these tests that led to a better understanding of the beam structures at the two facilities and the behavior of the UFSD sensors with therapeutic beams. The feasibility to use UFSD sensors segmented in strips for beam particle counting and the limitation in their counting capabilities are addressed.

Chapter 5 describes correction algorithms developed to mitigate counting inefficiencies at high particle fluxes due to overlapping of the signals from two particles close in time. The corrections algorithms, based on the logical correlation of signals from two neighboring strips, are first asserted with simulations and therefore applied to the data collected at CNAO and the PTC of Trento. The results show the possibility to extend the counting capability of LGAD strip detectors above the goal of the MoVe-IT project.

CONTENTS

List of figures and tables

Chapter 1

Radiotherapy with heavy charged particles

1.1. Introduction

Cancer is a significant, growing public health concern. It is already responsible for one in six deaths globally. In 2018, 18.1 million people around the world had cancer, and 9.6 million died from the disease. By 2040, those figures will nearly double [1].

The term cancer is commonly used to cover a wide range of diseases caused by an uncontrolled division of abnormal cells in a part of the body. The common feature of cancer diseases, is that cells in affected organs or tissues of the body continue to grow indefinitely, without reference to the needs of the body.as shown in Figure 1.1,

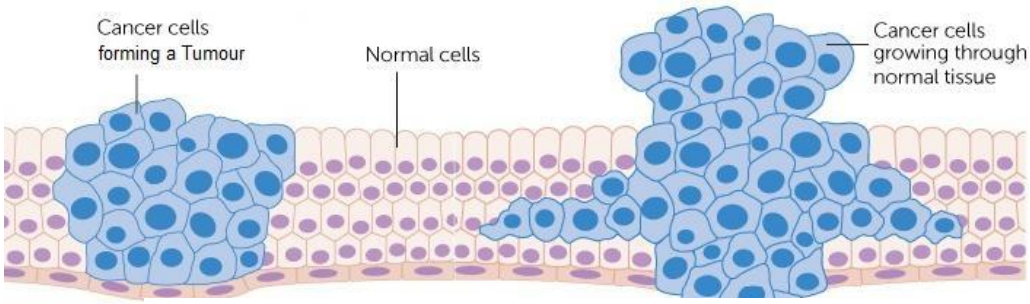

Figure 1.1 Cancer starts when cells change abnormally and their number grows in an uncontrolled mode.

Treatment can involve surgery, systemic therapy (e.g. chemotherapy, immunotherapy, endocrine therapy) and radiotherapy. As early diagnosis and treatment improve, the number of survivors will increase.

Radiation therapy is the medical use of ionizing radiation to treat cancer. High energy accelerated particles and electromagnetic waves passing through tissues will lose their energies and ionize atoms in the living cells, producing a direct damage to the DNA or indirect damage through free radicals which are capable of interacting chemically with the DNA.

Moreover, living cells are able to fix most of the damages occurring at low doses. To kill a tumor, it occurs to concentrate a high dose of radiation directly at the cancerous cells which will cause a multiple damage

specifically in the DNA. For severe damages, cells could lose their ability to fix or replicate and eventually they will die.

DNA damages affecting single nucleotides (single-strand breaks, SSB) can be repaired with high probability, while damages involving the two strands of the DNA at points less than three nucleotides apart (double-strand breaks, DBS) are more difficult to be repaired. For a given physical dose, radiation with high ionization density (for example heavy charged particles) produce more DBS damages and therefore have a higher biological effectiveness [2].

Tumors that do not respond positively to conventional radiation therapy based on high energy X-rays beams are classified as being radio-resistant. Moreover, some tumors are located very close to sensitive organs which are called organs at risks (OAR), such as the optic nerve or the spinal cord. Hadrons, as considered in this thesis, are ions accelerated to high energies in various types of accelerators. Particles have a number of potential advantages in radio therapy in particular for radioresistant tumors or tumors close to OARs [3].

1.2. Rationales and advantages of hadron therapy

Cure of tumors with protons and carbon ions presents, with respect to the conventional x-ray radiotherapy, some advantages from both the biological and physical points of view. The dose distribution of photons shows the highest energy deposition shortly after their entrance in tissues, which then decrease exponentially as the penetration depth increases. This implies that for a deep-seated tumor, a large dose is released at the entrance of the body and after the tumor.

In contrast to photons, the energy transferred to the tissue by ion beams depends on the particle speed. The more the particles slow down, the higher the energy they transfer to the tissue per track length, causing the maximum dose deposition at a certain depth. The maximum of the dose deposition in a depth dose curve is called the Bragg peak and its position depends on the initial kinetic energy (Fig. 1.2).

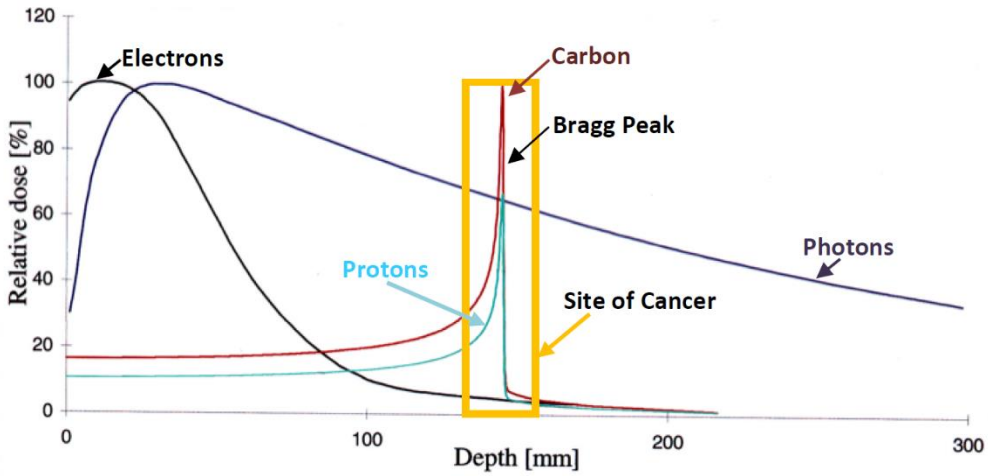

Figure1.2 Dose released by ionizing particles as a function of the depth in the tissue. The tumor location and dimensions are delimited by the yellow lines.

The specific range and the reduced lateral straggling of protons and carbon ions can be used to deliver higher doses to the tumor while reducing the doses absorbed by the surrounding healthy tissues [4]. The energy of the protons to cover different types of treatment need to be set between 60 and 250 MeV (depending on the tumor depth), which corresponds to a range between 3 and 38 cm in water (Table 1.1).

Table 1.1 Range and longitudinal straggling at different energies for protons and carbon ions

Protons			Carbon ions		
Energy (MeV)	Range (mm)	Straggling (mm)	Energy (MeV/u)	Range (mm)	Straggling (mm)
66	36.1	1.5	66	12.5	0.5
90	63	2.8	90	16.1	0.7
125	112.9	4.7	125	38.5	1.5
198	251.8	9.6	198	76	2.3
270	426.3	17.3	270	133.5	5
330	594.7	23.2	330	186.5	7

To achieve the treatment of the whole tumor, the energy of the beam has to be varied in a well-controlled way to obtain many narrow Bragg peaks that, when summed up, give origin to a Spread-Out Bragg Peak (SOBP) (Fig.1.3).

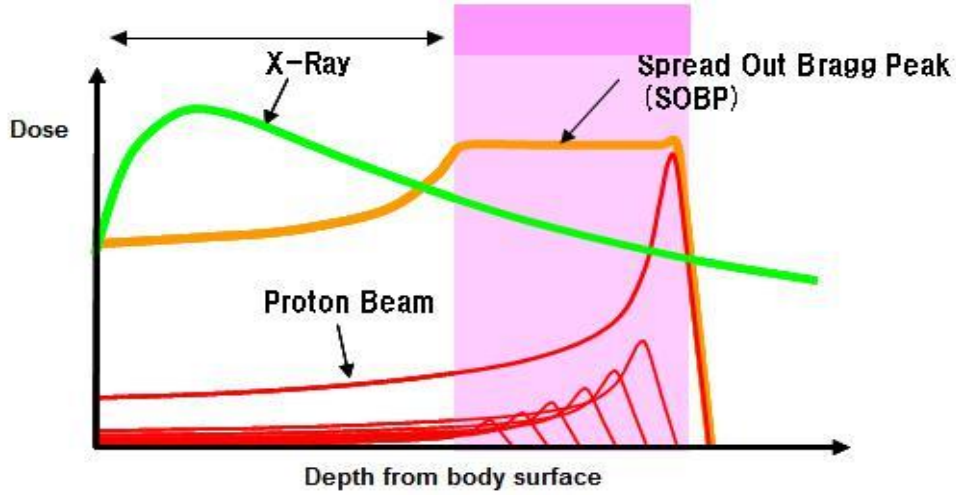

Figure 1.3 Typical Spread-Out Bragg Peak (SOBP) for protons. A SOBP is obtained as a superposition of many peaks by varying the proton energy.

A comparison of the typical planned dose distribution for the same tumor irradiated with X-ray or proton beams is shown in Figure 1.4. The plan shows how an X-ray beam deposits radiation dose to a much wider volume, with consequent risks of future toxicity.

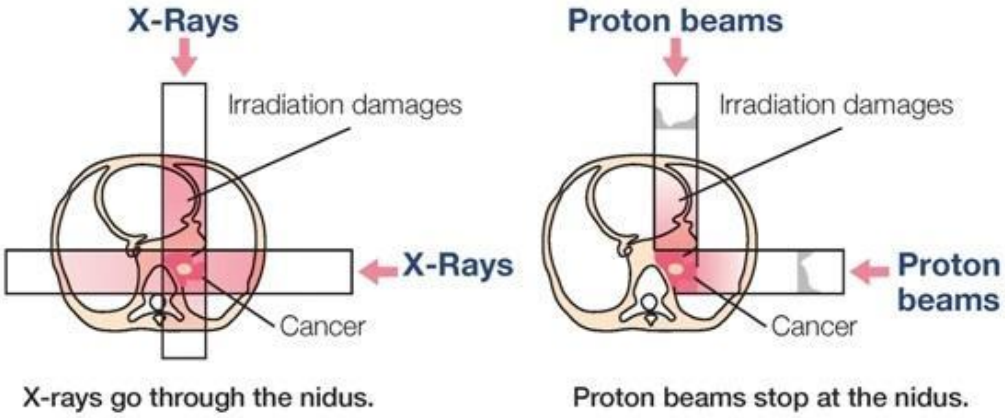

Figure 1.4 Comparison of the dose deposition of two X ray beams (right) with respect to two orthogonal proton beams (left)

To summarize, it should be remarked that radiotherapy with charged particles is considered a very advantageous tool to fight against cancer because of their physical (greater tumor conformation) and biological (greater biological effectiveness for heavy ions) properties [4].

In modern treatment facilities, proton and carbon ions are accelerated in synchrotrons or cyclotrons and focused in narrow beams of variable penetration depth, depending on their energy. The tumor volume can be accurately irradiated with optimal precision with minimal dose to the surrounding normal tissues if the beam energy and direction are properly modulated.

1.3. Accelerators employed in charged particle therapy

The technology of delivering a charged particle of the appropriate energy to a patient involves accelerating the particles and then focusing and bending the beam in the direction of the target.

Modern accelerator technology exists today to meet all of the clinical requirements within a reasonable budget for hospital-based hadron therapy facilities. Recent accelerator developments include fast extraction synchrotrons with fast varying energy, novel compact commercial solutions based on cyclotrons for proton therapy single room facilities.

1.3.1. Synchrotrons

The synchrotron consists of a lattice of bending dipole magnets and focusing quadruple and sextuple magnets (Fig. 1.5). The acceleration process in a synchrotron occurs in cycles, called “spills”, made by the following four steps (Fig. 1.6):

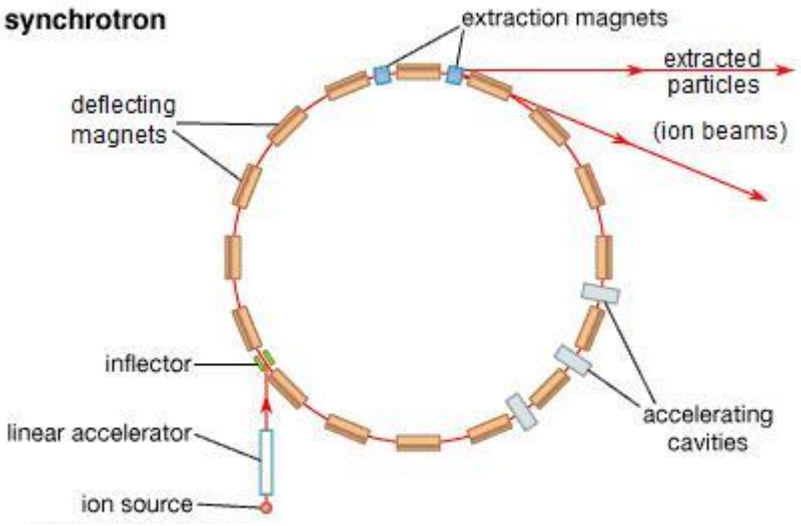

Figure 1.5 Scheme of a typical synchrotron which contains an injection line, deflecting magnets, accelerating cavities and an extraction line

1. a bunch of particles, produced by an ion source and pre-accelerated up to a few MeV using a linear accelerator (linac), is injected in the main ring of the synchrotron;
2. the beam circulates in the ring repeatedly through the accelerating structure until the desired energy, typically between 60 MeV and 250 MeV for protons, is reached;
3. a slow beam extraction for accurate dose applications is followed. The extraction time is typically between 0.5 and 5 seconds, depending on the required beam intensity (see Fig. 1.6. left). Schematically, the slow extracted beam would look like to the Figure 1.6. right;

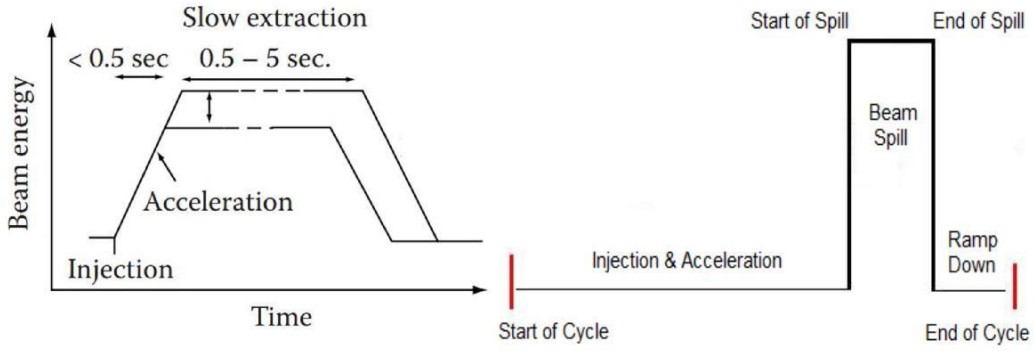

Figure 1.6 Scheme of the accelerator process in a synchrotron: Left: The injected particles are accelerated to the desired energy and slowly extracted; Right: Time structure of the beam delivery in one spill.

4. ramping down to the initial situation with deceleration and dumping the unused remaining particles.

A synchrotron produces pulsed beams at variable energies. The energy of the extracted beam can be varied from one cycle to the next in steps of a few MeV.

1.3.2. Cyclotrons

Cyclotron accelerators reach high projectile energies by repeated relatively weak accelerations of charged particles between two electrodes which relative potential is alternated at radio frequencies. Particles are injected, stripped of electrons, and accelerated by the field in the gap between the electrodes. During the periods in which the electric field is out of phase with the desired motion, the particles circulate inside hollow conducting D-

shaped electrodes. The particles are held to circular or spiral trajectories by a confining magnetic field until the selected final energy is achieved.

Commercially available cyclotrons for proton therapy typically deliver beams with an energy of 235–250 MeV [5]. Since the presently available cyclotron technology delivers the beam at fixed energy, the energy must be reduced to the value that is required for the treatment. This is typically done by an absorber consisting on a rotating degrader of different thicknesses and materials to reach a variable energy in the range between 70 and 250 MeV.

Figure 1.7 Cyclotron produced by the IBA company for proton therapy centers **[38]**.

The energy degradation produces significant emittance increase and energy straggling [6]. In order to fit to the acceptance of the beam transport system and to deliver a beam of the required quality most of the degraded beam has to be cut off by an energy selection system (ESS) consisting of a magnetic bending region followed by collimators [7].

Different beam intensities can be requested at the exit of the cyclotron, in a range spanning between 1 and 320 nA.

1.4. Treatment planning system

The Treatment Planning System (TPS) is a software which helps the physician to simulate the dose distribution in the patient and search for the optimal beam configuration to reach the clinical dose prescriptions. It is a complex tool, which receives as input the information on the patient anatomy as provided by the computed tomography (CT) data, the delineation of the target and of the surrounding organs, the beam set-up and the prescription of the wanted effect. Starting from these information and on the prescriptions on the desired dose on the target and the maximum tolerable dose on other organs, it performs a minimization procedure (called “inverse planning”) to

find the treatment parameters. The TPS task is completed when it finds the set of beamlets intensities, energies and directions necessary to satisfy at best the prescription.
The TPS seeks the solution in an iterative way: starting from an initial hypothesis on the beamlets intensities, the program computes for each point of interest the particles spectra and estimates the corresponding biological effect; if the result satisfies the prescription, then the TPS can terminate the execution and return to the physician the information on the prescribed beams; otherwise, the program must vary appropriately the beams intensities and repeat the biological effect evaluation, until the specifications are met or the maximum number of iterations is reached.

1.5. Beam Delivery Systems

The Beam Delivery System (BDS) is the last part of the machine before the tumor being irradiated, used to control the beam conditions and to assure that the dose distribution follows the prescription. The beam that comes from the accelerator laterally is well described by a 2D Gaussian function calculated as a function of the particle type, energy, depth and type of the material crossed from the vacuum exit window. The starting transversal and longitudinal dimensions have a typical FWHM (Full Width at Half Maximum) of less than 10 mm that is certainly smaller than the volume of a typical tumor, which normally could vary between 1 and 20 cm.

Basically, the narrow pristine beam extracted from the accelerator (known as pencil beam) with a fixed energy and direction cannot cover the irregular shape of the tumor volume without doing any adjustments.

There are many classes of techniques used to adapt the beam conditions and distribute the dose to the tumor volume in a correct way, following the prescription of the TPS.

The first class of dose distribution methods employs passive elements to spread out the original beam consisting of absorbers, collimators and range modulators, to create the proper SOBP and adapt the dose distribution to the lateral share of the tumors. The disadvantage of passive delivery techniques are the need of patient specific elements and the creation of secondary particles in the nuclear interactions of the beam with the passive elements.

Active beam shaping, or dynamic beam scanning [8], is a method to achieve the desired dose distribution by using magnets to move the beam laterally across the target while dynamically varying the energy of the beam to change the penetration depth.

The tumor is virtually divided into slices in the longitudinal direction, each slice being composed of small volumes called voxels or spots. Each slice is irradiated by a fixed energy beam which is moved in the transverse direction by a pair of scanning magnet [9] in order to deliver the required dose to each spot of the slice (Fig 1.8).

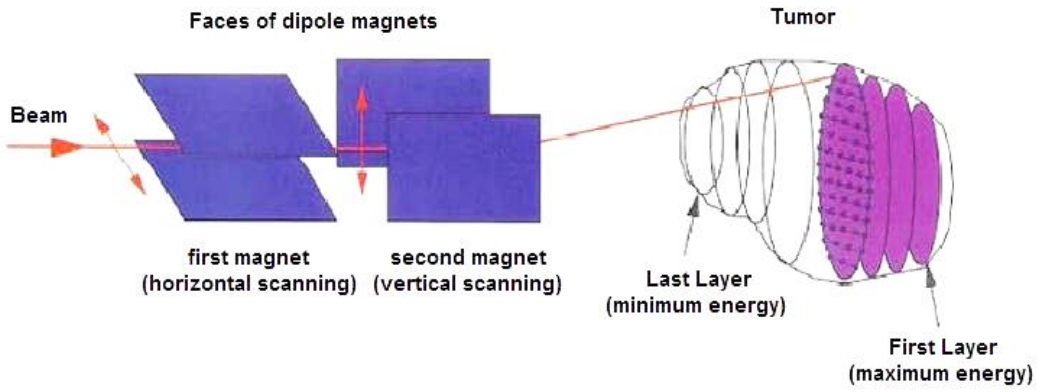

Figure 1.8 Scheme of an active dose delivery system. The tumor volume is divided in layers, and each isoenergetic layer is covered by a grid of spots. The beam is guided by a pair of scanning magnet irradiating each spot

The process of energy changes is achieved with various methods. In the case of a synchrotron, an energy variation can be obtained between two accelerator spills, while, for a cyclotron-based machine, an absorber for energy degradation followed by an energy selection system has to be used.

The advantages of the dynamic beam shaping can be achieved only by positioning the pencil beam and monitoring the number of particles delivered to each spot precisely using a fast and accurate monitor system fully integrated among the beam delivery system.

The drawback of such a beam delivery system is its greater complexity in operation due to the management of the scanning magnets and the control of the beam position. In addition, the tumor position must be known with high precision (of the order of 1 mm) to obtain the required precision in the dose shaping. Problems occur, specifically, when the tumor moves because of the patient's breathing and heart beats.

1.6. Dose Delivery System

The accuracy of the dose distribution achieved with the pencil beam scanning technique relies on a precise on-line measurement of the beam

position and the number of particles delivered to each spot. The Dose Delivery System (DDS) has to control the scanning system located at the end of the extraction line, consisting of two power supplies connected to two identical dipole magnets for horizontal and vertical beam deflections. Once the required number of particles is delivered to one spot, the DDS must change the magnet currents to move the beam to the next spot. In addition, the DDS has to be interfaced to the accelerator control to require a fast stop of the beam when one iso-energetic slide has been completed and to require a new energy values for the treatment of next slice.

The real-time control of the beam requires a monitoring system as most accurate and reliable as possible. The most commonly used beam monitor detectors are based on gas filled ionization chambers (IC). Figure 1.9, for instance, shows the monitoring system of CNAO [10], consisting of five parallel ionization chambers filled with nitrogen and placed at the end of the beam line, on the nozzle. Two chambers are devoted to measure the beam fluence with great accuracy and stability, at high speed, at 1 MHz rate.

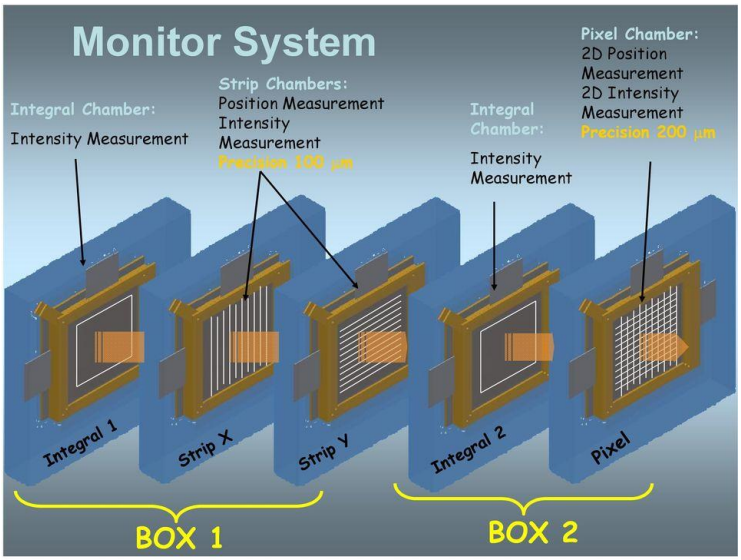

Figure 1.9 Components of gas based monitor system at CNAO

Other two ionization chambers with Kapton electrodes segmented in strips with orthogonal orientation are dedicated to measure the beam position with an accuracy of 100 µm every 100 µs through the evaluation of the center of gravity. A fifth chamber with the anode segmented in 1024 pixels provides an independent measurement of the beam position.

Thanks to their limited complexity, ICs offer several advantages such as robustness and ease of construction and operation, limited material budget (less than 1 mm water equivalent thickness) and show no indication of

performance degradation due to radiation and ageing effects, even after several years of irradiation.

However, they suffer from several limitations. Gas-filled detectors measure the charge produced in the gas, which depends not only by the number of particles, but also on the particle energy and on environmental parameters. To determine the number of particles delivered to each spot, the relevant clinical information on which the dose depends, the beam energy must be known in advance and the effect of temperature and pressure dependences must be corrected. Periodic calibration procedures are needed to take into account these effects and guarantee the reliability of the ICs in the clinical practice.

Another limitation of ionization chambers is their limited sensitivity: because of the small ionization charge produced in gases, the minimum number of particles an IC can detect is limited to the order of a few thousands. In addition, the charge collection times of ICs is relatively long (of the order of hundreds of microseconds), and therefore their response is quite slow.

These two limitations prevent their use in treatment modalities where fast position changes are required, or where a limited number of particles must be delivered to each spot.

Fast treatment modalities are required already now, for example, to treat moving organs with the so called “re-scanning technique”, where the dose painting is repeated several times with reduced doses, in order to mitigate interplay effects due to the combination of patient movements and beam position changes.

In the future, advanced irradiation techniques could be adopted, requiring more accurate, faster and more sensitive monitoring of the delivered dose. For example, 4-D treatments based on the tracking of the tumor position by following its changes with a movable beam are already a reality in conventional radiotherapy with dedicated linear accelerator such as Cyberknife and Vero [11]. The extension of such delivery modalities in charged particle therapy requires novel developments, on particular in faster scanning magnets, and on more precise monitoring detectors with improved speed, sensitivity and spatial resolution.

In general, fast beam delivery strategies represent the trend for future radiotherapy approaches, to improve the accuracy, to shorten the treatment times and to increase the patient throughput

The following section describes how the limitations of gas-filled detectors could be overcome by a new type of monitoring devices based on solid state sensors.

1.7. Beam monitoring with silicon detectors

To overcome the limitations of gas-filled detectors as monitoring devices in charged particle therapy, i.e. their limited sensitivity, the dependence of the measurable number of particles on the beam energy and environmental parameters, the poor position resolution and slow response times, a new approach for beam monitoring based on solid state detector is investigated in this thesis. In particular, segmented silicon detectors are considered as an alternative to IC chambers to count the number of particles of a therapeutic beam.

1.7.1. Silicon detectors

Silicon is a semiconductor, with a resistivity between that of metal and isolators, with the conduction energy band separated by 1.14 eV from the valence band. An electron jumping in the conduction band leaves a hole in the valence band, which behaves like a positive charge carrier. When the silicon is doped with Type III atoms (acceptors) "p-type" material can be formed with an excess of holes. A doping with Type IV atoms (donors) produces "n-type" materials with an excess of conducting electrons.

A silicon detector is based on p-n junctions, where a large depletion region free of conductive charges is formed by applying an intense inverse polarization. In a silicon detector the depletion region is the active volume where hole-electron pairs are created by the ionization of the crossing particles, similarly on how ion-electrons pairs are produced in a gas detector. The current induced in the electrode during the migration of the hole-electron pairs is collected and integrated to measure the total produced charge, proportional to the energy loss by the charged particle.

Even if the working principle is similar, the mean energy needed to create a hole-electron pair is an order of magnitude lower in silicon than in a gas (3.6 eV in Si vs more than 30 eV in N_2 or in air). Considering also the much higher density of silicon with respect to a gas, the charge produced by an ionization particle in a thin silicon layer is high enough to be measurable for a single particle.

Silicon detectors are built with a multitude of p-n junctions with the electrodes segmented in strips or pixels, and employed for particle tracking in charged particle and nuclear physics applications [12].

An example of a silicon microstrip detector is depicted in Fig. 1.10, it consists of highly dipped p-type (p+) strips implanted on a n-type planar

substrate, and a n++ backplane electrode. The n substrate is fully depleted by applying a positive voltage on the n++ electrode with respect to the strips. An ionizing particle penetrating through the fully depleted slice generates electron-hole pairs which migrates along the electric field generated by the bias voltage and induce a charge signal on the aluminum strips. In this example the aluminum electrodes are separated by a thin SiO2 capacitive layer (AC-coupling), but strip structures with direct aluminum-p+ contact are also used (DC-coupling).

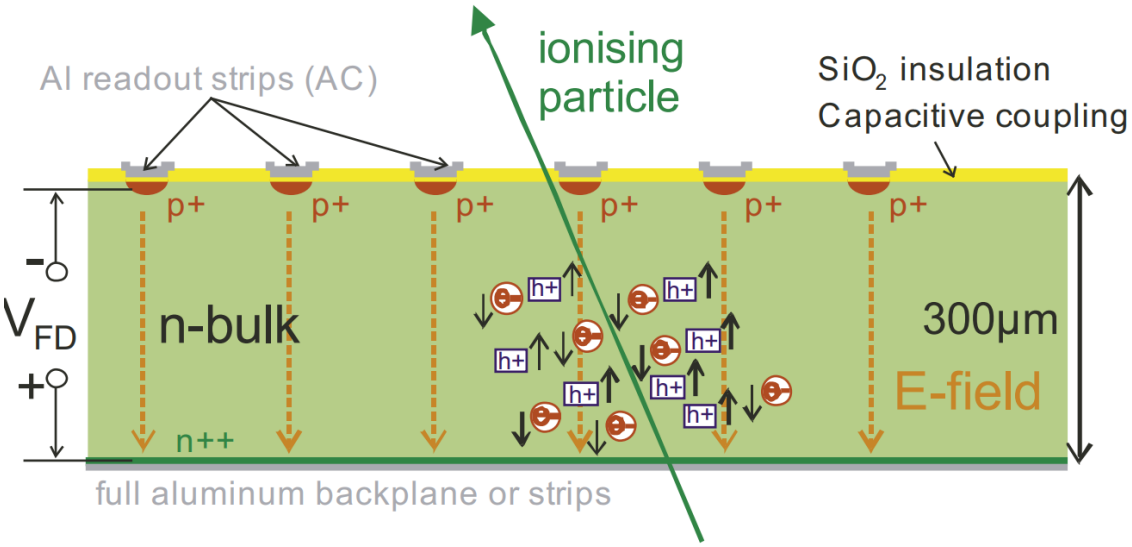

Figure 1.10 Charge formation by ionizing particle passing a multi strip silicon detector

In a typical strip detector, the thickness of the depletion region is about 300 µm to produce enough charge to be detectable by the readout electronics, which consists of a charge-sensitive amplifier collecting the signals from each strip. The typical collection time of electrons and holes is of about 6 to 10 ns, depending on the applied bias voltage. This time is short enough to allow to detect single particles even at high fluxes, if the detector is properly segmented.

The idea of this thesis work is to explore the capability of silicon strip detectors to discriminate the single protons of a therapeutic beam and to directly count their number, instead of evaluate this number by the total charge produced in the detector, as it is done with ionization chambers.

1.7.2. Advantages of particle counting in charged particle therapy.

The direct count of the number of protons of a therapeutic beams with a silicon detector would offer several advantages if applied for monitoring purposes. If the signal from the sensor is short and the pixel or strip

segmentation is high enough to allow to separate single particles, a direct measurement of the number of protons would not depend on the knowledge of the beam energy or on environmental parameters, as it happens with ionization chambers. In addition, a silicon sensor is potentially sensitive to each single particle, overcoming the sensitivity limitations of the gas detectors nowadays used for beam monitoring. Moreover, the response time of silicon detectors depends only on the charge collection time, allowing to follow beam changes occurring in a few ns, with respect to hundreds of µs integration times of ICs.

A monitoring device based on silicon detectors working in particle counting mode is therefore a potential candidate to overcome the limitations of ionization chambers in terms of speed, sensitivity and accuracy. In addition, very high space resolutions can be achieved with segmented silicon sensors, allowing to measure the position of each particle with a resolution of the order of 10 µm, with respect to the typical resolution of 100 µm achieved by ICs integrating the charge produced by several thousands of protons.

In order to operate a silicon detector to monitor therapeutic beams, the clinical requirement on a maximum error of 1% on the number of protons must be respected. This is challenging for a detector working in counting mode, because the overlap of signals from two particles crossing the same detector channel close in time gives rise to saturation effects at high particle rate.

The only two possible solutions to operate a silicon counting device at high particle rate are to segment the detector in a large number of independent readout channels with small area and/or to reduce the signal duration.

The first solution would require a detector segmented in small pixels. The complexity of a pixel sensor and of the readout electronics would be high, but possible with the current technology.
The second solution requires a thin detector, with a depleted region few tens of µm thick, with respect to the 300 µm thickness used in traditional silicon detectors. A reduced thickness would be useful also to reduce the beam distortion due to multiple scattering in the silicon material, that must be limited as much as possible in a beam monitoring device.

The technological choices for a prototype of particle counting device, described in details the following chapter, have suggested the use of silicon strip detectors for the sensor segmentation, as an intermediate step with a reduced cost and complexity with respect to a pixel detector.

The sensor thickness of the device prototype will be limited to 50 µm. However, the consequences of a small thickness for a silicon detector are a reduction in the charge produced in the sensor and an increase in the detector capacitance, resulting in a limited signal-to-noise ratio. The electronics would not be able to separate particle signals from fake counts due to noise with the high purity greater than 99 % required for this application.

The solution is to adopt a novel silicon sensor technology, called Low-Gain Avalanche Diode (LGAD), which provides enhanced signal-to-noise ratio even in detectors with low thickness.

1.8. Ultra Fast Silicon Detectors

Charge multiplication is well understood in gases and solids and is based on the avalanche process initiated by a charge moving in large electrical fields, leading to impact ionization with a gain given by the average number of final particles created by one particle. In semiconductors this effect is used to detect photons in Avalanche Photon Detectors (APD) [13] with gain of the order of 100's and Silicon Photon Multipliers (SiPM) [14] with a gain of about 10000. This high value of gain allows to achieve very good signal to noise ratios and time resolution but it has some drawbacks, namely the increase in sensor noise, the difficulties in sensor segmentation and large recovery times.

Detection of charged particles instead of photons has the advantage of a much larger initial signal, since on average in one micron 73 electron-hole pairs are created by a minimum ionizing particle (MIP), allowing the use of lower gain values which is in the order 10-20. A moderate internal gain mechanism has been introduced in silicon detectors with the Low-Gain Avalanche Diode (LGAD) design [15], where the high electric field needed

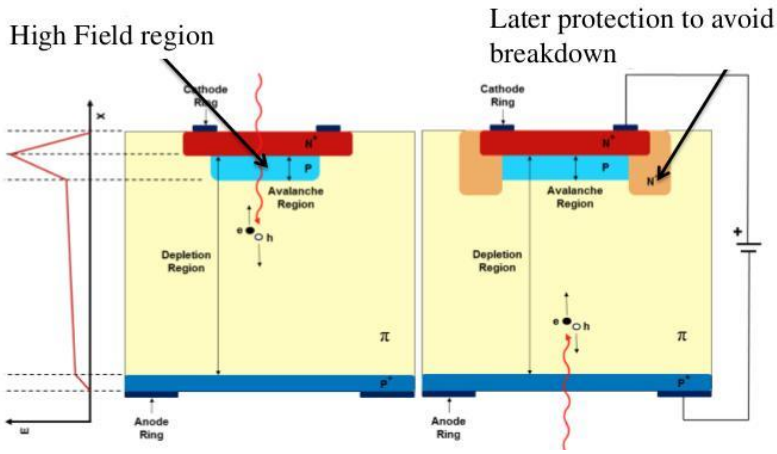

Figure 1.11 Scheme of LGAD n-on-p detector with implanted p+ gain layer below the n++ electrode

for the multiplication mechanism is obtained by implanting a p+ layer below the n++ electrode of a planar n-on-p silicon sensor (Fig. 1.10).

When reverse biasing the sensor, a high and localized electric field is established in the n++/p+ junction. Free electrons migrating toward the n+ electrode are accelerated under the effect of the high electric field; this produces further ionization and a multiplication of the number of electron-hole pairs.

The intensity of the local electric field and the amount of charge gain can be adjusted by altering depth and doping concentration of the additional p+ layer, in order to obtain a uniform multiplication mechanism across the electrode. The choice of an appropriate electric field is a crucial point in the development of LGAD sensors: the field must be high enough to obtain charge multiplication and sufficiently low to prevent breakdown.

Below the breakdown voltage, the gain factor (defined as the ration of the charge produced in the LGAD detectors over the charge produced in a similar diode without gain layer) can be changed with the applied bias voltage.

Their main advantage of LGADs is to provide an enhanced signal in thin detectors (few tens of micrometers) with similar noise level of a traditional silicon sensor of the same geometry, leading to fast detectable signals of very short time duration (1-2 nanoseconds in 50 micrometers thickness). These characteristics meet the requirements for a beam particle counter illustrated in the previous section.

In Torino LGAD detectors have been optimized to enhance concurrently the space and time resolutions with respect to traditional silicon sensors. LGAD detectors designed to enhance the time resolution are called Ultra Fast Silicon Detectors (UFSD) [16]. An outstanding time resolution of 16 ps has been measured with thin UFSD detectors [17].

Ultra Fast Silicon Detectors (UFSD) are the choice for the particle counting device studied in this thesis. In the following LGAD and UFSD terms will be both used, as synonymous of silicon detectors with moderate internal gain.

Chapter 2

Design of a single particle counter device

2.1. Introduction

As mentioned in the previous chapter, the goal of this work is to investigate the use of silicon detectors to monitor the number of protons delivered with a therapeutic proton beam with high accuracy (less than 1 % error), in a wide range of beam energies (typically between 60 and 250 MeV) and at high fluxes (the therapeutic flux ranges from 10^8 to 10^{10} p/(cm^2·s)). In contrast to the commonly used monitoring modalities, employing the charge produced for ionization in a gas detector, a silicon detector could be operated in counting mode to detect single beam particles and count their number. The sensor must be coupled to front-end electronics containing an amplification stage and a discriminator to compare the signals to a fixed threshold and provide short output pulses to be counted.

The counting capabilities of such a device depends on the minimization of pile-up effects due to the overlap of signals close in time. For the sensor, the maximum measurable flux depends on two factors:

1) the signal duration, related to the collection time of the electron-hole charges produced in the sensor, which defines the intrinsic dead time of the detector. The collection time is proportional to the thickness of the sensor active volume, and therefore small signal durations require thin detectors.
2) Signal segmentation. The typical transverse dimensions of a therapeutic beam range between few mm and about 1 cm, depending on the beam energy and accelerator optics. The particles flux can therefore be shared between several channels of a fine segmented detector, with each channel proving signals from a fraction of the beam particles. A silicon sensor with electrodes segmented in strips or pixels allows to extend the maximum measurable flux, depending on the area of each channel. To avoid double counting effects, the probability of hit coincidences in two neighboring channels due to charge sharing must be limited to less than 1 % for the required accuracy on the number of counts. The dead area between detector channels must be considered to deduce the total number of delivered particles from the measured number of signals provided by each sensor channel.

The requirements on a counting accuracy greater than 99 % up to high fluxes dictates additional constrains to the front-end electronics, in particular:

1) The front-end electronics must be as fast as possible to limit additional dead times and signal tails. A fast baseline restoring is also necessary to avoid a shift of the signals levels at high particle rates which would give inefficiency effects when the signals are compared to a fix detection threshold.
2) A detection efficiency greater than 99% is required for a wide range of signals, depending on the particle energy and random fluctuations in the number of electron-hole pairs produced in the sensor.
3) The noise level must be small enough to keep the probability of fake counts due to noise spikes below 1 %.

The electronics and sensor designs are not independent. In particular the sensor capacitance plays a central role in terms of electronic noise and amplifier time constants. In general, a high capacitance corresponds to an enhanced electronic noise. The capacitance of silicon sensors increases with an inverse proportionality with respect to the depth of the depleted region.

On the other hand, in a silicon sensor, fast charge collection is obtained with thin sensitive volumes. Therefore, thin detectors are needed in order to maximize the counting rate. A compromise has to be found for the detector thickness, which must be thin enough to provide short signals and at the same time with an acceptable capacitance.

Strip or pixel detectors commonly used for tracking in nuclear physics experiments have a typical thickness of 300 μm, corresponding to a signal duration of almost 10 ns, preventing the separation of two particles separated by several ns in time. Building detectors with lower thickness would allow a better separation and the reduction of pile-up effect due to signal overlap, but at the same time it will give an increase in capacitance and a reduced signal due to the smaller number of electron-hole pairs produced in the sensor by an ionizing charged particle.

The development of silicon sensor technology of the past year has produced innovative detectors with enhanced signal-to-noise ratio with respect to traditional silicon diodes. These new detectors (UFSD or LGAD), described in the previous chapter, allows to compensate the loss of signal in small thickness and have been adopted in this work as a possible candidate for beam monitoring applications, providing short signals with acceptable currents to the readout electronics. In this chapter, the design decision and technical details of the dedicated silicon structures and front-end electronics are described.

2.2. Design of UFSD strip detectors for particle counting

For R&D purposes, different UFSD structures have been produced at Fondazione Bruno Kessler (FBK, Trento) in the previous years, starting with simple pads and small sensors with a limited number of pixels or strips. All these structures have been designed in collaboration with INFN of Torino, on the base of TCAD simulation, and carefully tested in laboratory and in test beams from the Torino group, in order to assess their timing performance [18].
In addition, different front-end alternatives have been used for the readout of these sensors, based on simple passive boards for the sensor mounting and HV distribution coupled to external amplifiers, to dedicated ASIC chips optimized for timing measurements [19].

The medical physics group of Torino University and INFN Torino participated to these studies from the beginning, since 2014, to understand the performance of UFSD detectors and investigate possible medical applications, in particular for beam monitoring in charged particle therapy. In 2016 the research group joined a collaboration of several INFN institutes to prepare a project on advanced radiobiological studies and measurements, which won a grant of INFN Commissione Scientifica Nazionale 5 (CSN5). In these collaborations, the Torino group proposed the development and construction of two beam monitoring prototypes, to be used in radiotherapy experiments, as described in the following section.

2.3. The MoVe-IT project

MoVe-IT [20] is an INFN project started in 2016 which aims at developing innovative treatment planning systems, integrating new biological models to consider the impact of different effects, such as target fragmentation, Relative Biological Effectiveness and intra-tumor heterogeneity. To validate these new models, dedicated devices for beam characterization and monitoring in radiobiological and clinical irradiations are requested.
When the MoVe-IT project was prepared, it was clear that the UFSD technology was a good choice to build a first prototype of particle counting device based on solid state detectors.
The possibility to use silicon detectors based on the LGAD technology for beam monitoring was present since the beginning in the medical physics group of Torino. Several tests with simple pads were already performed on therapeutic proton beams before the start of the MoVe-IT project, to study the behavior of these detectors in the harsh environment of a clinical treatment facility.

The optimal design choice for a counting detector working at the high particle fluxes of a proton therapeutic beam (10^9 to 10^{10} p/cm^2) would require thin sensors with a very fine segmentation in small pixels. Simulations were performed before 2016 to understand the possible designs and problems related to charge sharing effects between different pixels, the requirements for radiation resistance and many other parameters.
A design based on pixel detectors is very complex and costly: the number of channels would be very high, a dedicated multi-channel chip to be bump bonded to the sensor would be necessary, and the cost would be not acceptable for a prototype device. For this reason, a first counting prototype was proposed within the MoVe-IT project, based on sensors segmented in strips instead of pixels, due to the need of detectors and electronics simple to develop in a relatively short time, with a reasonable complexity and price. A strip detector is limited in the maximum flux that can be monitored with accuracy, but it is useful in radiobiological experiments, for which it is not needed to reach therapeutic fluxes and often laterally spread-out beams are used. In addition, the limited area of a biological culture to be irradiated is compatible with sensors of small area.

The design of the counting device was based on the requirement of the radiobiology partners:

- Cover an area of 3x3 cm^2
- maximum measurable flux of 10^8 p/cm^2·s with less than 1-2% error
- sensitivity to single particles at very low fluxes
- provide the beam shape in two orthogonal directions

On the base of these requirements, and on the expertise gained by the UFSD collaboration, a strip area of 2 mm^2 and a sensor thickness of about 50 µm was proposed. More details follow in the next section.

2.4. Design of the strip sensor prototype

When the MoVe-IT project started, two dedicated LGAD structures were designed in Torino with the TCAD Synopsys Sentaurus software tool [21]. In both the designs the active volume has a thickness of 50 µm to keep the signal duration below 2 ns, and the sensors are segmented in strips, to provide a fine enough segmentation and limit the pile-up effects at the design particle rate. The area of the p+ layer below each strip is 2 mm^2, and the expected capacitance of each channel is about 7 pF, a value that in previous structures has shown to provide a reasonable noise level when it is coupled with the readout electronics. The two structures are shown in Figure 2.1.

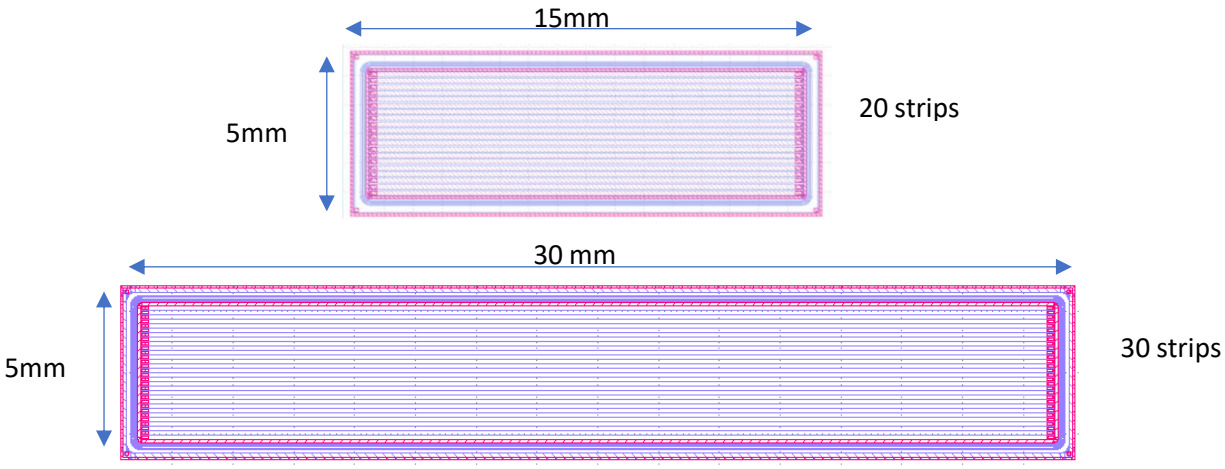

Figure 2.1 MoVe-IT strip structures

A set of sensors (named “MoVe-IT short strips”) contains 20 strips with a pitch of 216 µm, with each strip 15 mm long. The second set of structures (named “MoVe-IT long strips”) contain 30 strips, 30 mm long, with a pitch of 146 µm (Fig 2.1).
In both the sensor designs the lateral side with the contacts at the strip edge have the same length of 5 mm.

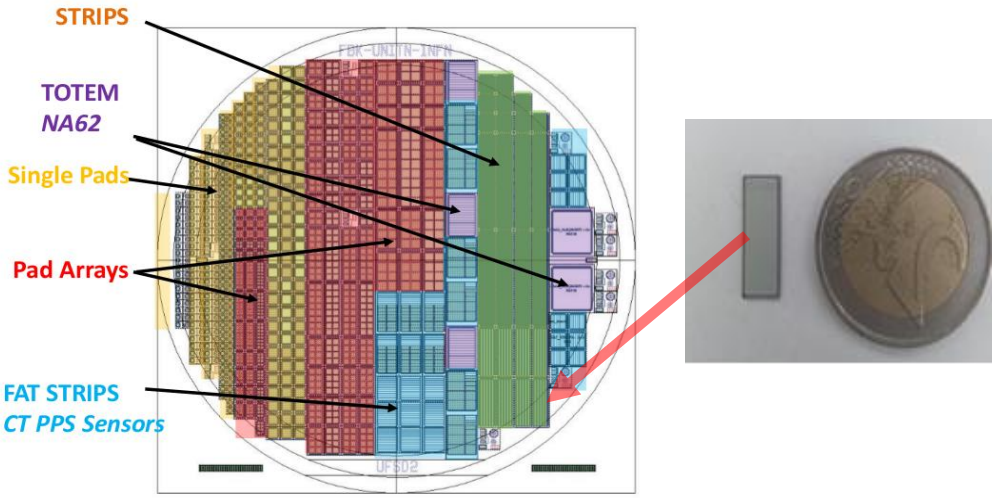

Figure 2.2 Wafer layout (left), small strip UFSD (right)

These structures were included in multi-project wafers depicted in Fig. 2.2 and produced at Fondazione Bruno Kessler (FBK, Trento) in 2017 A total number of 18 wafers were produced with different doping modalities for the gain layer to study the optimal strategy in terms of radiation resistance. The implantation of the p+ gain layer was performed using Boron or Gallium with different doses, different thermal cycle resulting in low or high

diffusion of the implanted acceptors, and in some wafers the implantation of a dose of carbon was added. The list of different doping alternatives used in each wafer is shown in Table 2.1.

Wafer n.	Dopant	Dose PGAIN	Carbon	Diffusione
1	Boron	2.45		L
2	Boron	2.5		L
3	Boron	2.5		H
4	Boron	2.5	1e18	H
5	Boron	2.5	1e19	H
6	Boron	2.55	1e18	H
7	Boron	2.55	1e19	H
8	Boron	2.55		H
9	Boron	2.55		H
10	Boron	2.6		H
11	Gallium	2.5		L
12	Gallium	2.5		L
13	Gallium	2.60		L
14	Gallium	2.60		L
15	Gallium	2.60	1e18	L
16	Gallium	2.60	1e19	L
17	Gallium	2.7		L
18	Gallium	2.7		L

Table 2.1 Table summarizing the doping parameters adopted for each wafer in the FBK production of UFSD sensors

The expected gain value of the MoVe-IT strips is about 10. Some strip structures in the wafer were produced without gain layer to study the gain factor corresponding to different structures and doping modalities, as described in the following chapter.

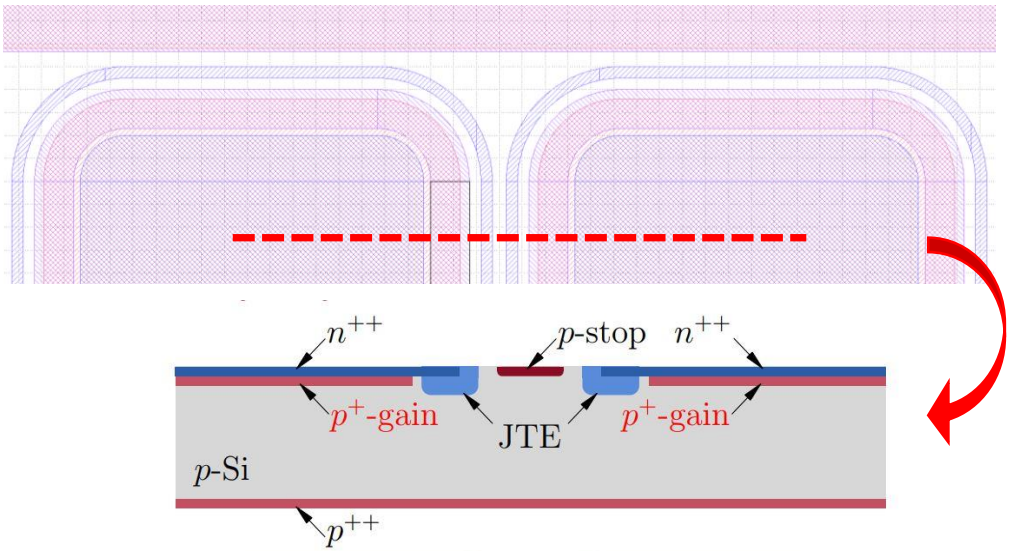

Figure 2.3 Two UFSD structure with cross section

It is worth underlining here some features of these sensors which will be recalled later (Fig 2.3). UFSD are provided with guard rings: n-implants that enclose the active area and have the same polarity of the n-electrode. Guard rings protect the n-electrode collecting charges produced in the periphery of the sensors, reducing the current flowing in the electrode and avoiding the collection of charges which, since they come from the outer part of the sensor, would increase the noise. Another important structure is the n-deep or JTE (Junction-Termination-Extension): this structure is basically a region of n-Silicon placed at the extremities of the gain layer volume; such structure is used to contain the field lines in the active volume, avoiding to collect charges outside it [22]. This tends to create an inter-strip zone where the charges are not multiplied due the absence of the gain layer. The "no gain zone" between two gain layers has a nominal width of 66 µm for the short and long strips structures produced for MoVe-IT.

The UFSD strip sensors were tested in laboratory and with proton beams between 2017 and 2019. In parallel to the characterization and test works, described in the next chapter, a batch of LGAD pads have been irradiated with protons and neutrons up to high values of fluences to determine the doping version with better radiation resistance.

The MoVe-IT strip structures dedicated to particle counting of charge therapy beams must be coupled to a custom readout electronics, designed, produced and tested at INFN Torino in parallel with the strip structures. The role of the electronics is to amplify the current signals from each strip and compare the amplified signal with a fixed threshold to provide a logical pulse for each particle (Fig.2.4).

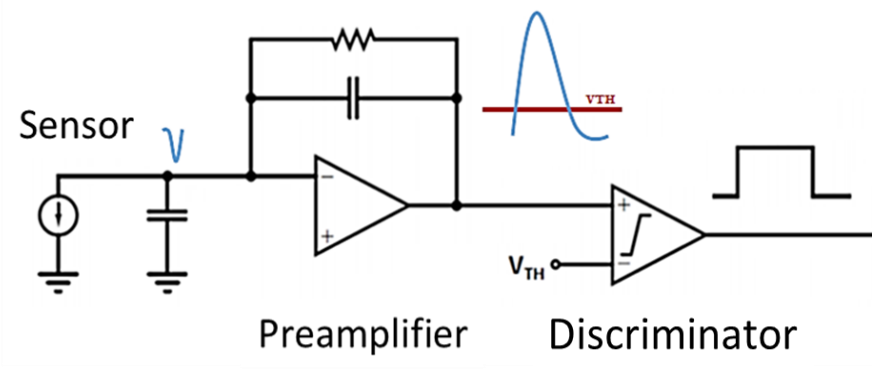

Figure 2.4 Schematic of the readout electronics of one UFSD strip

The design of the readout electronics required an accurate simulation of the output current from the strips for all the possible proton energies of a therapeutic beams, considering the Landau fluctuations of the charge

produced in the sensor. These simulations were performed within the thesis work with a dedicated simulation software described in the following section.

2.5. UFSD Simulator: Weightfield2.0

Weightfield2.0 [23] [24] is 2D simulation software of UFSD silicon detectors developed in Torino. It is based on an existing program called Weightfield developed by HEPHY in Vienna which simulates the current signal in a silicon detector with micro strip or pad geometry. The original program has been complemented with the addition of new simulation options and adapted to simulate the effect of the gain layer.

The Weightfield2 program is implemented in C++ language and makes use of the ROOT Graphical Interface. The graphical interface allows the user to select simulation parameters such as the type of incident particle, sensor geometry and doping, depletion and bias voltages and to display drift and weighting potentials (Figure 2.5), as well as current signals and oscilloscope output.

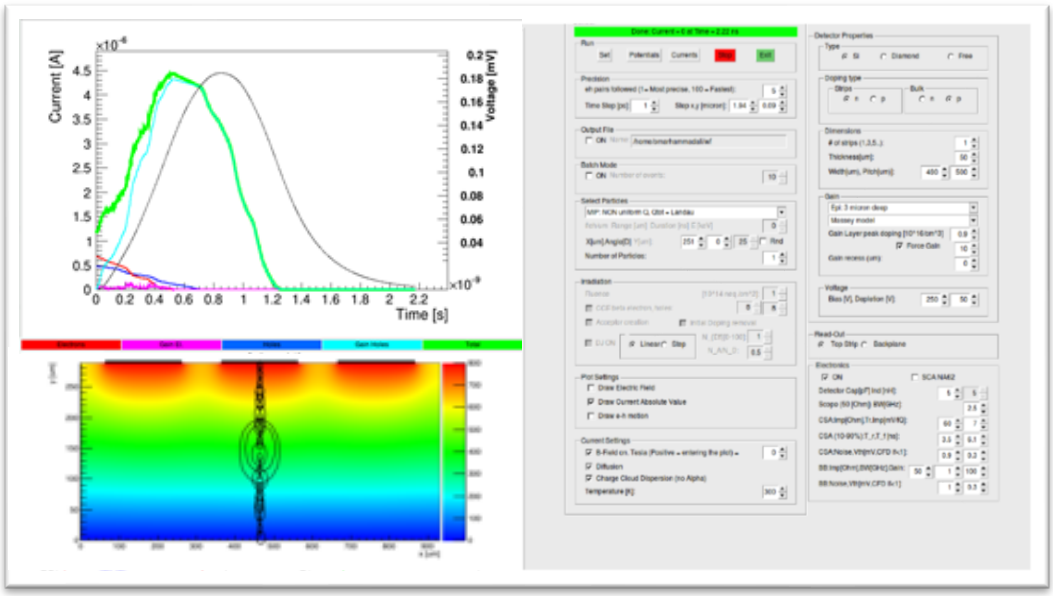

Figure 2.5 Snapshot from the Weightfield2 graphical user interface

The signal of a silicon sensor is defined as the current induced on the electrodes; so, even if we talk about charge collection, signal does not start when the charge is collected, but just when the charge begins to move inside the sensor. The induced current on a single electrode *i* is then given by Ramo's theorem:

$$I_i = -q\vec{v}(x) \cdot \overrightarrow{E_\omega}(x) \qquad 2.1$$

where v(x) is the charge velocity and depends on the applied electric field E and on the charge position x. E_ω is called weighting field and is defined as the virtual electric field which is determined by applying to the collecting electrode i the potential 1 and 0 to the others. The weighting field is only geometry dependent and it is independent of the bias voltage.

The program simulates the electron-hole pairs produced by an ionizing particle by distributing charge carriers along the trajectory, taking into account statistical fluctuations in the charge production. The local charge production is implemented on the base of the results of Geant4 [25] simulations. The point where the particle hits the detector and the angle formed with the vertical are selectable from the graphical interface.

For instance, minimum ionizing particles (MIPs) with non-uniform charge distribution following a Landau distribution is the option used to simulate the signals produced by particles from treatment facilities and later is used as a reference to build and design the ASIC, assuming a range in the produced charge corresponding to 1 up to 6 MIPS depending on the energy.

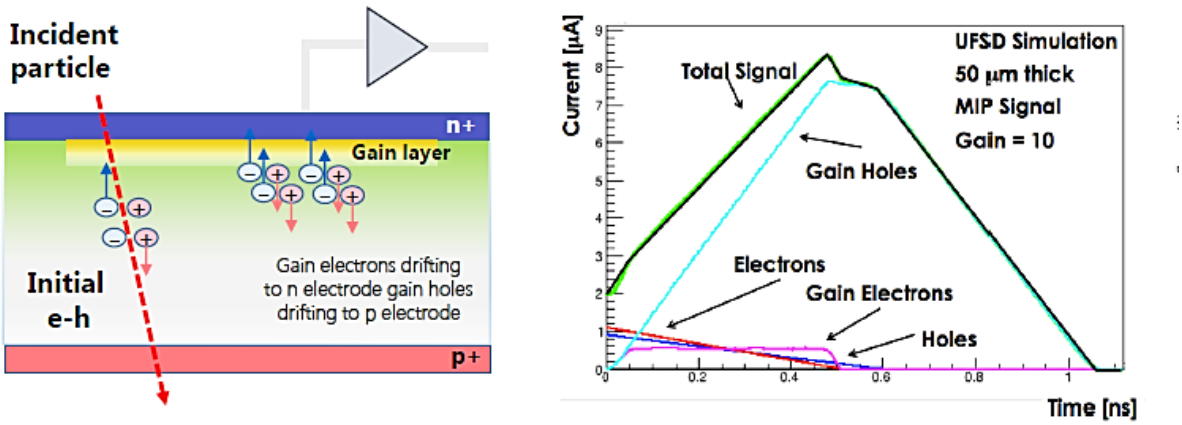

Figure 2.6 Left: charge migration inside a UFSD detector; Right: contribution of different carriers to the UFSD output current

The left part of Figure 2.6 shows an example of charge production mechanism, while the right part shows the current output provided by Weightfield2 for a UFSD diode of 50 μm thickness and gain 10. When the ionizing particle crosses the depletion region, primary electron-holes pairs are produced and migrate toward the electrodes. The contribution to the current signal from the primary holes (blue curve in Fig.2.6 right) decreases while they are collected in the p+ electrode. When the primary electrons

reach the high field region of the p+ gain layer charge multiplication occurs and additional electron-holes pairs are created. Both the primary and secondary electrons are collecting by the n+ electrode giving a small contribution to the output current (red and pink curves). The contribution of the secondary holes to the current signal (light blue curve) increases until all the electrons reach the gain region, and after decreases while the holes migrates toward the p+ electrodes and are collected. The overall signal duration is little more than 1 ns.

The Weightfield2.0 software was used to collect the time dependence of the current signals produced by minimum ionizing particles (MIPs). This information are stored on files and used to simulate the current flow from beam particles in a treatment facility with a proper time distribution used as a reference to build and design the electronics, assuming that the charged particles hitting the sensor corresponds to a range of 1 up to 6 MIPS depending on the energy.

2.6. Design of the front-end readout ASIC

A dedicated multi-channel front-end Application Specific Integrated Circuit (ASIC) was designed, produced and tested at INFN of Torino for the readout of the MoVe-IT strips.
The first information needed to design the amplification stage was the input capacitance of the sensor and the expected range of the integral charge produced by each particle, in order to adapt the dynamic range of the ASIC chip to all the conditions expected when the sensor is irradiated with therapeutic protons.

The capacitance depends only on the geometry adopted for both the short and long strips corresponding to a value of 7 pF.

As already discussed, the design goal of the counting device produced for the MoVe-IT project is to measure the number of protons with a maximum error of 1% up to a fluence rate of 10^8 p/(cm^2·s). The value of the maximum fluence rate due to signal pile-up was already discussed in the previous part of the thesis, and is limited by the sensor thickness and strip area, assuming the system is fully efficient for all the particles. For a single particle the efficiency must be greater than 99 %, and this define the range of charges the electronics must be able to accept. The typical proton beam energy adopted in particle therapy ranges between 60 MeV/u and 250 MeV/u corresponding to an ionization from 2 to 6 times that of a MIP particle; therefore, the expected charge range at the front-end input is very wide.

Geant4 simulations were used to include the effect of the Landau statistical fluctuation in defining the charge distribution for MIPs and protons of different energies in 50 µm of silicon thickness. The results are shown in Fig.2.7 where the charge distributions expected for therapeutic carbon ions (kinetic energy between 120 MeV/u and 400 MeV/u) is also included.

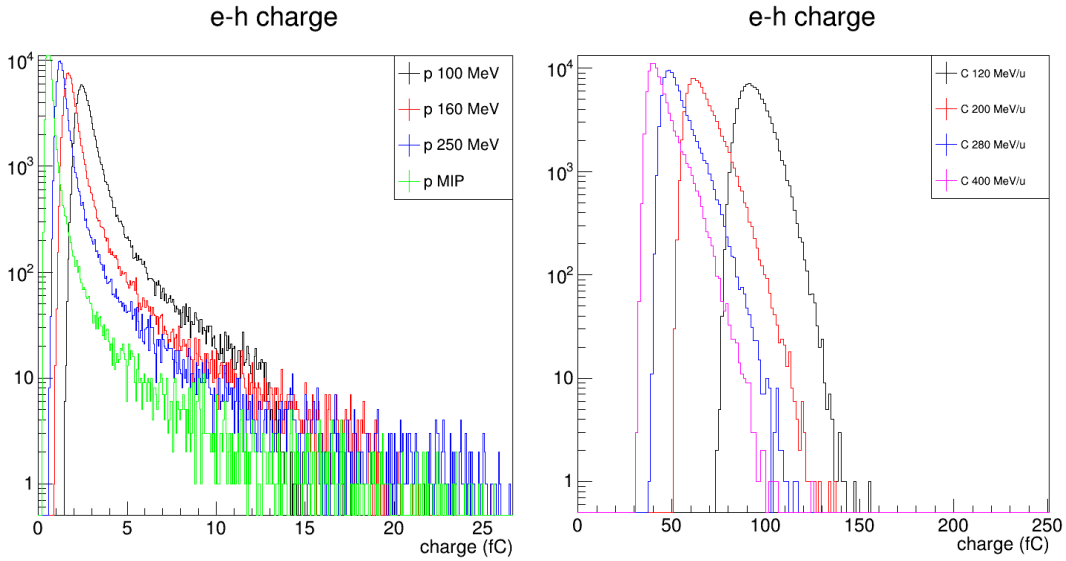

Figure 2.7 Left: Distribution of charge produced by MIPs and protons of different energies in 50 µm thick silicon layer (simulations from Geant4, no gain included). Right: charge distribution produced by carbon ions of different energies in 50 µm of silicon.

From these distributions the range of charges expected for MIPS, protons and carbon ions of different energies can be determined. The high limit of the charge range is determined such that less than 1 % of the protons release a higher charge in the silicon. The effect of the UFSD gain is considered as a multiplicative factor to the results of the Geant4 simulation. The results are shown in Table 2.2.

Particle	Gain	Min charge [fC]	Max charge [fC]
MIP	1	0,2	8
Protons 250 MeV	1	0,5	10
Protons 60 MeV	1	2	15
Protons 250 MeV	10	5	100
Protons 60 MeV	10	20	150
Carbons 120-400 MeV/u	1	30	150

Table 2.2 Simulated charge release by different particles in a UFSD sensor without gain and with gain =10

According to the results shown in the previous table, the range of charges produced by therapeutic protons in a 50 µm thick UFSD silicon detector with gain 10 is between 5 fC and 150 fC. The indication to electronic designers was to optimize the chip to operate on a charge range between 3 fC and 150 fC, where a large tolerance was added to the lower limit to consider the possibility to use sensors with lower gain. An electronics able to operate with this charge range can also be used to readout signals produced by carbon ions in a sensor without gain layer, a possibility that we want to keep open for the future.
We also asked to design the electronics in order to have a signal-to-noise ratio greater than 10 at the minimum detectable charge, in order to minimize the fake counts due to the electronic noise.

The front-end electronics was integrated in a 24-channels chip nicknamed ABACUS, Asynchronous-logic-Based Analog Counter for Ultra fast Silicon strips [26]. The ABACUS ASIC has been designed with minimum MOSFET gate length of 110 nm and produced within a Europractice multi-project wafer. The design area is 2x5 mm^2 and the number of pads is 140.

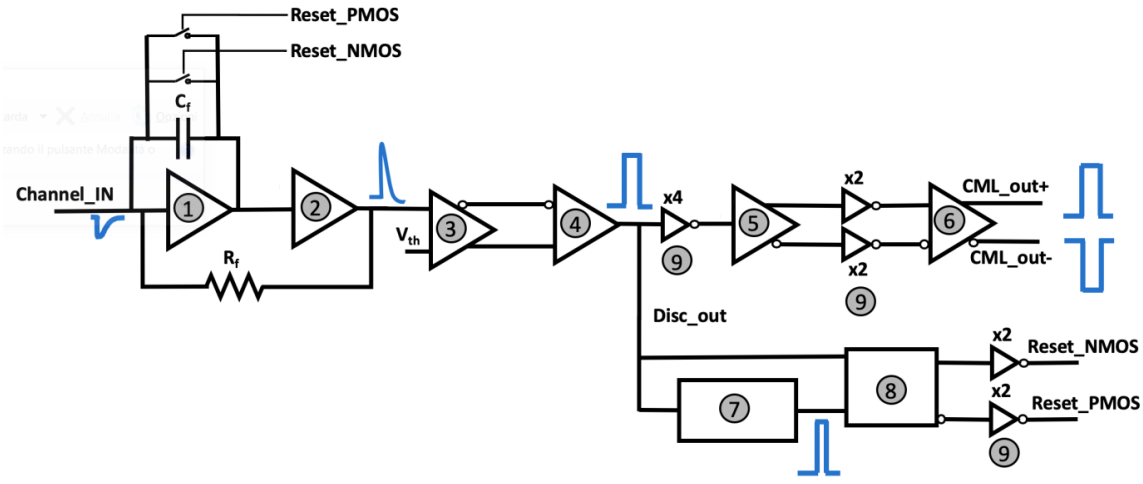

Figure 2.8 Block diagram of one ABACUS channel.

The block diagram of one ABACUS channel is shown in Fig 2.8. A charge sensitive amplifier (CSA) (1) is followed by a low-pass filter (2). The amplified signal is therefore fed to a leading-edge multistage discriminator (3 and 4) followed by a driver (5 and 6) which provides a logic pulse in Current mode logic (CML) format. The output of the discriminator is also used in a feedback circuit (7 and 8) to reset the CSA feedback capacitance. This feedback circuit was designed for a fast baseline restoring and to avoid signal saturation. The ABACUS chip was optimized for an input capacitance between 5 and 20 pF and to cope with continuous signals up to 100 MHz rate.

During the design stage a simulation of the time distribution of the current signals expected in a realistic case was needed to simulate the circuit behavior at high particle rate. I worked to produce files with signals randomly distributed in time at different rates, using Weightfield2 simulations to generate the time evolution of each signal.

These files were used as input to CAD post-layout simulations of the circuit used to optimize its performance at high particle rates. An example of results from these simulations is shown in Figure 2.9, with the input current is on the top, followed by the output from the CSA (green), from the low-pass buffer (green) and by the CML+ and CML- outputs (bottom).

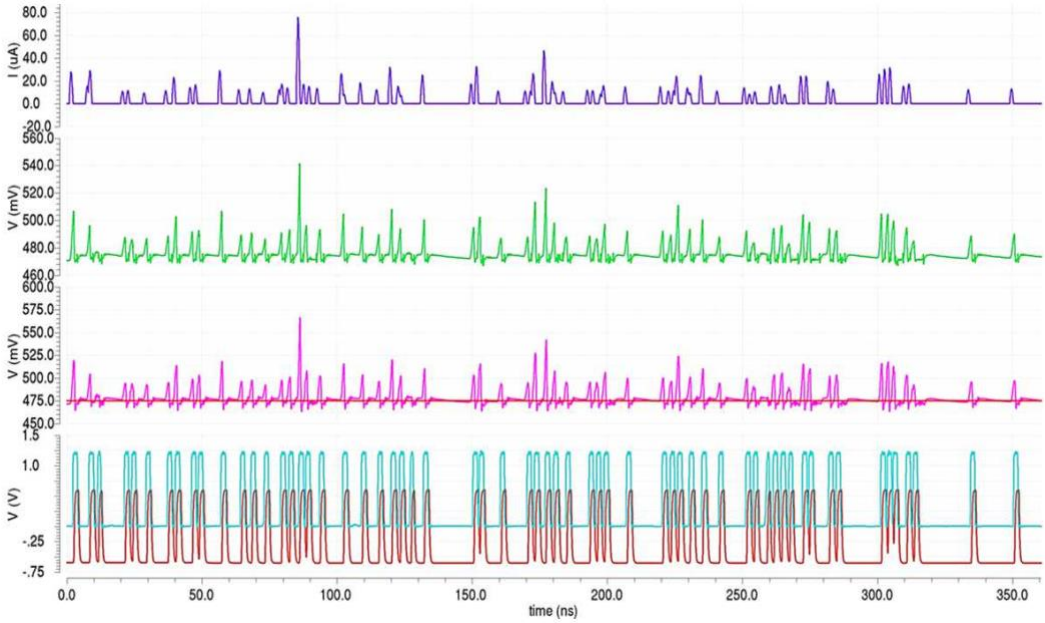

Figure 2.9 Schematic simulation waveforms for 250 MeV protons at 250 MHz. From the top: the input signal, the CSA output voltage, the buffer output voltage, the discriminator output

A dedicated motherboard for testing the system including both ASIC and UFSD sensors has been designed and developed (Figure 2.10).

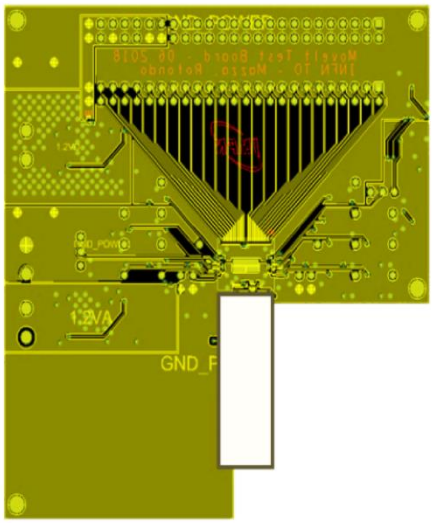

Figure 2.10 Top view of the ABACUS test board, with the strip sensor placed in the board inner

The PCB layout is shown in the Figure 2.10. The geometry of this PCB has been modeled with the idea to glue the silicon strip sensors on two edges, in order to do not have the board layers in the particle path. The ABACUS readout is based on an FPGA connected to the motherboard, where the number of logical CML pulses in output from the ABACUS chip are counted for each channel.

In the laboratory tests input charge pulses were injected to the ASIC inputs through dedicated capacitances. The ASIC was tested in terms of linearity, noise level and efficiency at high pulse rates.

Pulse detection with full efficiency has been obtained for injected charges between 3 fC and 160 fC. The output voltage from the amplifier and the noise were estimated by the measurement of the number of detected pulses as a function of the threshold value. The results are shown in Figure 2.11 for charges between 3 fC and 20 fC.

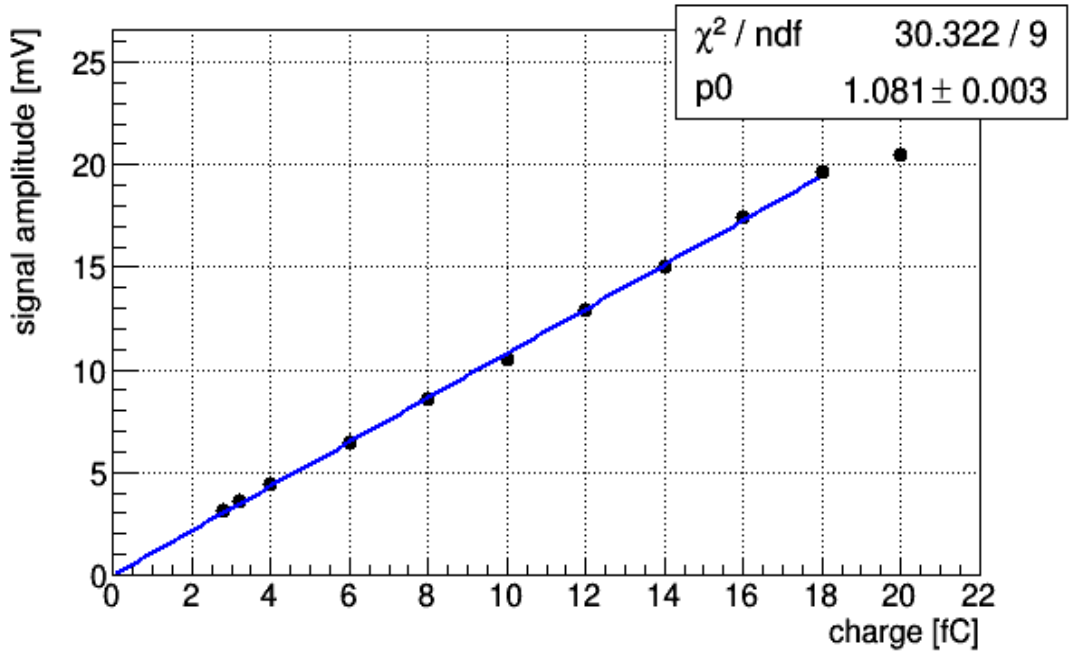

Figure 2.11 Amplitude of the amplifier output signal as a function of the charge injected at 1 MHz rate

The measured noise rms is 0,36 mV, corresponding to a minimum signal-to-noise ratio of 10 at the lowest charge. A counting efficiency higher than 98% up to 100 MHz was measured.

Chapter 3

Characterization of the MoVe-IT strip sensors in laboratory

3.1. Introduction

This chapter describes the part of the work performed within this thesis for a preliminary study of the properties of the MoVe-IT strip sensors described in the previous chapter.
A first set of measurements were intended to characterize the behavior of each channel, using static measurements performed with a probe station and a multichannel analyzer. In a second step, the signal produced by a pico-second laser has been studied, and the gain level of the sensors (sect.3.4). The most promising strip sensors are therefore tested with therapeutic proton beams, to characterize their behavior in a realistic environment; this is the subject of the next chapter. In most of the work described in the thesis, the front-end readout based on the ABACUS chip was not ready yet and all the tests were done using a passive board which allow to bias the sensor at high negative voltages. The output of two channels were amplified by broadband amplifiers, while the rest of the strips were grounded to reduce the superficial current. The amplifier signals were collected by a fast digitizer or oscilloscope and saved on disk.

3.2. Laboratory setup

The setup used for the sensor characterization consists of the following components:
- Probe station with card holder
- Keysight Technologies: Source/Measurement Unit (SMU)
- Technoprobe: multi needles Probe card
- Keithley: Switching matrix
- National instruments LabVIEW software

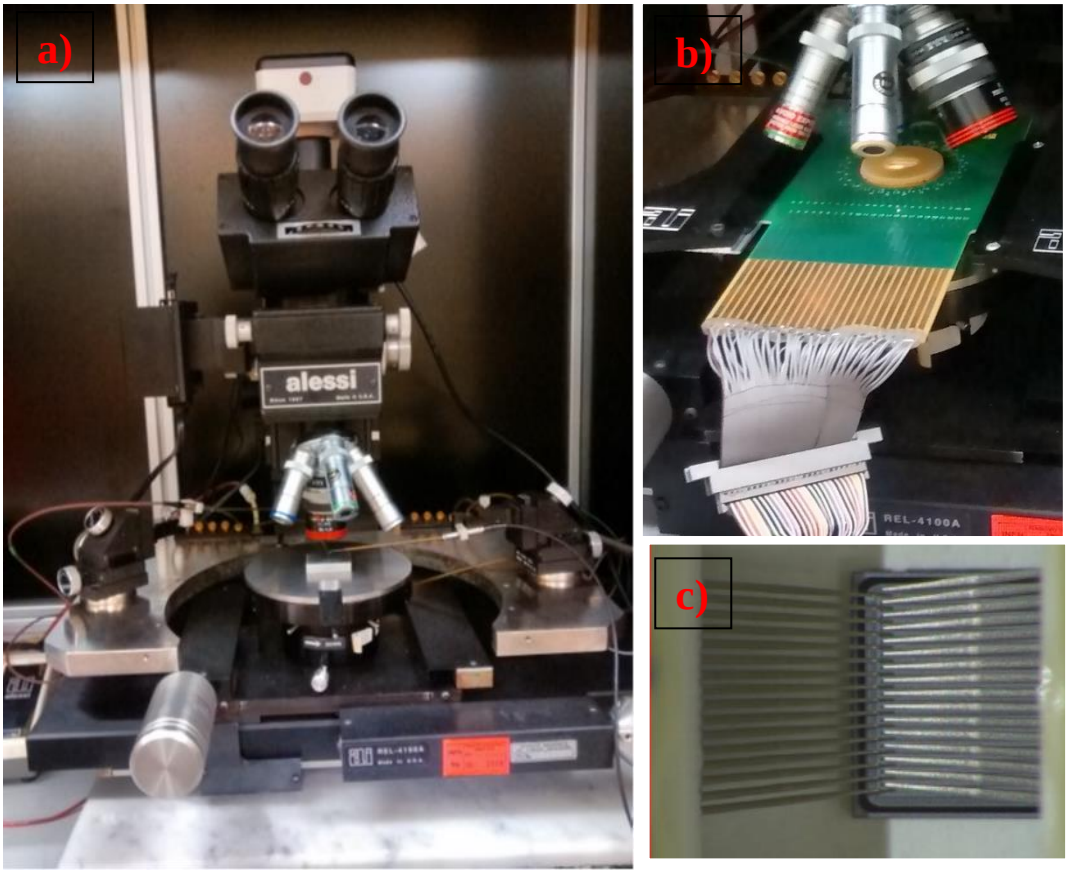

Figure 3.1 a) probe station, b) probe card, c) needles in contact with strip UFSD

3.2.1 Probe station and SMU unit

All the measurements were performed with a probe station (Fig. 3.1) connected to a source/measurement unit (SMU) (Fig 3.2).

Figure 3.2 Left: Keysight Technologies Source/Measurement Unit (SMU), Right: switching matrix

The SMU is a Power Device Analyzer / Curve Tracer, model Keysight B1505A [27], consisting of a single box solution used to provide the HV to the sensor and measure currents and capacitance from the contacts of the probe station pins.
The SMU Analyzer is equipped with three modules:

• High Voltage Source Monitor Unit B1513C (HVSMU), with a range up to 3000V and 8mA;
• Medium Power Source / Measure Unit B1511B (MPSMU), with a range up to 100V/0.1 A and a minimum measurement resolution of 10fA/0.5μV;
• Multi Frequency Capacitance Measurement Unit Module B1520A (MFCMU), with a frequency range from 1 kHz to 5 MHz and an AC signal level of amplitude up to 250mV.

The device enables precise μΩ resistance measurements and provides 10 μs fast pulses for transient measurements. The SMU can be programmed to generate a ramp of bias voltages and to measure for each V_{bias} value the current and capacitance and automatically saving the results in files or in graphs.

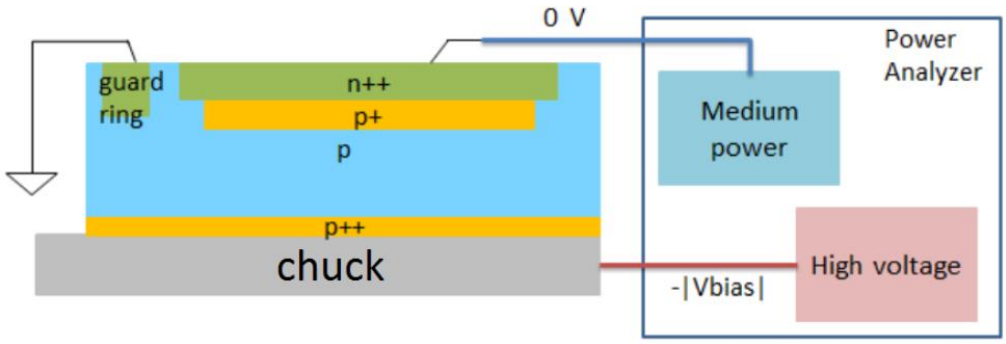

Figure 3.3 scheme of the probe station connections to a single pad

Figure 3.3 shows the contacts of one sensor channel: a high negative voltage is provided by the HVSMU module to the p++ backplane of the sensor through its contact with the chuck of the probe station, while the sensor guard ring is connected to ground. The n++ electrode is connected to the MPSMU monitor unit.
The chuck is provided with a vacuum pump in order to hold the sensor on a fixed position and assure a proper contact.

The measurements of the current as a function of the bias voltage (I-V curves) provide information on device parameters like depletion voltage, leakage currents, sensor gain and breakdown voltages. The measurement of the capacitance as a function of the bias voltage (C-V curves) adds important information on the doping profiles.

The probe station is enclosed inside a dark box to avoid the noise coming from light impinging sensors. Measurements were always performed at room temperature. The tests of all the strips of the entire set of MoVe-IT strip sensors produced by FBK were performed using a matrix unit and a multi-needle probe card.

3.2.2 Probe card and matrix unit

A dedicated probe card and a switching matrix module were used to test automatically all the strips of each sensor.
A switching matrix consists of a series of inputs and outputs; connections between the inputs and outputs can be made by closing one or more relays. While the number of inputs on a switching matrix is fixed, the number of outputs is usually determined by the number of cards installed in the matrix mainframe. A matrix unit (Keithley 7002) [28] (fig. 3.2 right) was used to connect the SMU to a multi needle probe card used to probe all the strips of a sensor and automatically analyze all the channels one after the other.
A dedicated LabVIEW [29] software was used to configure the matrix unit, to synchronize the matrix unit with the SMU operations, to collect and save the I-V or C-V curves measured for each strip. To accurately measure the current from the connected strip, the remaining strips are grounded especially the ones on the edge of the sensor.

Two custom probe cards were produced with the geometry of the needles matching the number and the pitch of the contacts on the two types of strip sensors. They are passive printed circuit board (PCB) with multiple needles with tips of few µm to give a good connection to the sensors pads with the minimum contacting area (Fig 3.4).

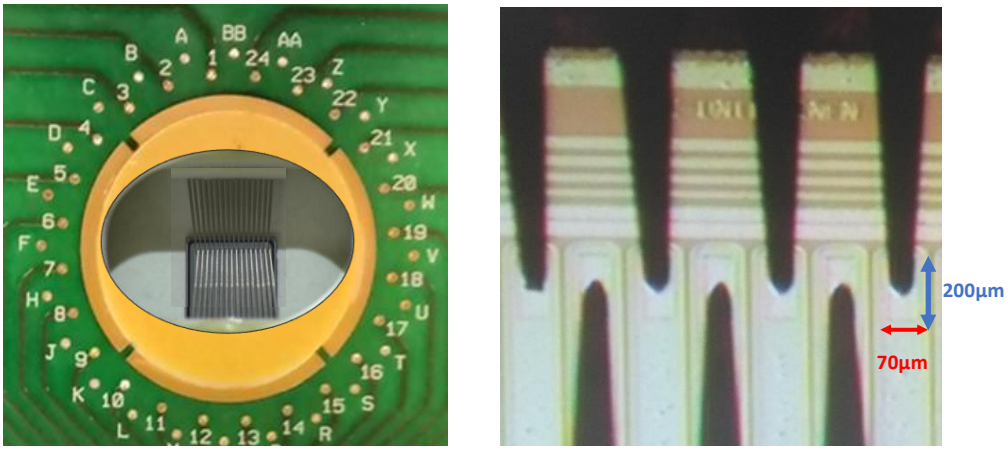

Figure 3.4 Left: Probe card with needles connected long strip pads; Right: zoom showing the orientation of needles and their contacts on the strip pads

The probe card assures an electrical path between the needles and the input channels of the matrix unit through a flat cable.
Before the strip sensor arrived, I was in charge to prepare the test setup and to provide to the manufactory company “Technoprobe” all the information needed to customize the probe card design on the base of the strip sensors design. The probe card for the long and short strip sensors have 32 and 22 needles, respectively. The two extra tips with respect to the number of strips are used to connect the guard ring to ground.

3.3. IV curves

I-V curves are derived for each strip by measuring the two currents (one current from the strip, the second one from the guard ring) as a function of the bias voltage. These curves allow to determine the value of the full depletion voltage, to investigate the presence of superficial currents, and the voltage value above which an avalanche starts to be produced in the sensor (breakdown voltage).

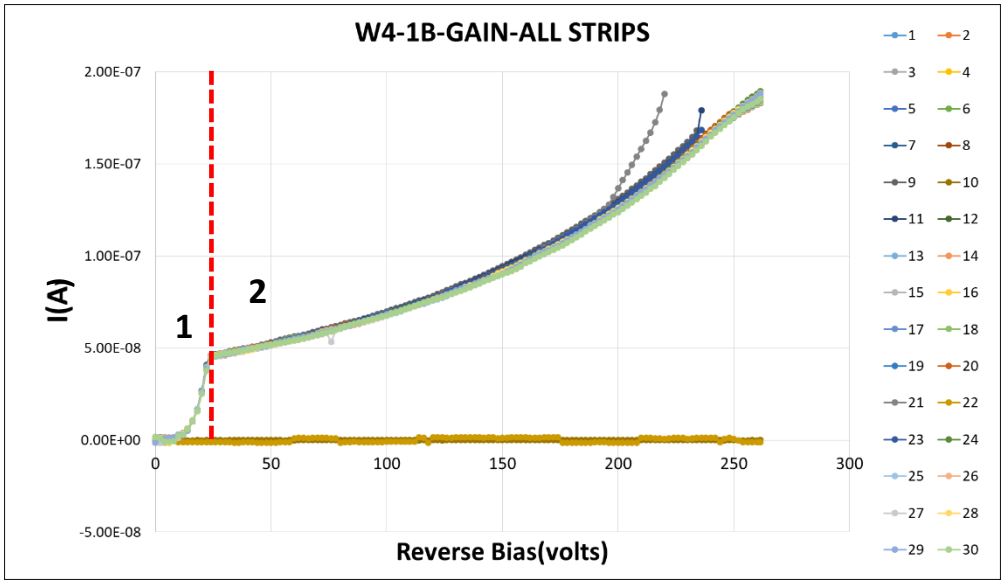

Figure 3.5 IV curves for a reversely biased multi strips LGAD sensor (long strips)

Figure 3.5 shows an example of IV curves collected for different strips of a sensors from wafer no.4 (Table 2.1). The typical I-V curve for the strip current is composed of two regions separated by a "knee”. In the first region (1 in Figure) the current increases with the square root of the applied voltage The knee corresponds to the full depletion of the sensor (at about 25 V), and above the full depletion voltage the current increases slowly with the V_{bias} until it reaches the breakdown. From the measurements shown in Figure 3.5

two strips starts to exhibit a breakdown behavior at a bias voltage lower than the others, preventing the use of this sensor at a bias voltage above 200 V.
The purpose of these measurement (performed on all the strip sensors produced by FBK), was to identify abnormalities in some strips like the ones of the example before, and to select only sensors with uniform behavior. It must be mentioned that a good and uniform behavior is observed for most of the sensors.

Figure 3.6 shows the mean currents measured from the strips of all the short sensors of Wafer 8 as a function of the bias voltage, after removal of the sensors with some problematic strip. The lowest I-V curves refer to sensors without gain layer: for these sensors, the current is approximately independent of the bias voltage.

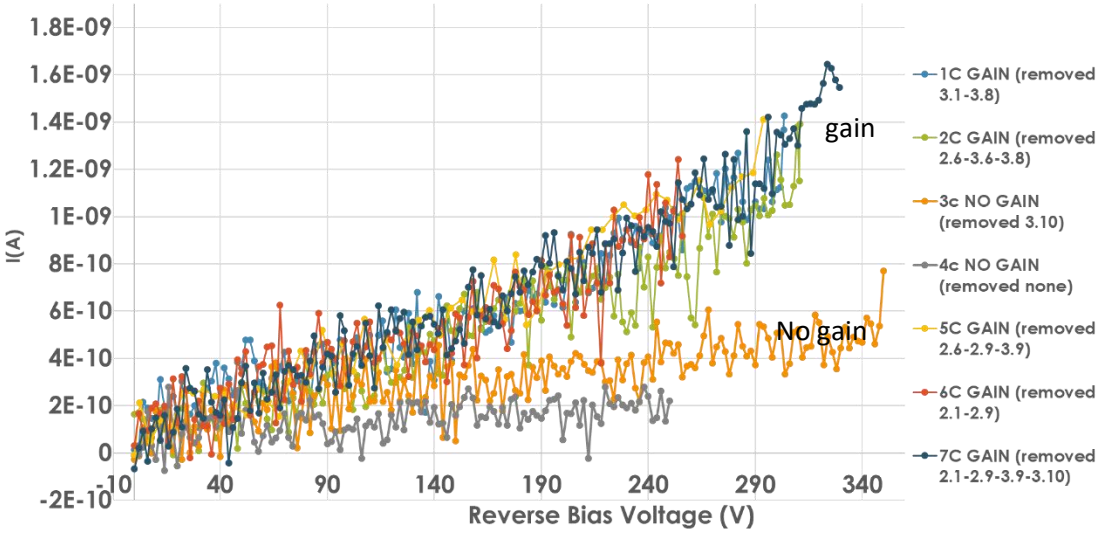

Figure 3.6 IV curves for all short strip sensors from W8

For the other UFSD sensors with gain layer, the current increases with the bias voltage. This is due to the multiplication of the minority charges thermally produced in the sensor bulk which depends on the electric field in the gain region.
The comparison of the slopes of I-V curves from UFSD sensors with gain with respect to the sensors without gain layer and the same geometry provide an indicative value of the gain factor. This measurement has not been performed in this study: a more precise value of the gain factor was instead obtained by comparing the output signals from sensors with and without gain, using laser pulses to emulate the effect of particle crossing or with real particles.

3.4. C-V curves

Interesting information come out from the measurement of the strip capacitance as a function of the applied polarization voltage. The procedure for taking C-V measurements involves the application of DC bias voltages across the sensor capacitance while making the measurements with an AC signal. Commonly, AC frequencies from about 10kHz to 10MHz are used for these measurements. The bias is applied as a DC voltage sweep that drives the structure from its accumulation region into the depletion region and then into inversion.

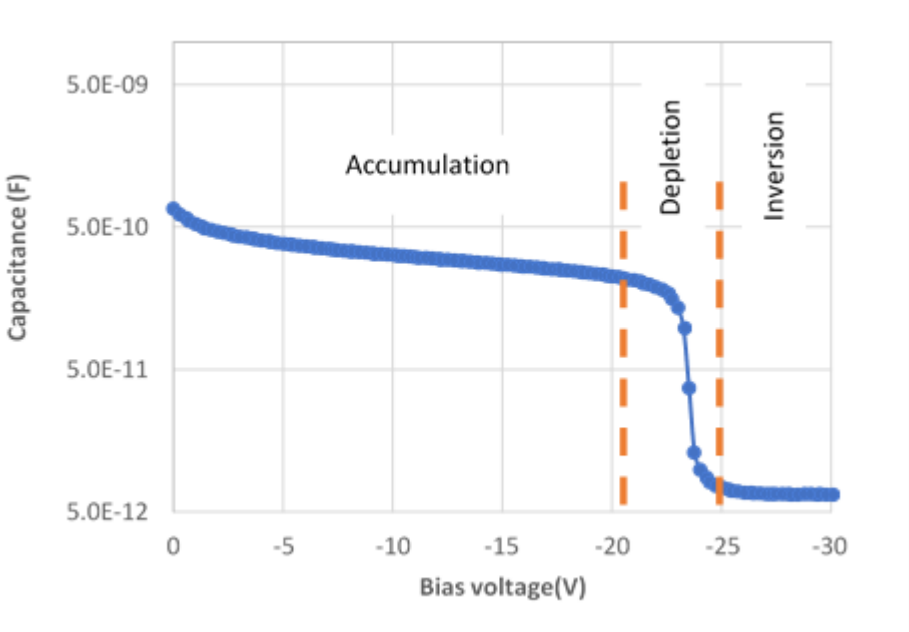

Figure 3.7 CV curve for a sensor from W4

The capacitance of several strips has been measured as a function of V_{bias} with at 10 kHz AC signal. One example is shown in Figure 3.7.
The C-V curve allows to determine precisely the value of the depletion voltage and to estimate the doping profile. The dependence of the capacitance on the acceptor density N_A and on the bias voltage V_{bias} for a sensor of active area A is given by:

$$C = A\sqrt{\frac{e\epsilon\mu_h}{2V_{Bias}} \cdot N_A} \qquad \textbf{(3.1)}$$

where e, ε, μ_h are the electron charge, the permittivity and the holes mobility respectively.
In addition, the dependence of the full depletion voltage on the width of the depletion region is:

$$V_{dep} = \frac{d^2}{2\epsilon\mu\rho} = \frac{d^2}{2\epsilon} \cdot qN_A \quad \textbf{(3.2)}$$

where d is the thickness of the depletion region.
These equations state that the capacitance of a sensor is proportional to the square root of the depth. Moreover, it is noticeable that the depletion voltage V_{dep} is proportional to the doping concentration.

The ideal C-V characteristic of a standard PN diode is a $1/\sqrt{V_{bias}}$ curve which becomes constant when the sensor is fully depleted and the capacitance reaches a constant value

$$C = \varepsilon \frac{A}{d} \quad \textbf{(3.3)}$$

The voltage value at which the capacitance becomes constant is the depletion voltage. If one extracts from the C-V curve the depletion voltage and knows the sensor thickness, the doping concentration of the bulk can be determined. according to Eq. 3.2, the higher the doping concentration is, the higher will be the depletion voltage.

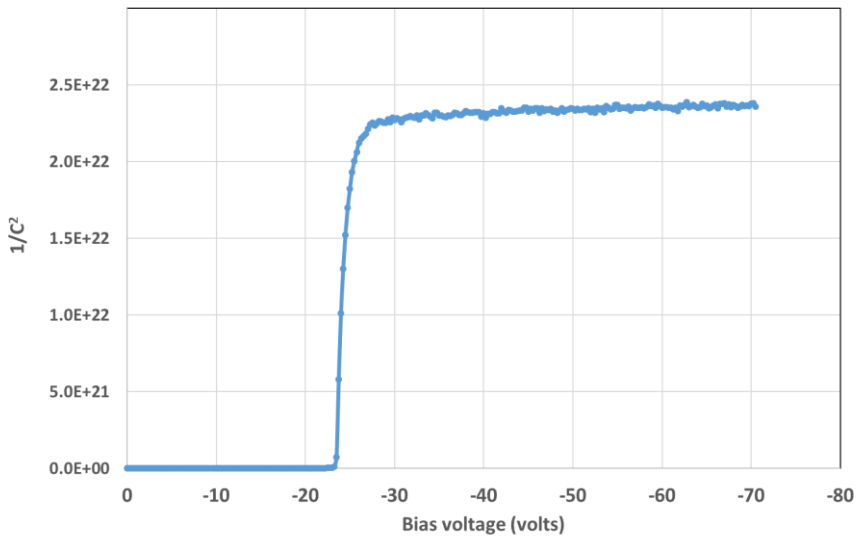

Figure 3.8 $1/c^2$ as a function of the bias voltage

When the inverse bias voltage starts to increase, the first region to be depleted is the gain layer: this region is fully depleted at few tenths of volts. The depletion voltage of the gain layer (the "knee", called in this way because of the shape of the curve in this point) is proportional to its doping concentration: one can compare the doping concentrations of different devices simply evaluating their gain layer V_{dep}. When the gain layer volume

is fully depleted, the bulk depletion begins, which coincides with the second region of the C-V curve.
Full depletion of the bulk is reached in a few volts because, although it is thicker than the gain layer, its doping concentration is much lower. The capacitance values of the depleted region under one strip of the sensors produced for particle counting application are:

Capacitance (pF)	One strip	Two strips
Short strip	6.3	13
long	6.5	15

Table 3.1 capacitance measurement for short and long MoVe-IT sensors

In agreement with the expected values. The capacitance measured for two strips connected in parallel is little more than the sum of the capacitances of the single strips due a little interstrip coupling capacitance.

A profile of the acceptor doping concentration N_A can be estimated from $1/C^2$-V curves. From Eq.3.1, the dependence of $1/C^2$ over V_{bias} for $V_{bias}<V_{dep}$ is given by:

$$\frac{1}{C^2} = \frac{2V_{bias}}{e\varepsilon\mu_h A^2} \cdot \frac{1}{N_A} \tag{3.4}$$

and it reaches a constant value when the detector is fully depleted. For a given depletion thickness d, the capacitance is also given by Eq. 3.2.
For a given V_{bias}, Eq. 3.2 allows to extract the depth in the silicon where the depletion region was extended, while the derivative of Eq. 3.4 with respect to V_{bias} determines the acceptor concentration at depth d.
An example of results from this analysis is shown in Figure 3.9, where the acceptor concentration is estimated as a function of the depth in the strip.

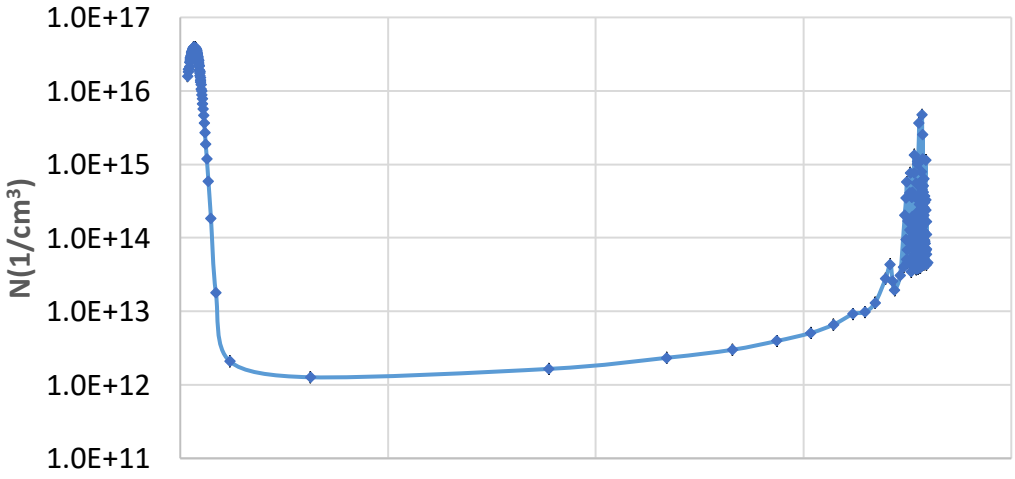

Figure 3.9 Doping profile, acceptor doping concentration as a function of the sensor depth

The first peak extended up to 1-2 µm inside the sensor correspond to the p+ gain layer implanted below the n+ electrode. The flat region gives to the dopant concentration of the sensor bulk, while the last peak in figure is the dopant concentration of the p+ electrode in the backplane. The measured values of the dopant concentration are compatible with the design values expected after the implantation.
These measurements were performed only on a few samples of the sensor batch produced for the MoVe-IT project. More extended studies have been done on irradiated PINs of the same wafers to study the effect of irradiation on the UFSD gain, and will be summarized in Section 3.7.

3.5. Readout for signal shape acquisition

On the basis of the previous characterization, sensors are sorted according to their functionality within a range of bias voltage where they are supposed to have a good gain value of about 10 with acceptable dark current and quite far from the breakdown limit, Sensors with strange behavior, low reliability, or anomalous strips are rejected.

Although these UFSD sensors have the additional doping layer to enhance the signal formed by particles crossing them, the level of signal is still so low to require another amplification stage using addition preamplifiers. During the sensor tests described in the following, the ABACUS chip dedicated to the readout of the strip sensors and described in the previous chapter was still in a design phase and a temporary solution to acquire signals from the sensors to continue their characterization was needed.

Several options were tested for the acquisition of the sensor signals, based on readout boards with external amplifiers or on readout boards housing internal preamplification stages with discrete component circuits. A passive custom board was already designed by INFN Torino to test the first UFSD PINs produced for timing applications. This board (shown in Fig. 3.10) is designed to distribute the bias voltage produced by a HV power supply to the sensors and to connect up to 2 channels to external amplifiers.
The only solution that allowed to readout accurately the signal shapes avoiding long recovery times and tails was the use of the passive boards described before coupled to external broadband amplifier produced by Cividec [30]. These are low-noise current amplifiers with an analog bandwidth of 2 GHz and 40 dB gain.

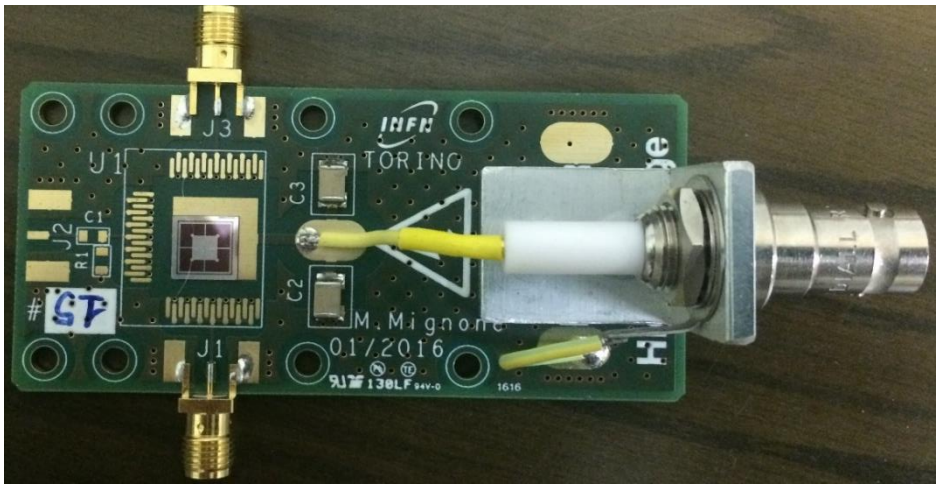

Figure 3.10 Two channels passive board made by INFN Torino with 2x2 pads UFSD connected

Other boards with internal amplification stages were produced by external institutions and available in our institute (Santa-Cruz, CERN).
In order to test the best readout options, a fast-pico-laser (PiLas) [31] providing fast pulses (few tens of ps) at 1060 nm wavelength was available. The silicon is transparent to the infrared wavelengths, and therefore these pulses can produce charges in the silicon, emulating the behavior of charged particles crossing the sensor.
The sensor is usually fixed on a motorized 3d stage with a movement precision of the order of one micrometer which allow the precise and accurate positioning under the laser spot. The laser pulse is propagated through an optical fiber and focused to a small spot of less than 10 μm with a lens mounted at the end of the fiber
A typical test bench to test the laser with pico-laser pulses is shown in Fig. 3.11.

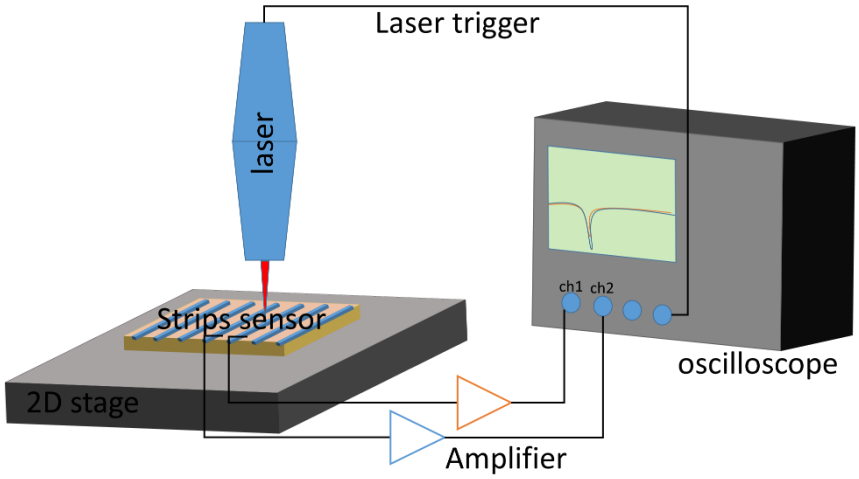

Figure 3.11 Scheme laser setup

The laboratory setup consists of:

1. Picosecond laser (PiLas) by Advanced Laser Diode Systems with controller EIG2000DX, wavelength 1060 nm, simulating a MIP
2. Oscilloscope (LeCroy, sampling frequency 2.5 GHz)
3. Power supply (Keithley 2410)
4. Cividec amplifier 40db

In order to avoid laser reflection, the presence of an optical window on the top metal layer of the sensor is necessary. The sensors produced for the MoVe-IT project have a continuous metallization contact covering all the strip area which does not allow to use a laser beam for simulate the effect of charged particles. Other PINs structure produced by FBK in the same wafers together with the MoVe-IT strip structures with optical apertures in their electrode metallization were used to test the readout chain.

A typical signal from a UFSD PIN collected with the oscilloscope in coincidence with a laser pulse is shown in Fig. 3.12.

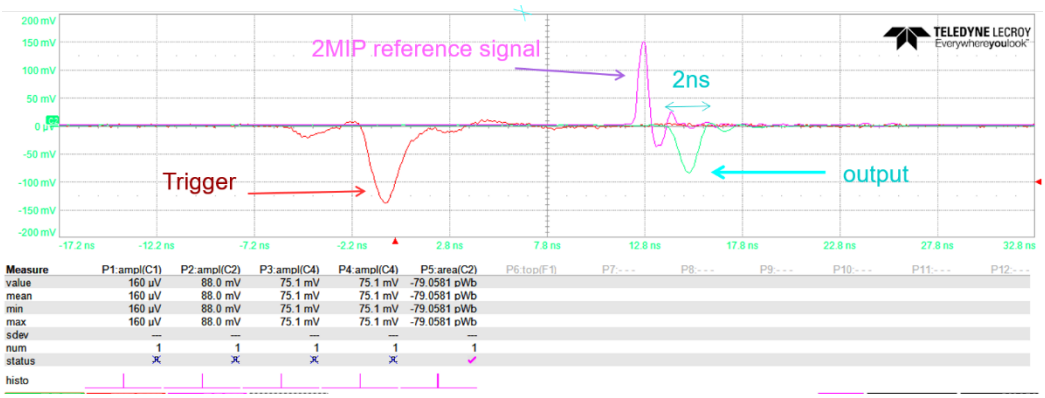

Figure 3.12 Oscilloscope screenshot showing the amplified signal from a UFSD PIN (green), reference diode (pink) and the laser trigger signal (red)

The laser setup was used to collect signals from the PINs connected to several boards with integrated amplification. However, their performance was not optimized for a counting application because all these boards were designed for timing applications, requiring the reduction of signal jitter at the price to introduce quite large time constants and recovery times. The signals in output from these integrated amplifiers were not short enough for counting applications at high rates. At the same time, the baseline restoring of almost all of the tested boards were not fast enough to avoid dangerous baseline shifts during the acquisition of particle bursts.

3.6. Measurements with laser pulses

As already mentioned in the previous section, the strip sensors produced for the MoVe-IT project have no optical window on the aluminum layer over the strips, and therefore it was not possible to test directly the signals with laser pulses sent to the top of the sensors.
In the absence of an optical window, a laser scan was performed with the laser beam sent to the side of the sensor (Fig. 3.13) instead than to the top.

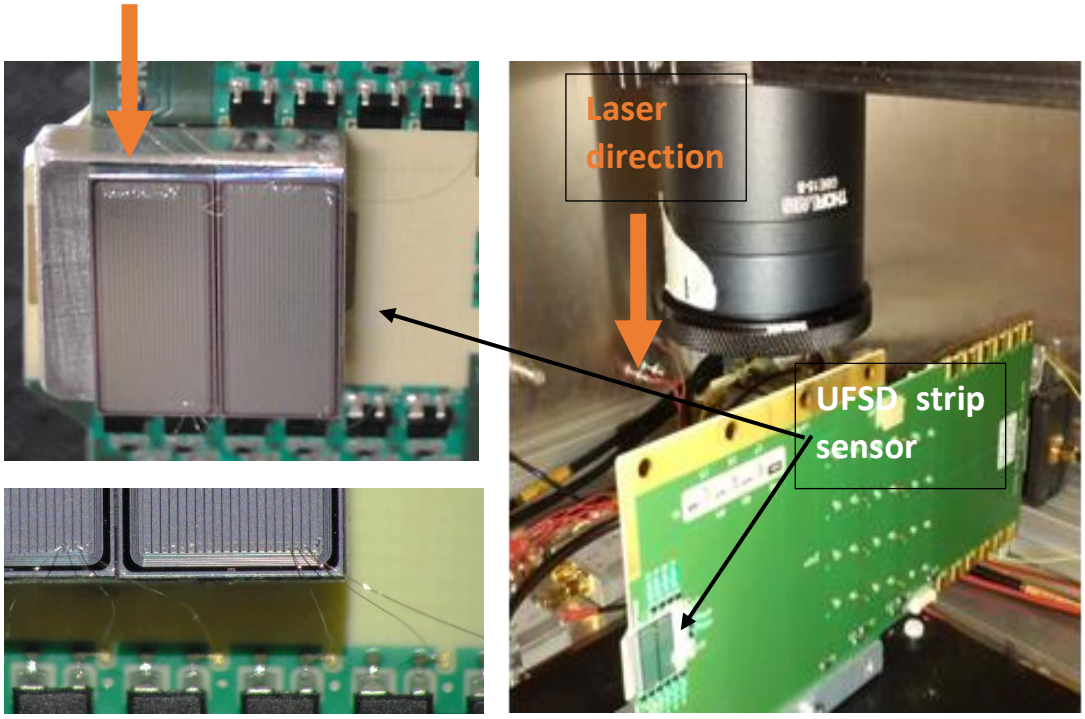

Figure 3.13 Two vertical strips sensors bonded on an active board, with the laser irradiated from the top

This test permitted to probe the internal structure of the sensor like the zone between two strips and to estimate the gain of the sensor defined as the ratio

of signals from sensors with gain and without gain with the same geometry and same bias voltage.

Two adjacent strips of a short strip sensor have been connected to an active board with internal amplifier and the output signals were readout with an oscilloscope. Another short strip sensor without gain layer was connected to other two strips of the same readout board. The laser spot was focused with a spot diameter of less than 8 µm and moved with 2 µm steps in both the directions orthogonal to the strip length, and the amplitude of the output signal for fixed laser pulses was measured for each spot position. The results are shown in Figure 3.14.

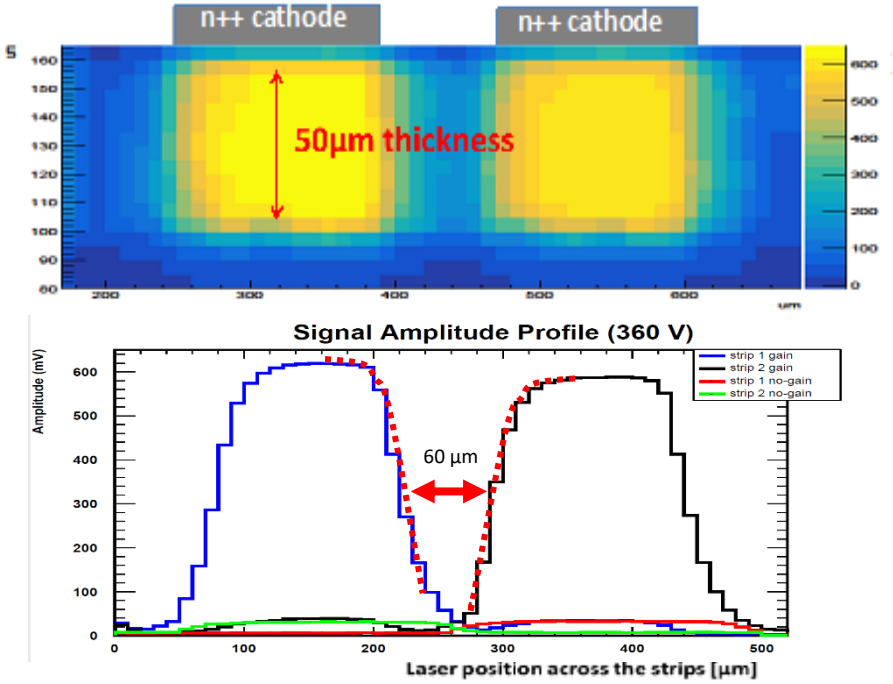

Figure 3.14 Top: 2D dependence of the signal amplitude measured as a function of the position in two orthogonal directions orthogonal to the strip length for a sensor with gain. Bottom: a profile of the signal amplitude for a fixed vertical position for the two strips of a sensor with gain (blue and black) and for a similar sensor without gain (red and green)

The vertical and horizontal axes correspond to the two coordinates of the laser spot on the sensor and the color scale to the signal amplitude at each point. In this scan the vertical position corresponds to different depths in the sensors below the strip contact, while the horizontal position covers two strips and the region between the strips. The enhanced signal from the two strips is clearly visible, while the signal in the dead region between two strips is strongly attenuated.

The bottom part of the figure shows the dependence of the signal amplitude on the horizontal position for a fixed depth in the sensor. The blue and black curves are the signal amplitudes measured with two strips with gain, while the green and red lines are the amplitudes from two strips of a similar sensor without gain.
The distance from the two signals obtained at half maximum is 60 µm, in agreement with the results expected from the TCAD simulation in the design. A little amount of cross talk is visible, when the laser is fired on one strip and a small signal is observed in the neighboring strip. This effect is probably due to the diffusion of the laser beam inside the sensor.

The signal amplitudes measured for a LGAD strip sensor and a sensor without gain when the laser beam is focused on the strip central position are used to measure the gain. The gain factor of the UFSD sensor is defined as the ratio of the output signals from the two sensors at the same operating parameters, and is shown in Fig.3.15 as a function of the bias voltage. The gain factor increases with the bias voltage, and the nominal value of 10 is obtained with a bias voltage of about 320 V.
A better estimation of gain value is obtained by using particles from a therapeutic beam, as described in the next chapter.

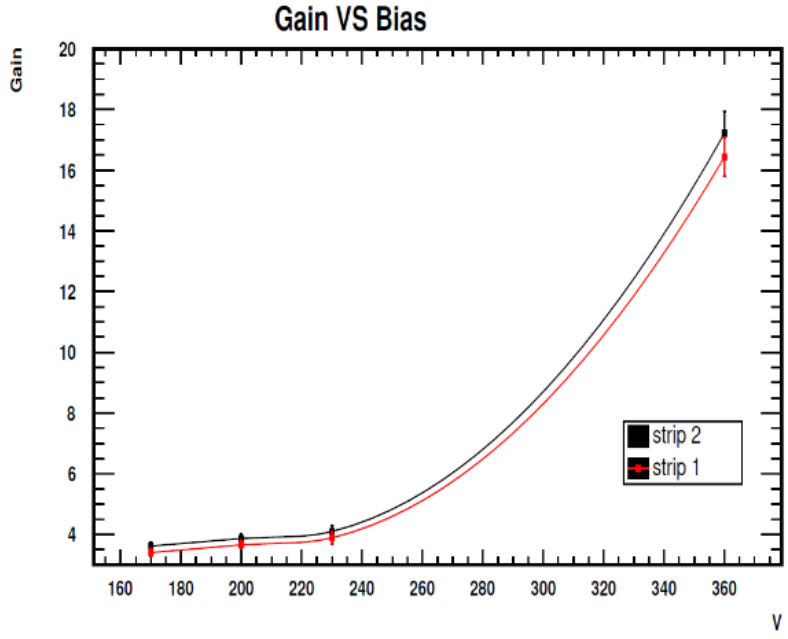

Figure 3.15 Gain value of two neighboring strips in function of the negative bias voltage

3.7. Radiation resistance of UFSD structures

Some of the UFSD structures produced in the same wafers together with the MoVe-IT strip sensors have been irradiated with neutrons up to a fluence Φ_n~3x10^{16} n/cm^2 (Ljubljana) and with high energy protons up to Φ_p~9x10^{15} p/cm^2 (CERN), to test their radiation resistance. Our colleagues in Torino working on UFSD development have studied the effect of radiation on the performance of structures from different wafers produced with alternative doping modalities. The main results of these tests are reported here [32].

Both neutrons and protons produce a reduction of gain in the LGAD sensors, due to deactivation of the acceptors forming the gain layer ("acceptor removal" mechanism). Concurrently with the acceptor removal mechanism, irradiation causes also the creation of defects and traps in the sensor bulk. These two effects are parameterized by the following equation:

$$\rho_A(\Phi) = g_{eff}\Phi + \rho_A(0)e^{-c\Phi} \quad \textbf{(3.5)}$$

where Φ is the irradiation fluence in cm^{-2}, $\rho_A(\Phi)$ is the acceptor density in cm^{-3}, g_{eff} a constant (g_{eff}=0,02 cm^{-1}) and c is a parameter describing the acceptor removal mechanism. The parameter c depends on the initial acceptor density $\rho_A(0)$ and on the type of irradiation.

The density of active acceptors in the gain layer can be measured from 1/C^2-V curves as described in Section 3.4. The main results are summarized in Fig.3.16 (neutron irradiation) and Fig.3.17 (proton irradiation). In both the figures, the fraction of active acceptor density ($\rho_A(\Phi)/\rho_A(0)$) is reported as a function of the fluence for sensors from different wafers. The lines in the figure are fits to the data according to Eq. 3.5.

From these results it emerges that a higher gain reduction is observed when Gallium is used as acceptor with respect to Boron. In both the cases the addition of carbon in the gain layer improves the radiation resistance. Moreover, a thermal cycle with low diffusion is helpful in improving the radiation resistance. In general, narrower and more doped gain implants have a higher resistance to the radiation dose.

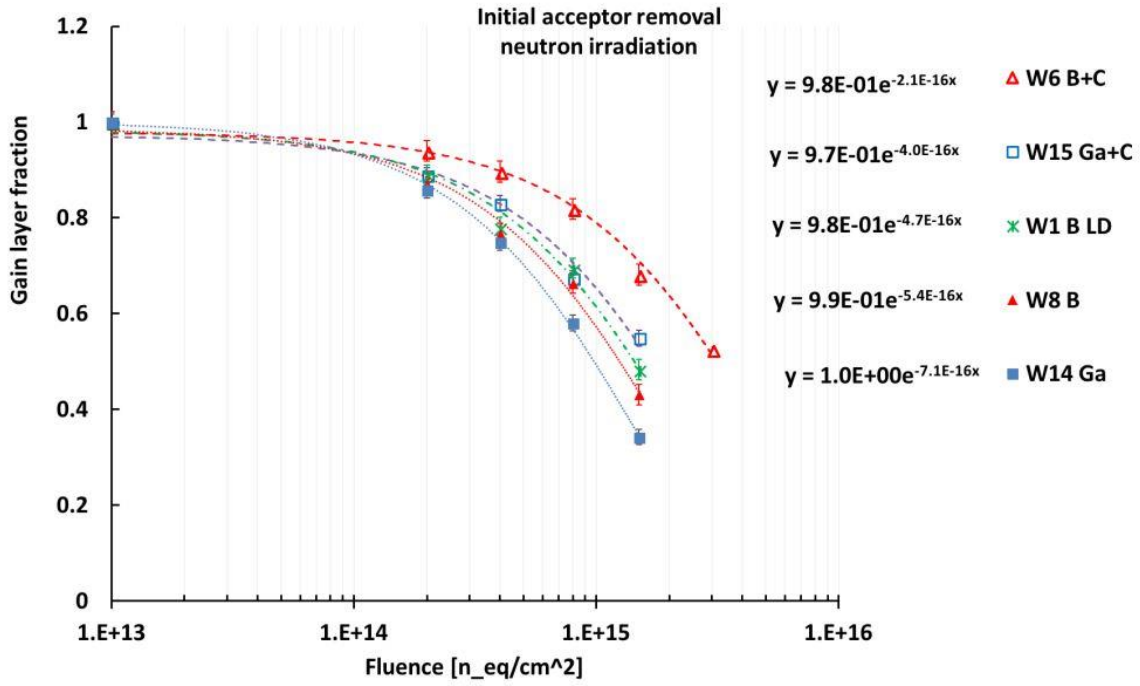

Figure 3.16 Fraction of active gain layer as a function of the neutron fluence

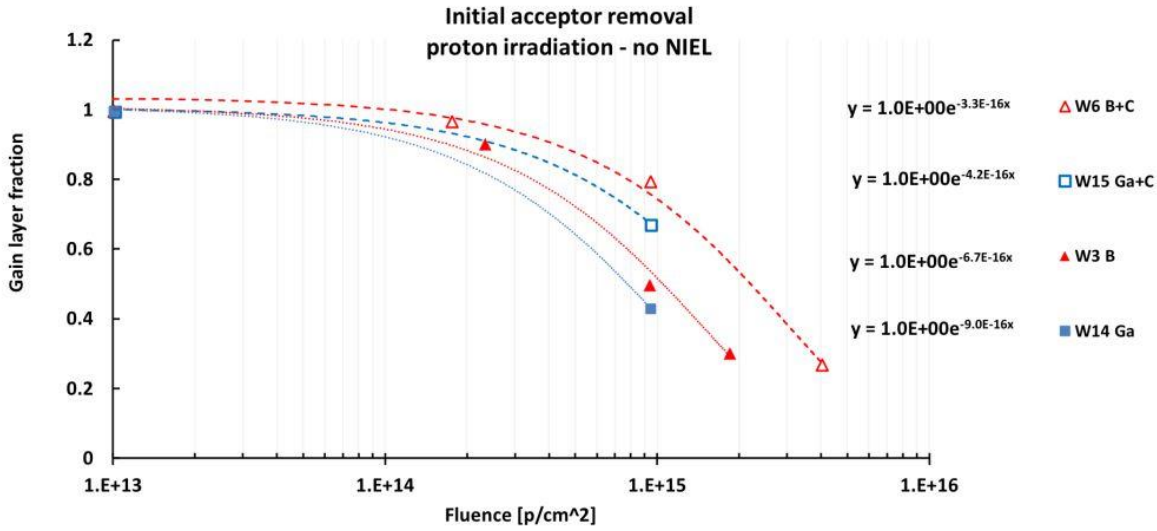

Figure 3.17 Fraction of active gain layer as a fraction of the proton fluence

Chapter 4

Test of UFSD strip sensors with therapeutic beams

4.1. Introduction

The silicon strip sensors described in the previous chapters have been tested with therapeutic proton beams of the Centro Nazionale di Adroterapia Oncologica (CNAO) and Proton Therapy Center of TIFPA (Trento, Italy). A few strips have been readout using external broadband amplifiers and a digitizer to collect the signals. From the collected data the stability of the device, its discrimination properties, and counting capability were studied. An independent estimation of the counting rate was obtained with the use of a pinpoint ionization chamber positioned behind the sensors and compared with the counting rate measured with the strip sensor for different beam energies and fluxes.

4.2. Beam characteristics of CNAO and TIFPA.

At the Centro Nazionale di Adroterapia Oncologica (CNAO) in Pavia, Italy, a synchrotron is used to accelerate protons and heavier ions to treat tumors with a full active delivery system [33]. Three beam transport lines guide the beam into one of the three treatment rooms (Fig.4.1). Two rooms are equipped with a single horizontal fixed beam line, while in the third one, a horizontal and a vertical fixed beam lines are available. Each room includes the beam nozzle with monitor chambers, the patient positioning and immobilization system [34].
An additional beam line will be available in 2020 to distribute the beam in an experimental room.

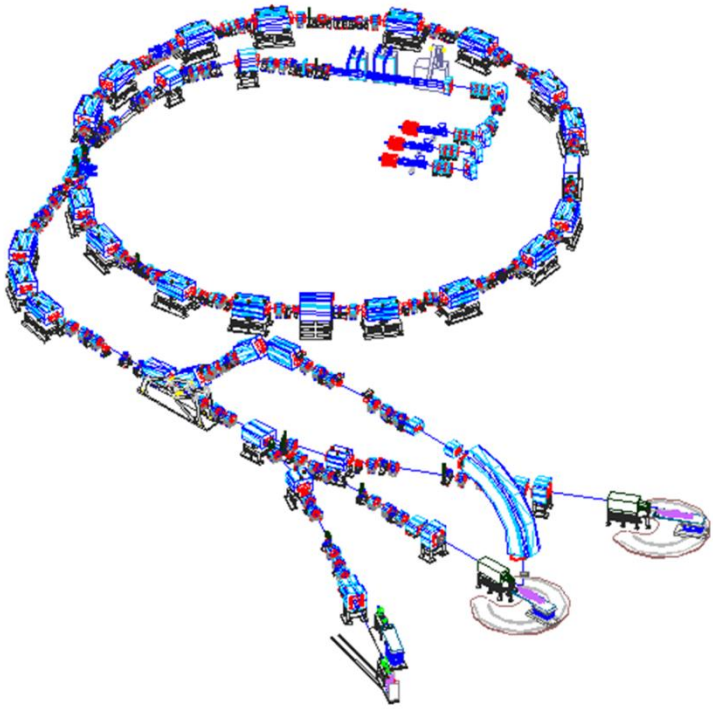

Figure 4.1 Scheme of the CNAO beam delivery, with the beam distributed in three treatment rooms. The beam line to the experimental room is not shown in the picture.

The beam energy can be selected within a set of values between 120 MeV/u and 400 MeV/u for carbon ions (C^{+6}) and between 60 and 250 MeV for protons (p), corresponding to a range in water between 3 cm and 27 cm, selectable with 0.1 cm steps.

The particles acceleration and extraction in the synchrotron has a cyclical behavior. Each cycle has a pre-configured events sequence, always with the same structure, but a different setup for different particles, energies, beam intensity and dimension. The delivery phase is known as spill and in order to provide a whole volume irradiation, several beam energies have to be shot providing spills in a periodic sequence (Fig. 4.2).

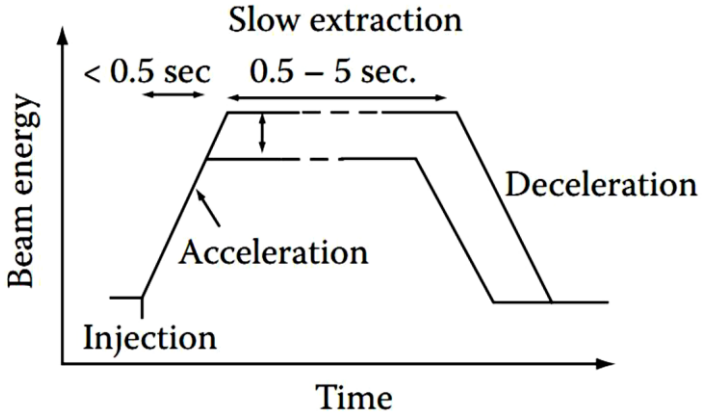

Figure 4.2 Spill schematic: the injected particles are accelerated to the desired energy and extracted slowly

The time period ranges between 4 and 5 seconds, with an approximate spill length of 1.5 sec, with the inter-spill time needed to setup the machine magnets for the following beam. The accelerator can provide a maximum of 4×10^{8} C^{+6} or 10^{10} protons per spill, leading to a maximum beam current on the patient of 0.38 nA and 1.6 nA respectively.

The measured full width at half maximum (FWHM) of the pencil beam transverse shape in air at the isocenter is energy-dependent for both the particle species: in particular, for protons, the spot size ranged from 0.7 to 2.2 cm. For carbon ions, two sets of spot size are available: FWHM ranged from 0.4 to 0.8 cm (for the smaller spot size) and from 0.8 to 1.1 cm (for the larger one). The corresponding beam fluence rate ranges between 10^{9} p/(cm^2·s) and 10^{10} p/(cm^2·s) for protons, depending on the FWHM and extraction settings, and between 4×10^{7} and 4×10^{8} for carbon ions [35]. The spot position is accurate within ± 1 mm over the whole 20 × 20 cm^2 scan field; homogeneity in a uniform squared field was within ± 5% for both particle types at any energy [36].

Another italian treatment facility is the Proton Therapy Center (PTC) of TIFPA at Trento [37], built by the commercial company IBA [38], and based on a Proteus 235 cyclotron, which accelerate protons at an energy of 228 MeV. Shortly after the cyclotron exit, a coarse energy selection is carried-out by a rotating degrader of different thicknesses and materials and a magnetic energy selection system in order to provide different beam energies down to the minimum value of 70 MeV.
The facility has two treatment rooms equipped with rotating gantries while a third experimental room is totally dedicated to research [39]. The beam

cannot be shared simultaneously among the different rooms and can only be requested alternately in either the gantries or the research area.
Different beam intensities can be requested, in a range spanning between 1 and 320 nA. The maximum particle rate depends on the beam energy, ranging from $3.8x10^6$ p/s at 70 MeV, up to $2.3x10^8$ p/s at a cyclotron extraction current of 1 nA. The extraction current can be increased up to 320 nA, and the corresponding maximum beam rates scale accordingly. The proton beam current is modulated by a 50% duty-cycle square wave, with a 20 ms period. The beam FWHM at the isocenter ranges from 6.9 mm at 70 MeV to 2.7 mm at 228 MeV.

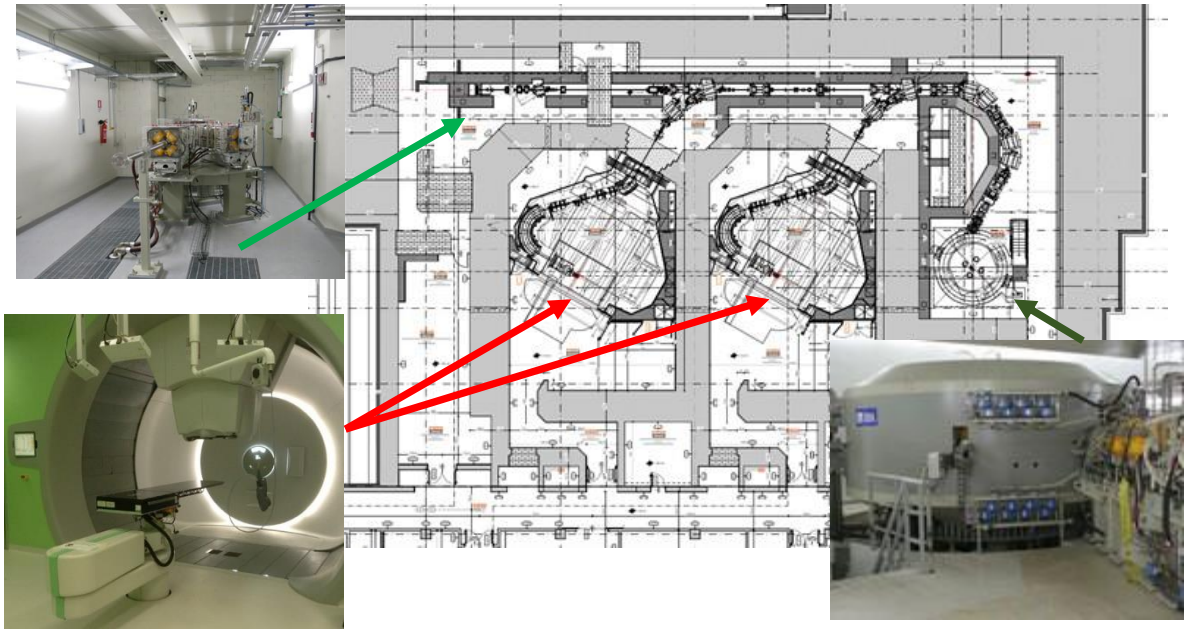

Figure 4.3 Trento proton therapy center

An extra feature provided by this cyclotron is the possibility to provide low beam intensities, with rates within a range of 10^1 up to 10^5 particles per second, required for a broad spectrum of experiments. To provide low particle fluxes the accelerator works in an operational regime that is different from the standard clinical one. In fact, such low intensities are obtained by exploiting the so-called accelerator "dark current", achieved by decreasing the high voltage of the accelerator source below the threshold used for standard operations.

4.3. Test setup and acquisition

Following the lab characterizations, the MoVe-IT UFSD strip sensors have been tested with the proton beams of CNAO and the Proton Therapy Center of Trento. In these tests other simple LGAD PiN diodes (pads) have also been studied.

The experimental setup, which scheme is depicted in Fig 4.4, was installed inside the treatment room at CNAO and the experimental room of TIFPA [40]. The sensors were mounted in custom passive test boards used to distribute the bias voltage and to provide the signal from two strips to the external electronics.
The HV was supplied by a CAEN DT1570 power supply [41], controlled by remote through an Ethernet connection and the GECO2020 control software [42].

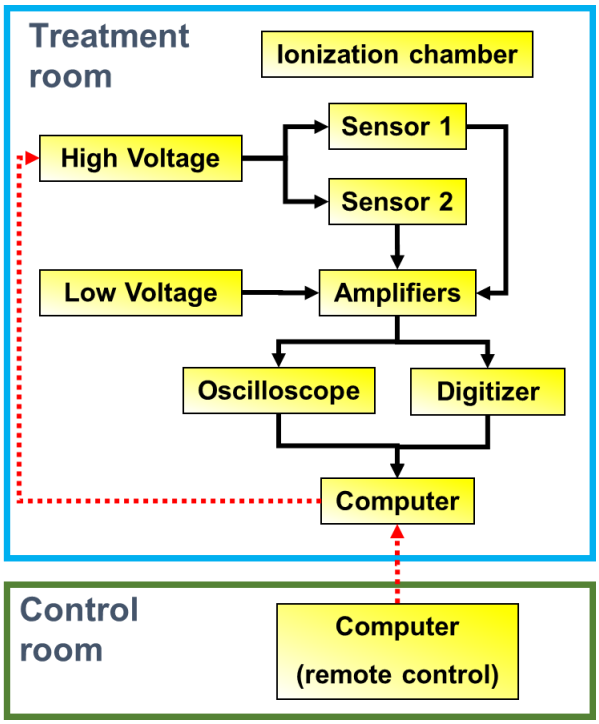

Figure 4.4 Scheme of the acquisition setup

The readout is based on external broadband amplifiers from CIVIDEC [30], with 40 dB gain and 2 GHz bandwidth, powered with a Low Voltage supply. The noise level of the CIVIDEC amplifier is 2.5 mV. The output signals from the amplifiers are sampled and collected by a fast digitizer and saved on a PC. Some preliminary acquisition has been done using an oscilloscope (LeCroy, Wave Runner 6 Zi, 0.4-4 GHz of bandwidth, 40 GS/s sampling rate) [43]. All the instruments are remotely controlled by a computer installed in an external control room.
A pinpoint ionization chamber from PTW was installed behind the sensors and aligned with the beam direction to provide an independent measurement of the beam rate. A picture of the acquisition setup installed in the CNAO control room is shown in Fig.4.5

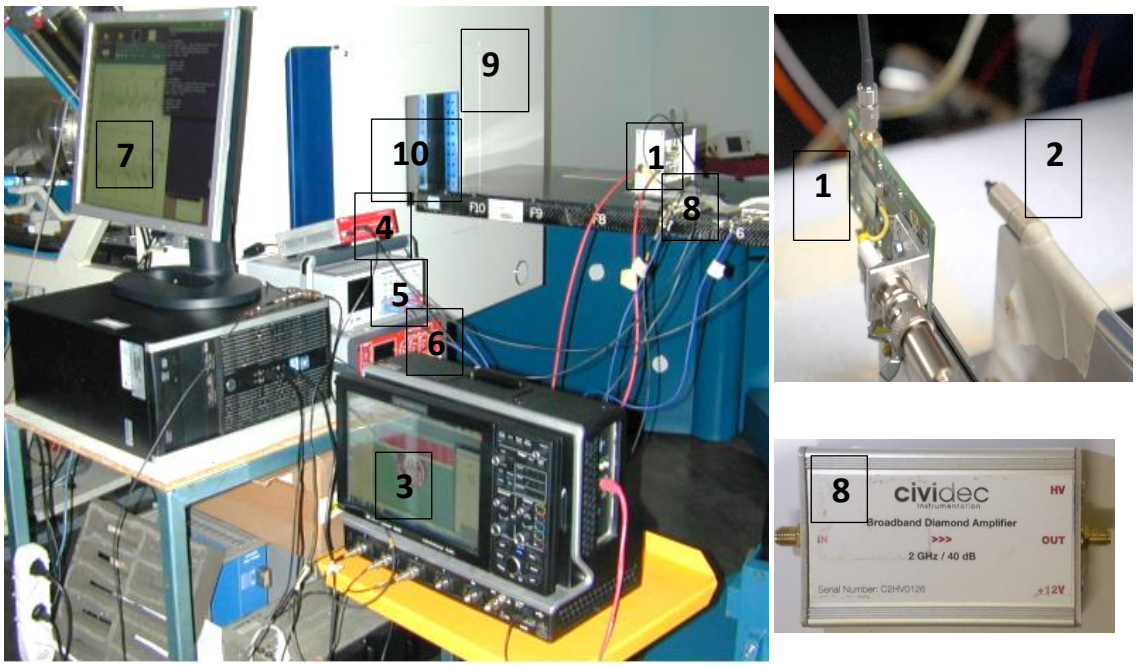

Figure 4.5 Beam test set up, with the strip/pad UFSD sensors (1) aligned with pinpoint ionization chamber (2). The other instruments are: oscilloscope (3), digitizer (4); low voltage power supply (5); HV power supply (6); acquisition PC (7); amplifier (8); monitoring chamber (9). The beam exit is indicated as 10.

4.3.1. Digitizer

The main instrument used to collect the signal is a 16+1 desktop digitizer (DT5742 CAEN, Italy, [44]), with 500 MHz bandwidth (Fig. 4.6). The digitizer samples the signals at 5 GS/, with one ADC count corresponding to 0.24 mV. For each trigger it stores 1024 samples corresponding to a waveform of 204.8 ns duration.

Figure 4.6 CAEN digitizer, with 16 channels input and two data transfer modalities

An optical link connects the digitizer with a PC through a CAEN PCI CONET A2818 Controller [45], which allows to transfer data at 80 MB/s which is 3 times faster than an alternative USB connection.

A custom modified version of the CAEN software Wavedump [46] was used to configure the working parameters, to control the acquisition and to provide an asynchronous software trigger as soon as the previous event was collected and saved on disk. The conversion time of the digitizer (110 μs) and the time needed to transmit and store the data (~500 μs) limit the acquisition rate to about 1 kHz.

At CNAO a spill-on logical signal from the accelerator control room was acquired with one digitizer channel and used to prevent trigger generation during the inter-spill period. To optimize the data throughput, the acquisition software was modified to buffer events in the PC memory during the in-spill data acquisition and save them on disk during the inter-spill period when no new events are expected.

At TIFPA the beam structure was different with no spill structure, and a continuous acquisition scheme was adopted. The analog signal following the cyclotron radio-frequency (RF) cycle was acquired with one of the digitizer input channels to study the beam structure and its synchronization with the RF repetition period.

4.3.2. PTW pinpoint ionization chamber

The setup included also a PTW Pinpoint ionization chamber (T31015) [47]. This chamber is ideal for dose measurements in small fields of photon and proton beams having a nominal sensitive volume of 0.03 cm^3 and 2.9 mm in diameter, measuring relative dose distributions with very high spatial resolution.
The charge was measured with the PTW Unidos electrometer [48] that applied the high voltage (100-400) V between the chamber electrodes and displays the measured values in various units i.e. dose and dose rate in Gy, R, Gy/min, R/min or Gy·m. Charge and current are measured in C and A.

4.4. Tests at CNAO

To understand the beam characteristics and the sensor behavior, several warmup runs were performed with 1.2x1.2 mm^2 LGAD pads produced at CNM, Barcelona [49] and circular LGAD pads with 1 mm diameter produced by the Hamamatsu company [50].

As a second step, selected UFSD strip sensor were positioned in the isocenter of the proton beam and the pinpoint ionization chamber was aligned just behind the connected strip to have a reference value of the total fluence for each run (Fig 4.7).

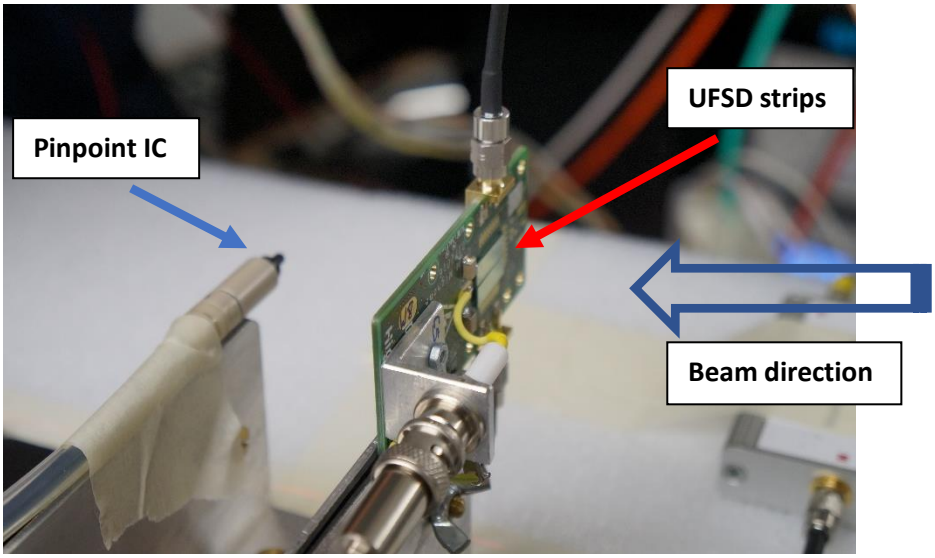

Figure 4.7 A pinpoint chamber and a strip sensor aligned along the beam direction

Preliminary measurements with pads and LGAD strips have been performed collecting data on the oscilloscope, and repeated for different bias voltages and energies. These runs are important to find the optimal working parameters, like the bias voltage to the sensor to have a sufficient SNR for all the proton energies, to adapt the digitizer dynamic range and avoid saturation.
Once the operational parameters have been fixed, sets of measurements have been performed with the digitizer and different beam fluxes to study the counting capabilities of the sensor

4.4.1. Signal shape and beam structure

The data collected at CNAO are saved in files, containing the ADC values for each digitizer sample and for each enabled channel. A separate file is saved for each trigger, containing a waveform of all the collected channels in a 204.8 ns window with the acquisition time saved in the header of each file, used later to calculate the acquisition duration.

The data analysis has been performed using the ROOT framework [51], where all the functions for data reading, processing, and the output are implemented.

An example of waveform collected at CNAO is shown in Figure 4.8.

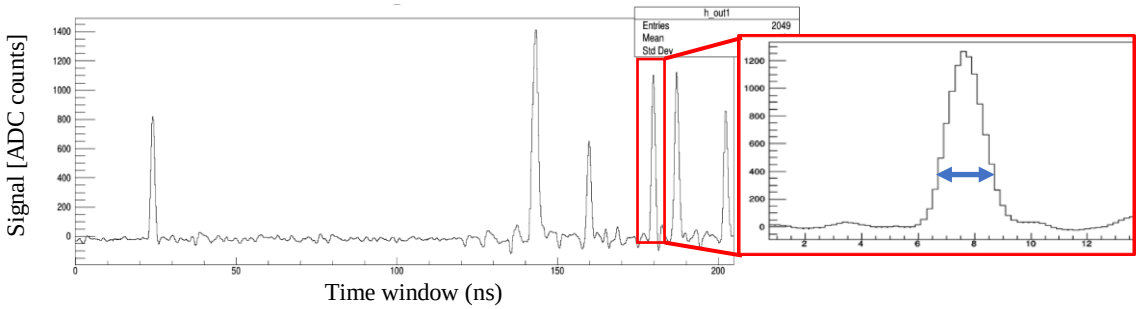

Figure 4.8 Left: an example of digitizer time window. The individual peaks correspond to signals from single protons; Right: a zoom of a single

This waveform shows the signals from one strip during the beam irradiation with 62 MeV protons at a flux of about 10^8 p/(cm^2·s). The waveform has been corrected for a constant offset estimated using data collected with no beam irradiation.
The peaks, corresponding to individual protons crossing the sensor strip, can be clearly distinguished and separated. An example of a single signal is shown in Figure 4.8(right); its duration, of about 2 ns, is compatible with the expected signal, taking into account the limited bandwidth of the digitizer.
A fast baseline restoring of the amplifier is observed, preventing a baseline shift that could affect the counting capabilities of the device.

The very fast response time of the LGAD sensors allowed to study the CNAO beam structure with extremely high details, at the nanosecond time scale. An example of time distributions of signal peaks identified when a LGAD pin was irradiated with the 227 MeV protons at CNAO is shown in Fig.4.9.

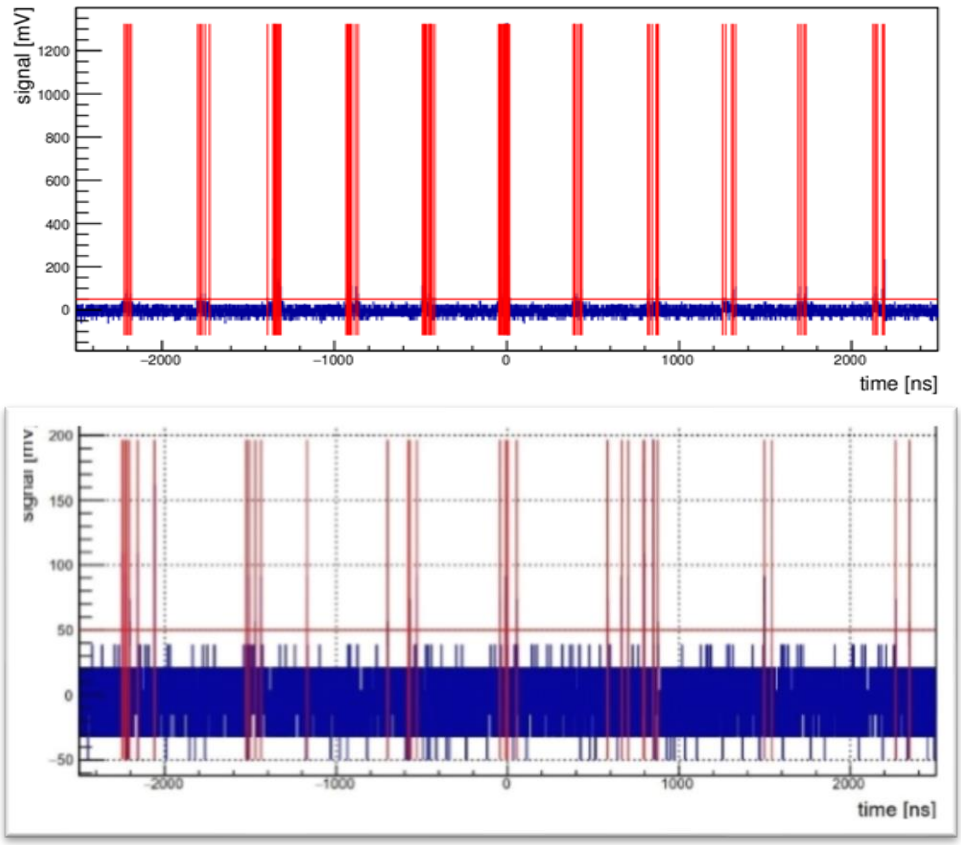

Figure 4.9 Beam structure of the CNAO proton beam at 227 MeV (top) and 62 MeV (bottom). The protons are packed in bunches synchronous with the extraction period of the accelerator. The instantaneous intensity reaches 10^{10}p/(cm^2·s).

This data show that the particles are extracted in short bunches with a period of about 220 ns and a frequency of about 2.3 MHz, compatible with the revolution time of the protons in the accelerator main ring. This beam bunched structure reflects the extraction mechanism of the accelerator, and is less evident reducing the proton energy at 62 MeV (Fig 4.9 bottom).

The mean proton flux at 227 MeV is about 10^9 p/(cm^2·s). The beam structure shown in Fig. 4.9 indicates at that highest CNAO energy the particles are concentrated in bunches which duration is about 10% of the bunch period. The corresponding instantaneous particle flux in each bunch is therefore an order of magnitude higher than the mean flux, about 10^{10} p/(cm^2·s) affecting the counting capabilities of the UFSD strip structures, as described in details in the following.

4.4.2. Choice of the threshold value.

In order to count the number of protons, a fixed threshold must be selected to discriminate real signals from the background noise. Once a fixed threshold is selected, each pulse is detected by checking a signal level crossing the threshold. In order to prevent double counts due to signal noise, in the data analysis a minimum number of digitizer samples is required before a second pulse can be detected.

To achieve the required accuracy of 1 % on the number of counts, the threshold must be high enough to limit the number of fake counts due to noise spikes to less than 1 % of the total number of counts; at the same time the detection efficiency must be greater than 99 % for the signals from protons of different energies expected in a therapeutic beam (from 62 MeV to 227 MeV at CNAO). It is to be underlined the statistical nature of the ionization events in the thin silicon sensor, giving large fluctuations of the signal levels even for particles at a fixed energy.

In order to study the noise and signal amplitude distributions, the number of pulses detected in the collected data sample was counted for different threshold levels (threshold scan). An example of the count rate distribution as a function of the applied threshold level is shown in Fig.4.11(left) for data collected from a LGAD diode at three different proton energies (62, 105 and 227 MeV). The high number of counts at low thresholds is due to the effect of the noise. By increasing the threshold value, a plateau in the count distribution is visible, corresponding to the region where the threshold is above the level and the signal peaks are correctly counted. At still higher threshold levels the count rates decrease again due to the loss of signals with an amplitude below the threshold.

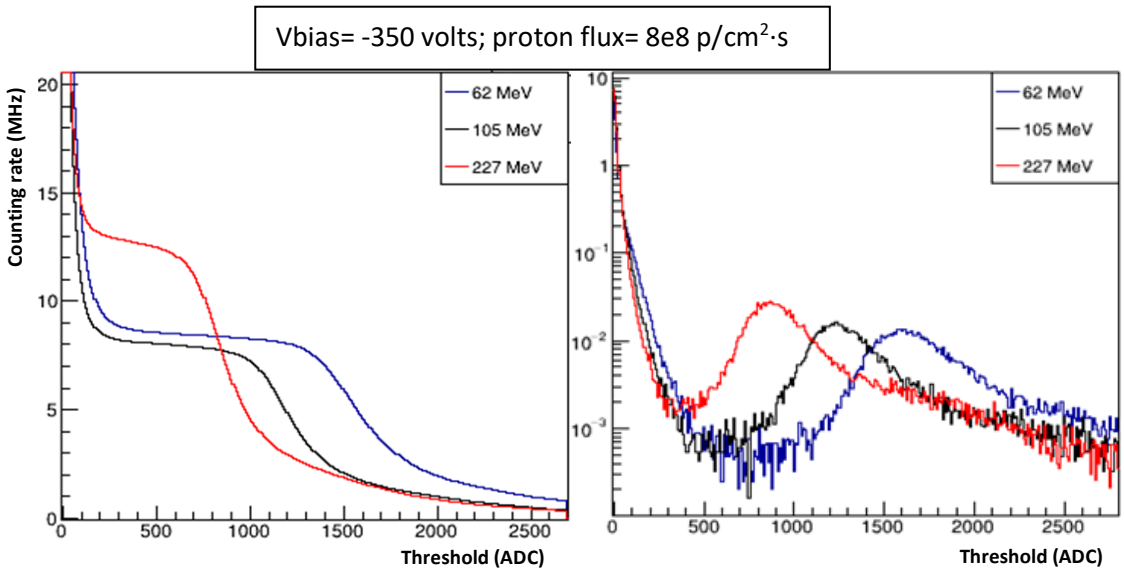

Figure 4.10 Left: threshold scan for a LGAD pad with 350 Vbias: count rates versus the threshold value are shown for three different proton energies; Right: amplitude distributions estimated from the threshold scans for the three energies

The count rate distributions of Fig.4.11(left) depends on the noise level and signal distributions, the last depending on the proton energy. It would be interesting to have a clear view of these distributions, in order to set an optimal threshold to separate the signals from the noise. The procedure to determine these distributions is here described.

Suppose f(x) being the probability density distribution of the signal amplitudes x. The number of counts detected for a fixed threshold x_{thr} is the number of signals with an amplitude greater than x_{thr}, corresponding to the following integral:

$$N(x > x_{thr}) = \int_{x_{thr}}^{\infty} f(x)dx = 1 - \int_{0}^{x_{thr}} f(x)dx \qquad \textbf{(4.1)}$$

From Eq. 4.1, the probability density of the signal (and noise) amplitude can be determined as:

$$f(x_{thr}) = -\frac{dN}{dx_{thr}}(x_{thr}) \qquad \textbf{(4.2)}$$

Therefore, the signal amplitude distribution can be estimated using the derivative of the measured rate distribution as a function of the applied threshold. The results are shown in Fig. 4.10(right).

The amplitude distributions show the expected Landau distribution, with a long tail and an increasing Most Probable Values (MPV) with the lowering of the proton energy. The noise appears as the fast decreasing curves at small

threshold values. The optimal threshold level is chosen in the region between noise and signal distributions: as an example, a value of 350 ADC counts (corresponding to 84 mV) was chosen for this sensor. It has to be remarked that the highest proton energy of 227 MeV corresponds to the minimum energy release in the LGAD sensors and to the worst signal-to-noise separation. It is clearly more difficult to have a proper and accurate discrimination of pulses for high energy particles.

The threshold scan analysis was performed to determine the optimal threshold value for each sensor and for each bias voltage in all the analysis shown in the following part of the thesis. For each data set the optimal threshold value was determined with the threshold scan as described above.

4.4.3 Gain measurement and dependence on the high voltage

The tests at CNAO have been performed with the long and short strip UFSD sensors described in the previous chapters aligned along the beam direction and irradiated with proton beams at different energies. The same threshold-scan offline procedure described before was been applied for each run to evaluate the amplitude distribution. An example is shown in Fig. 4.11 where the amplitude distributions extracted from data collected with the digitizer from one channel of the short strip sensors irradiated with 105 MeV protons are shown. The different curves correspond to different values of the bias voltage applied to the sensor.

The MPV values of the signal distributions move to higher values when the bias voltage is increased. This is a characteristic feature of LGAD detector, for which the internal charge amplification depends on the electric field in the region of the gain implant that increases with the bias voltage. Operating a LGAD detector at higher voltages allows to enhance the signal and to have a better separation of the signal from the noise, as evident from the distributions of Fig. 4.11

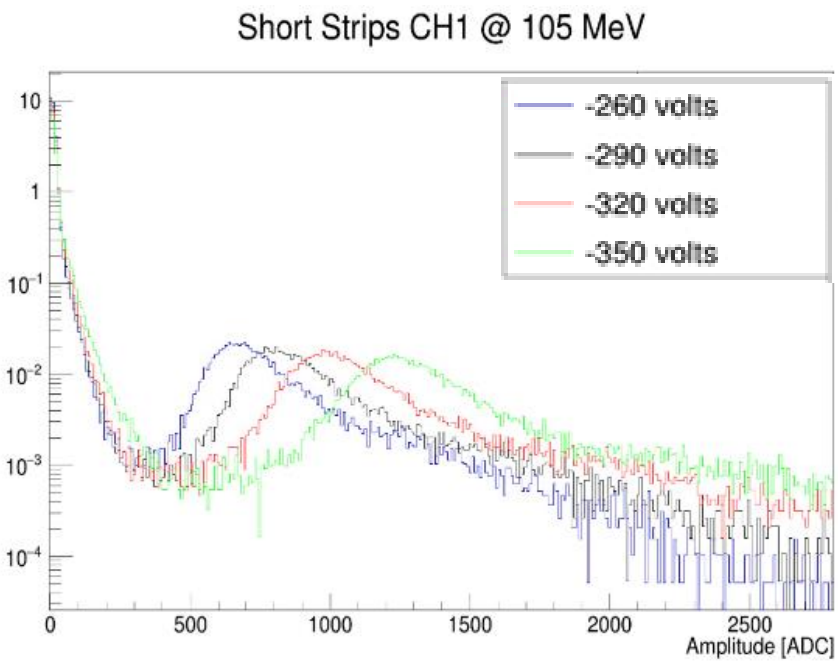

Figure 4.11 Amplitude distribution as a function of threshold for the three bias values

In order to estimate the gain factors of the UFSD structures with long and short strips, data have been collected also for the sensors produced without the implantation of the gain layer. The gain values of the UFSD strip sensors, defined as the ratio of the amplitude MPV values for sensors with and without gain, are reported in Fig.4.12 as a function of the bias voltage for two different proton energies

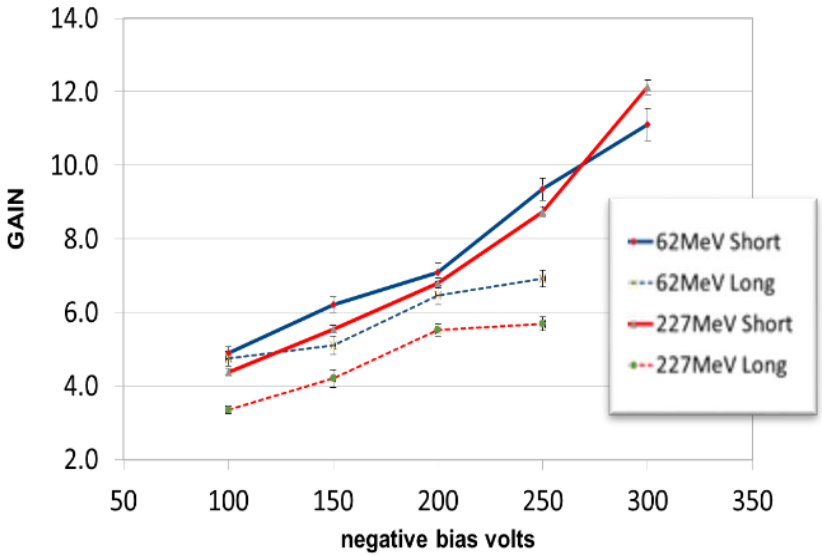

Figure 4.12 Gain values for long and short UFSD strips as a function of the applied reverse bias at two extreme CNAO energies

The gain factor increases with the bias voltage, as expected, reaching a value greater than 10 for the short strips at V_{bias}>270 V. The gain factors measured for the long strips are smaller. This is due to the different widths of the gain layer of the strips in the two UFSD structures, with a smaller faction of area where the gain reaches the full values in the long strip with respect to short strips. At the strip border the gain decreases from the full value to 1 moving from the gain region to the interstrip dead area. The measured gain value is a mean value depending on the gradient of this transition and the width of the region where a full gain is achieved.

After the threshold is defined, the single peaks can be discriminated and counted. Fig. 4.13 shows how the MPV from a Landau fit of the area distribution below each peak depends on the beam energy. The red curve in Figure 4.13 is the results of a fit with a 1/E function, showing that these measurements follow the expected Bethe-Block dependence on the energy.

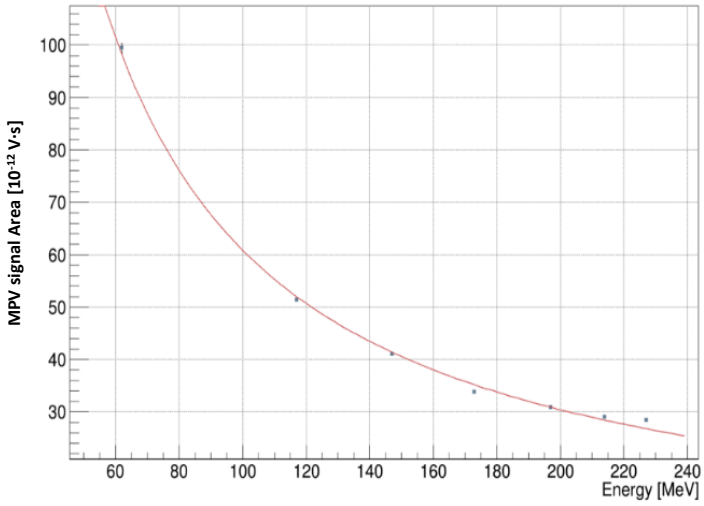

Figure 4.13 Fit of MPV at different energies follow Bethe-Bloch trend

4.4.4. Radiation resistance

In one of the first tests performed at CNAO at the end of 2016 a UFSD pad was irradiated with protons of different energies and an integrated fluence of 10^{12} protons/cm^2. The signal amplitude has been checked from data collected at the beginning and just before the end of the test, to evaluate the degradation in performance of the irradiated sensor. The results are shown in Fig. 4.14 where the distribution of the signal areas is shown before and after irradiation.

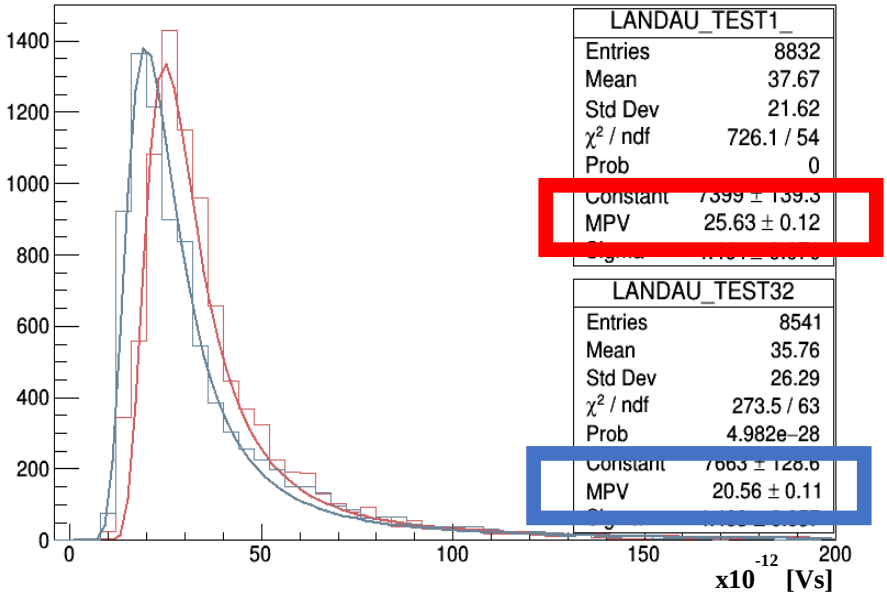

Figure 4.14 Shift of the MPV toward left after long irradiation

The curves overlapped with the distributions and the parameters shown in figure are the results of a fit with a Landau distribution. A clear decrease of the Most Probable Value (MPV) of the signal area of about 20% is observed, due to a well-known effect of gain reduction with radiation for a UFSD silicon detector. This gain reduction can be compensated with an increase of the voltage bias, but the observed gain degradation occurs at a very low fluences for actual clinical applications. For example, a beam monitor detector used in in a clinical environment is expected to be exposed to about 10^{15} p/cm^2.

Since 2016 extensive studies have been performed by our colleagues in Torino to understand and improve the radiation resistance of UFSD sensors. Some of the results have been already described in Section 3.7 and it is already demonstrated the possibility to operate a UFSD sensor after the irradiation of more than 10^{15} n_{eq}/cm^2 with acceptable time resolutions [52]. Other studies to push further the operation limits of UFSD detectors at very high radiation doses are ongoing, in particular for applications in high energy experiments at LHC.

4.4.5 Test of counting capability

In order to test the counting capabilities of the strip sensors, several runs have been collected at CNAO for different proton energies and, for each energy, at different beam fluxes. At CNAO it was possible to ask for particle fluxes

corresponding to the clinical fluxes and for lower beam intensities provided by a "degrader" mechanism in the extraction procedure. The degrader can be set at different levels (100%, 50%, 20%) roughly corresponding to scale factors applied to the maximum beam particle flux.

Many runs have been collected with different UFSD strip sensors during a test performed at CNAO in May 2018. The data described in the following comes from long strip sensors positioned at the isocenter and irradiated with protons at three energies: 62, 110 and 228 MeV. For each energy three runs have been collected with three degrader settings, to check how the counting capability of the strips changes with the beam intensity. A fixed number of particles were irradiated for each run and measured online by the monitor chambers installed in the treatment room. The strips were polarized with 250 V. For each run the integral charge produced in the Pinpoint ionization chamber positioned behind the strips was registered to provide an independent measurement of the particle rates, as described later.

During the test, the signals from two strips were collected by the digitizer and saved on disk. The offline analysis started with the study of the threshold scans and the choice of a proper threshold level. The number of counts and the rate of signals above threshold has been measured for each run and compared with the charge rate measured by the pinpoint chamber. The conversion form number of counts or total charge to the corresponding particle rates is performed using the time registered in the file headers, which allows a precise determination of the total beam time for each run.

The results are shown in Fig. 4.15, where the strip count rate is shown as a function of the charge rate measured with the pinpoint chamber. In this figure each plot corresponds to one of the energies used in the test, and for each energy the three points correspond to different degrader settings.

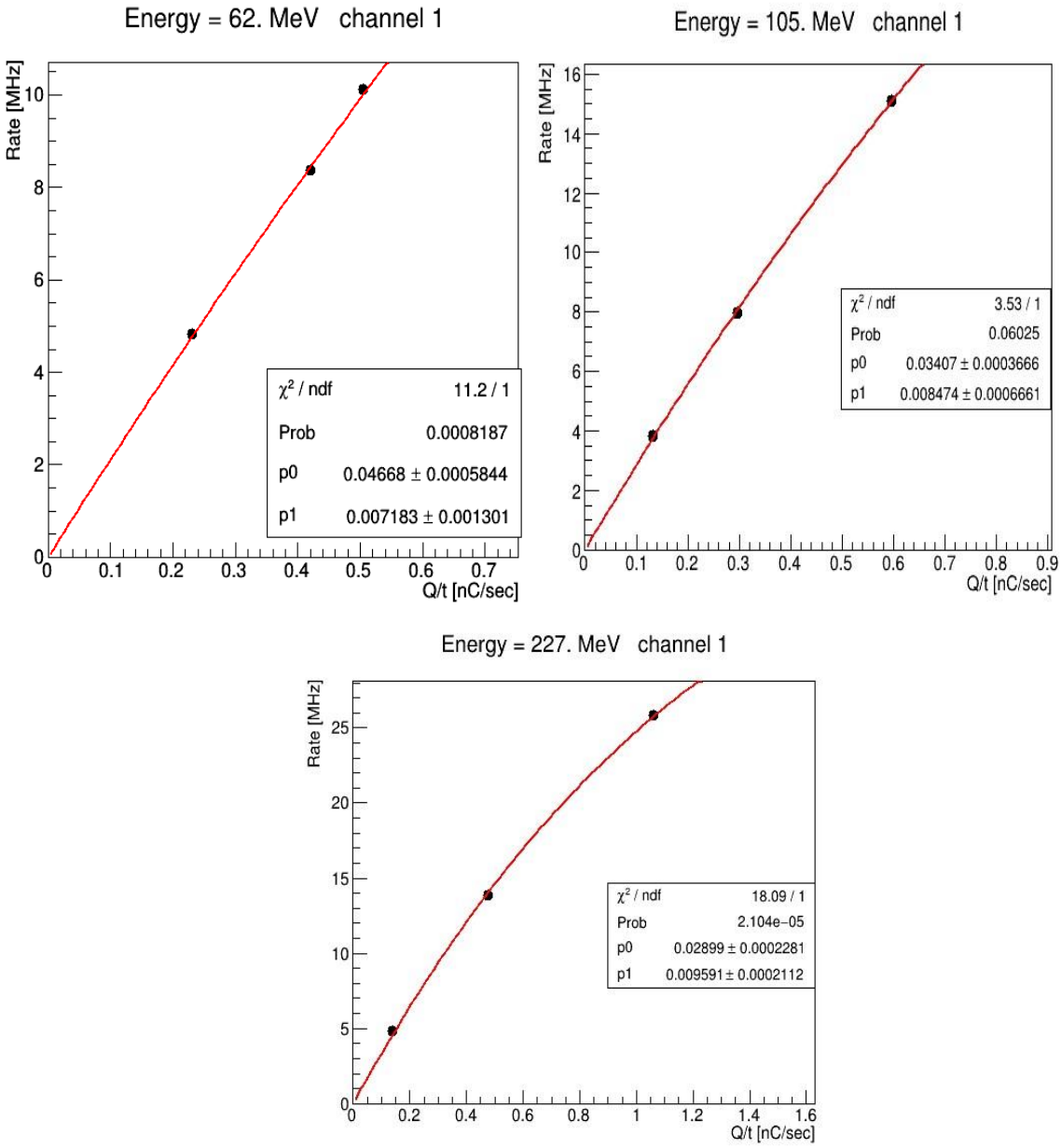

Figure 4.15 Measured particle rate by a UFSD strips as a function of collected charge rate collected by the pinpoint IC at CNAO

At the highest energy a clear saturation curve is visible. The non-linearity between the particle rate measured with the UFSD strip and the charge rate measured with the ionization chamber is caused by counting inefficiencies due to the overlapping of signals close in time (pile-up): this pile-up effect becomes important at high fluxes. The fact that the effect is more evident at high energy is due to two reasons: at high energy the beam at CNAO shows a bunch structure, and the instantaneous particle flux inside each bunch is high. This bunch structure is less evident at lower energies, and therefore the pile-up effects are less pronounced when the beam energy is reduced. A second reason of the different saturation behavior at low and high proton

energies is due to the beam transversal shape. At low energy the beam FWHM at the isocenter is larger than at higher energies due to an enhanced scattering of low energy protons in air between the beam line exit window and the isocenter. The corresponding flux is therefore lower.

In order to have an estimation of the input particle rate hitting the strip regardless the pile-up effects, it is assumed that the charge measured by the pinpoint chamber is linearly correlated to the number of input particles and that no saturation effect is present in the charge collection. The inefficiency due to pile-up effects are parameterized with the following equation:

$$f_{meas} = f_{true} e^{-\tau f_{true}} \quad \textbf{(4.3)}$$

where f_{true} is the particle input rate in one strip, f_{meas} the count rate measured from the strip, and τ the system dead-time. In this study, Eq. 4.3 is considered as a possible simple parametrization of counting inefficiencies. In the next chapter it will be shown that Eq.4.3 is also the description of inefficiencies in a paralyzable pulse counting system with a fixed deadtime τ, when the particle flux is random and the number of input particles in a fixed time period follows the Poisson statistics. In a paralyzable counting system, the deadtime τ is the time period when the system cannot count other pulses arriving after a first one, and these pulses extend the deadtime of the system. It is plausible that an LGAD sensors behaves like a paralyzable system due to the way the signals from charge migration is formed in the sensor.
Assuming the pinpoint IC behaves linearly with respect to the particle flux, the input rate f_{true} is proportional to the charge rate Q/Δt measured by the pinpoint chamber:

$$f_{true} = \frac{Q}{C \cdot \Delta t} \quad \textbf{(4.4)}$$

where C is an unknown normalization factor, depending on the strip and pinpoint geometries, on the beam shape and energy. This factor C is the equivalent charge produced in the pinpoint chamber for one proton hitting the strip. Inserting Eq. 4.3 into Eq. 4.4, the following parameterization of inefficiency effects arises:

$$f_{meas} = \frac{Q}{C \cdot \Delta t} \cdot exp\left(-\tau \cdot \frac{Q}{C \cdot \Delta t}\right) \quad \textbf{(4.5)}$$

where f_{meas} and Q/Δ(t) are the quantities shown in the axes of Figure.4.16 (i.e. the count rate from the UFSD strip and the charge rate from the ionization chamber). Two unknown parameters appear in Eq. 4.5: the

deadtime τ and the normalization constant C. These parameters depend on the beam energy. In particular the factor C depends on the beam shape, on the charge produced by one proton in the pinpoint chamber and on the relative position of the pinpoint and the strip. Even if the two unknown parameters could depend on the beam energy, we don't expect that they change for runs collected with a fix energy and different degrader settings. Therefore, they are extracted by a fit with Eq. 4.5 of the points shown in Fig 4.15 for each value of the proton energy. The red lines and the parameters in Fig. 4.15 correspond to the fit results. The value of the two parameters τ and C extracted by these fits are also listed in the following table:

Energy (MeV)	τ (ns)	C (fC)
62	9.6±1.4	0.0457±0.0005
105	8.47±0.6	0.0340±0.0003
227	9.59±0.2	0.0289±0.0002

Table 4.1 τ and C parameters extracted by a fit with Eq.4.5 at three CNAO energies.

The factor C decreases with the increase of the beam energy, as expected for the different ionization of the protons in the IC gas. The τ factor estimated from the fit is greater than the deadtime expected from the signal duration (about 2 ns as shown in Fig. 4.8). The reason of this discrepancy originates from the highly non-uniform time structure of the CNAO beam. As described in the following chapter, the effective τ derived by Eq. 4.5 when f_{meas} is the mean count rate includes the effect of the beam bunch structure. The fact that the effective dead time increases with the beam energy depends on the beam structure becoming more and more packed in bunches, with higher instantaneous frequencies.

Once the normalization factor is determined for each energy, the charge rate measured with the pinpoint chamber can be converted in mean input particle rate hitting the strip, using Eq. 4.4. Fig. 4.16 shows the dependence of the measured strip count rate as a function of the input rate estimated from Eq. 4.4. All the nine points measured at different energies are present in this plot, because this saturation curve does not depend on the beam energy. In Fig. 4.16 an additional horizontal axis has been added, where the estimated input rate is converted in a local particle flux on the strip expressed in GHz/(cm^2·s), considering a strip area of 2 mm^2. The effect of inefficiencies due to pile-up effect is clearly visible at high particle fluxes.

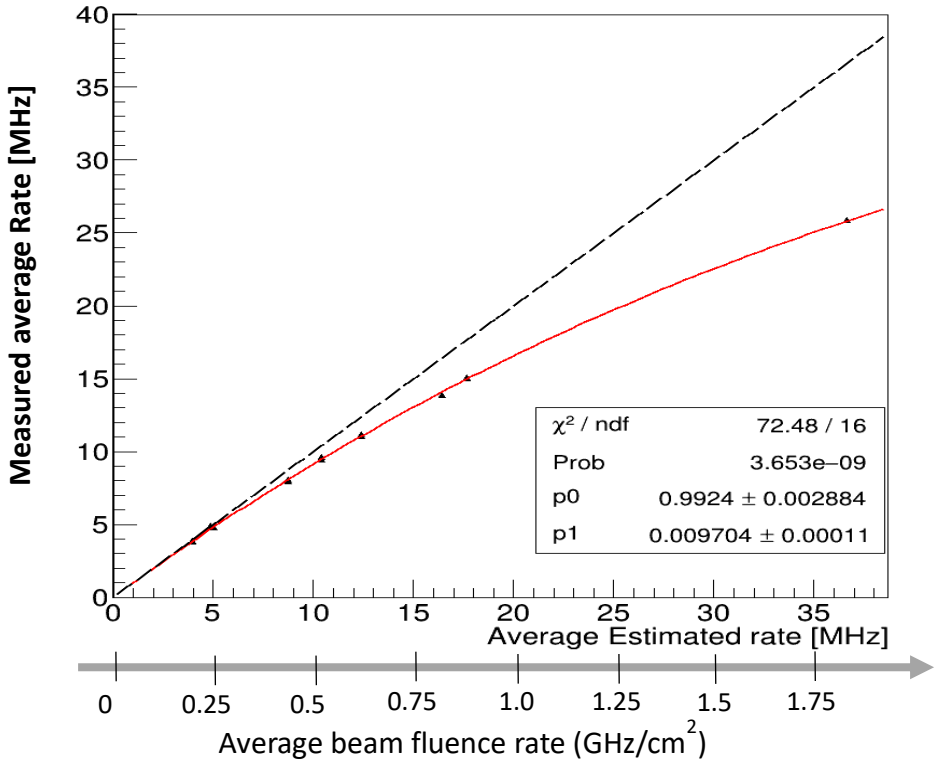

Figure 4.16 Measured rate vs. average estimated input rate for 3 acquired energies for data collected at CNAO

The input count rates in the UFSD strip for this test range from 4 MHz to 40 MHz, corresponding to local flux between 200 MHz/cm^2 to 2000 MHz/cm^2. It has to be remarked that the goal of MoVe-IT is to measure the particle flux up to 100 MHz/cm^2 with an error below 1%: in this region of flux values the inefficiency curve extracted from the data is very close to the ideal linearity curve shown with the black dashed line in the figure. However, the data collected at CNAO don't cover the region of such a low particle flux and don't allow to investigate with accuracy the counting errors at low particle rates. In addition, only three different beam intensity can be selected at CNAO for each energy, and the number of points available for the fits are not sufficient for a precise determination of the unknown parameters needed for a good estimation of the input rates. The following section describe the results obtained with a similar analysis with data collected al the Proton Therapy Center of Trento, where particles can be delivered with lower fluxes than at CNAO and a wider range of beam intensities.

4.5. Tests at the Proton Therapy Center of Trento

The tests performed at CNAO and described in the previous section have been repeated at beginning and mid 2019 at the experimental room of the

Proton Therapy Center (PTC) of Trento. The same instrumentation and acquisition setup were used, as already described. More accurate planning and control of the acquisition times were adopted to assure the count statistics was compatible with the expected errors.
The main differences with respect to the test at CNAO consist in the beam structure and the different range of beam intensities available at the PTC of Trento, as described in the following.

4.5.1 Beam structure at the PTC of Trento.

As already observed at CNAO, it is very important to understand and consider how the beam protons are distributed in time, because the counting inefficiencies depend on the instantaneous rate.

The first measurements performed at Trento were therefore dedicated to employ the fast response time and the optimal sensitivity of the UFSD detectors to understand the beam structure provided by the cyclotron.

A first beam structure observed at the PTC of Trento is shown in Fig. 4.17. In this figure the number of protons measured with a UFSD strip in each digitizer snapshot of 204.8 ns is reported as a function of the acquisition time. The periodic structure shown in the figure correspond to a beam irradiation occurring periodically with a period of 20 ms and a duty cycle of 50 %.

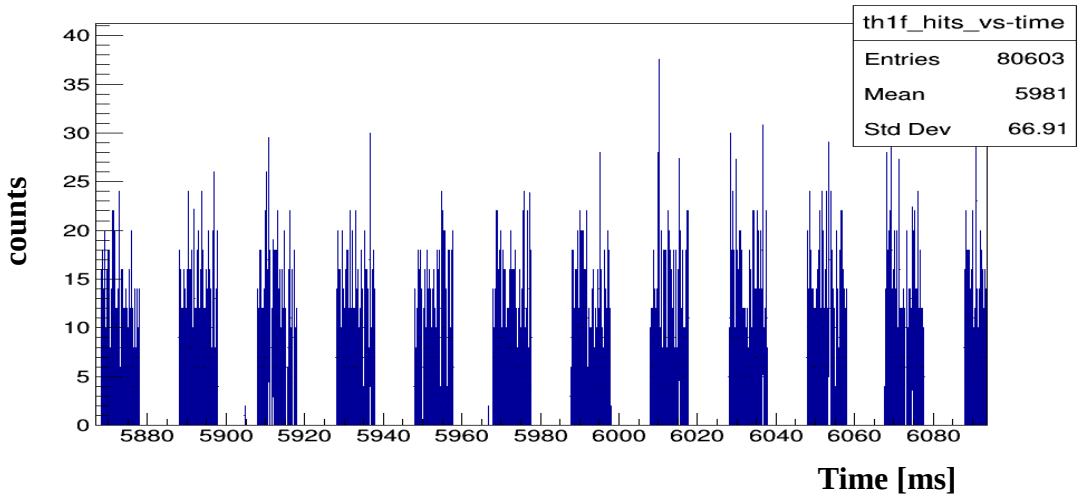

Figure 4.17 Number of protons measured for each trigger as a function of the acquisition time for data collected at Trento.

A second beam structure is observed at a finer time scale. An attenuated signal from the cyclotron radiofrequency was available in the control room and connected to one channel of the oscilloscope, while the other

oscilloscope channels was dedicated to collect the signals from one LGAD pad after the amplifier. A snapshot of the oscilloscope in shown in Fig. 4.18.

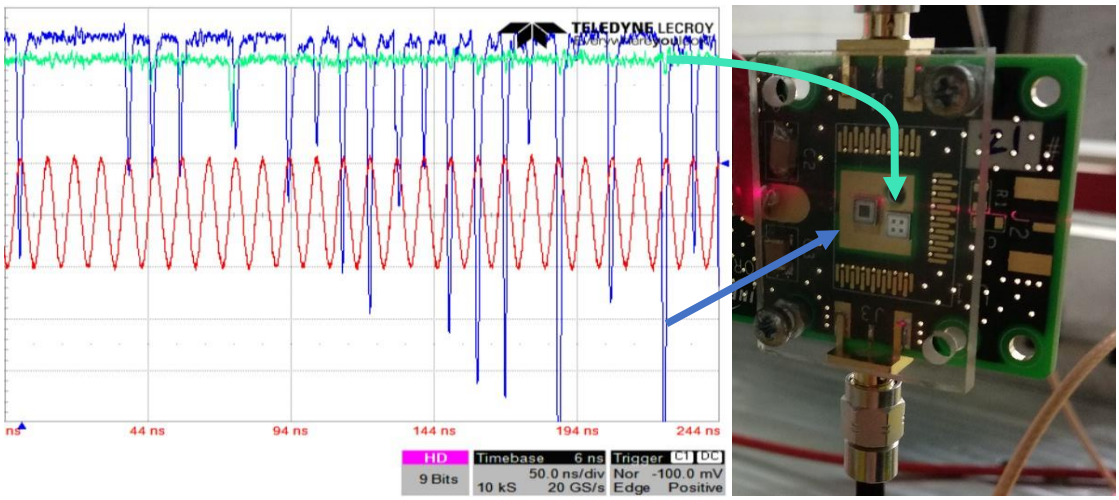

Figure 4.18 Left: screenshot from the oscilloscope with the signal from one LGAD pad (blue) overlapped with the RF periodic signal (red) for a beam energy of 148 MeV and a current of 1 nA. Right: board hosting two LGAD pads.

In Fig.4.20 the red curve is the signal from the accelerator RF with a period of 9.4 ns (frequency 106 MHz), while the blue curve is the signal from one UFSD pad of 4mm^2 area during the beam irradiation. It is evident from the picture that the proton extraction is synchronous with the cyclotron revolution or RF, and the protons are always provided in a short time interval with respect to the RF phase. The amplitude distribution of the signals of Fig. 4.18 does not depend only on the fluctuation in the charge produced in the sensor, but mainly on different number of protons irradiated at the same time in synchronous with the radiofrequency. In such a situation, the signals of multiple protons erogated in the same cyclotron cycle and hitting the same UFSD channel are completely overlapped and cannot be separated. However, it has to be underlined that the oscilloscope snapshot of Fig.4.18 has been collected at a high particle rate. The main goal of the tests at the PTC of Trento was to evaluate the counting capabilities of the UFSD sensors at a low fluence rates of 10^8p/(cm^2·s) foreseen as a MoVe-IT goal, not achievable at CNAO. This fluence rate corresponds to a particle rate in one UFSD strip of about 2 MHz, and at this rate the probability to have 2 proton signals overlapped in the same RF cycle is negligible.

4.5.2 Data analysis and counting inefficiencies

The test performed in February 2019 were used to study the beam structure, as described before, to find the operational bias voltage, to check the currents

from the sensor during the irradiation and to ensure the sensor stability with time. In July 2019 other measurements were done with UFSD strip sensors, by collecting data at different beam energies and beam currents. Data from two strips connected to CIVIDEC broadband amplifiers were collected with a digitizer. A PTW pinpoint chamber was positioned behind the strips and both the strips and the chamber were aligned along the beam direction using the laser pointing system available in the experimental room.

One problem appearing at TIFPA was the increase of the baseline noise in the waveforms collected with the digitizer and the difficulty to properly count the number of signals at high rates and at high proton energies. One example of signals collected with protons of 228 MeV and a beam current of 1 nA (corresponding to a count rate in the strip of 4.5 MHz and a local flux of about 200 MHz·cm^{-2}·s^{-1}) is shown in Fig.4.19(top): the proton signals can be easily discriminated by setting a threshold value such that the noise contribution to the pulse count is negligible. In Fig.4.19(bottom) the beam current was increased to 10 nA (proton rate in one strip 45 MHz, local flux of about 2x10^{9} p·cm^{-2}·s^{-1}): at this current the noise level was too high to allow a good separation of fake counts from real signals. From more detailed studies not reported here, it emerged that the negative pulses not associated with strip signals are due to particles crossing other strips of the sensors.

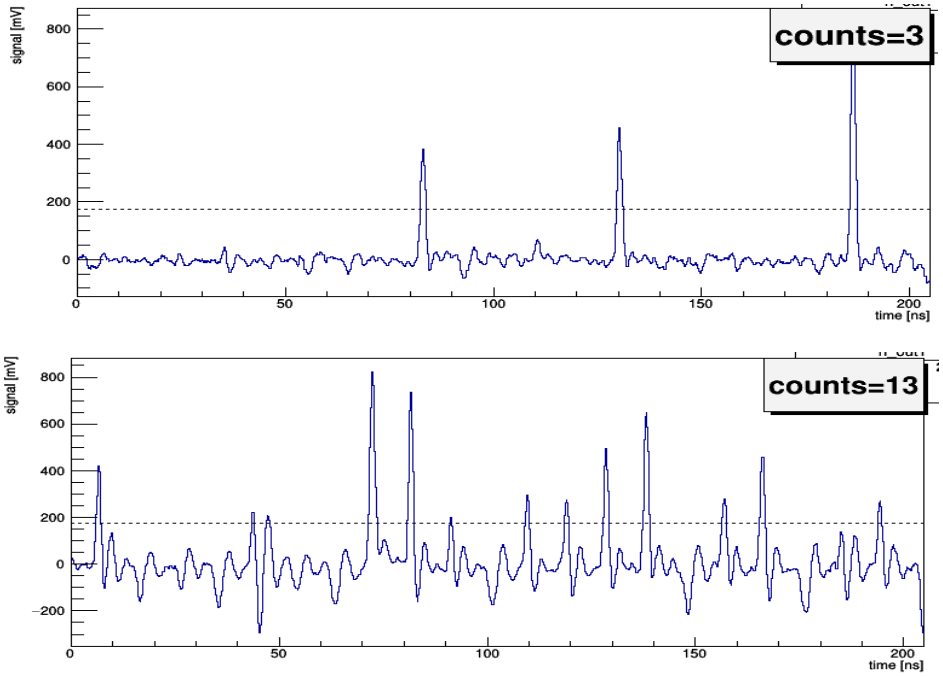

Figure 4.19 Digitizer waveform collected at beam energy of 228 MeV, and a beam current of 1 nA(top) and 10 nA(bottom)

The amplitude distribution extracted from the threshold scan procedure described in Sect.4.4.2 is shown in Fig. 4.20 for 228 MeV protons and different beam currents. At 3 nA a separation of the signals from the noise is still visible, allowing to set a proper threshold to discriminate proton signals. At higher currents two effects are contributing to the degradation of the counting capabilities of the sensor: the MPV of the signal distribution moves to lower values due to a baseline shift due to the negative pulses shown in Fig.4.19 and the noise increases. At 7.5 nA of current is it impossible to separate signal from noise looking at the amplitude distribution of Fig.4.20.

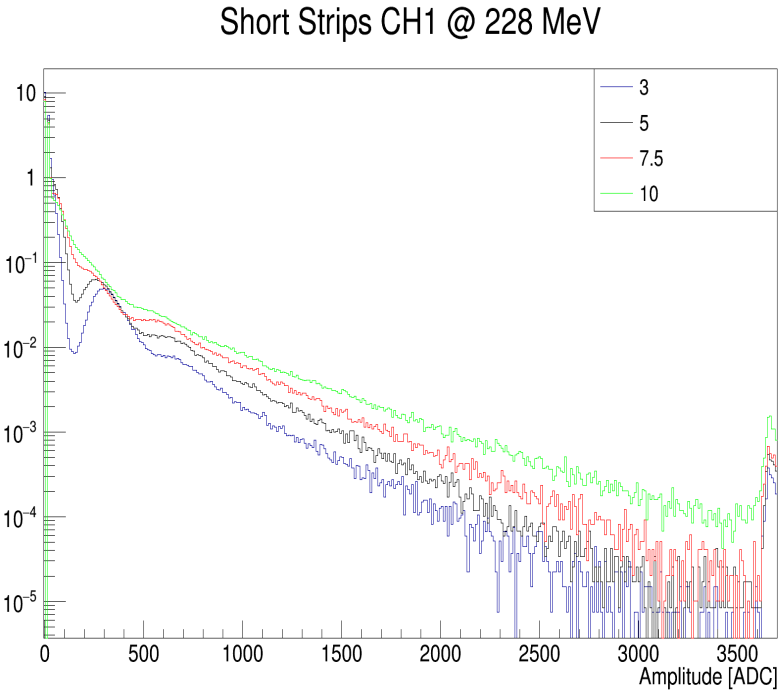

Figure 4.20 Amplitude distribution from a threshold scan for protons at 228 MeV and different beam currents.

The limitation of the strip sensors to provide reliable data at high beam fluxes was considered in the following tests by setting the beam current at levels corresponding to fluxes below 10 MHz·cm^{-2}·s^{-1} at 228 MeV, requiring cyclotron operation in "dark current" mode (Sect.4.2). It has to be mentioned that a better separation of noise from signal is achieved at lower proton energies due to the higher ionization in silicon and higher signal levels.

Runs with the following beam energies and currents have been collected:

Energy (MeV)	Current (nA)
70	50-100-150-225-300
125	5-8-15-25-40
179	3-4-6-8-10
228	Dark current mode-1-2-3-4

Table 4.2 Beam parameters required for the tests of the MoVe-IT strips at TIFPA

The beam intensities were chosen to investigate the counting capabilities of the UFSD strip sensors at low beam fluxes not available at CNAO, around the goal flux of MoVe-IT ($1 \cdot 10^8$ $cm^{-2} \cdot s^{-1}$ corresponding to 2 MHz count rate for a single strip).

The same offline analysis already described for the tests performed at CNAO was applied to estimate a common threshold level independent of the energy, to count the number of proton signals above threshold and the corresponding counting rates for the two strips and for each run. The only difference with respect to the measurements at CNAO was in the value reported by the electrometer used for the readout of the PTW chamber: at CNAO the electrometer reported the collected charge in nC, while at the PTC of Trento the results from the Unidos were reported in mGy. The same fits described in section 4.4.4 have been used to be estimated the particle input rate from the dose rate measured with the pinpoint at Trento: the only difference is that the C parameter in Eq. 4.5 for the data collected at Trento should be interpreted as the effective dose produced in the PTW chamber by each proton hitting the strips, instead of an effective charge.

The following figure shows the signal rate measured in one UFSD strip as a function of the dose rate measured with the pinpoint chamber, where each plot corresponds to one of the four energies used in the test and for each energy the black point are the measurements done at different beam currents. The red curve and the extracted parameters of fits are also reported in table 4.3.

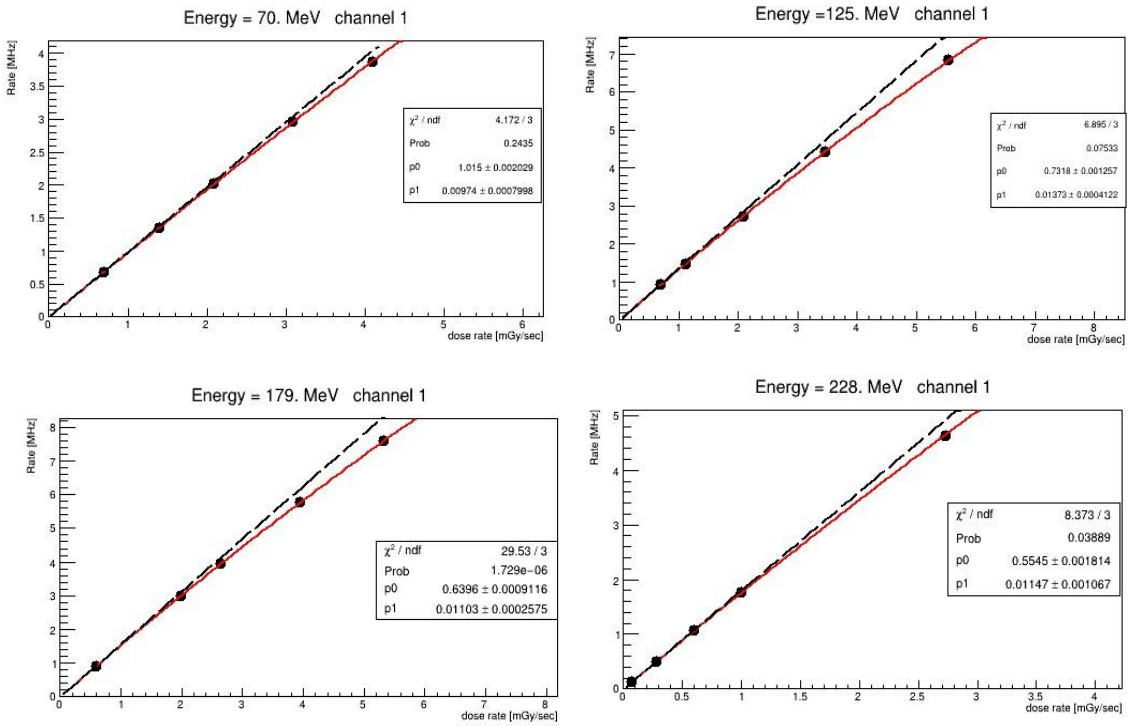

Figure 4.21 Particle rates by one UFSD strip as a function of the dose rate by the pinpoint IC for different proton energies at Trento Proton Therapy Center.

Eq.4.4 is therefore applied to estimate the input particle rate for each strip. The particle rate measured in one strip is reported in Figure 4.22 as a function of the input rate estimated with the method described above. The points shown here come from all energies and beam intensities used in the test, and the dashed line corresponds to the ideal case
of no counting inefficiency.

Energy (MeV)	τ (ns)	C (nGy)
70	9.7±0.8	1.0213±0.002
125	13.7±0.1	0.7358±0.0008
179	11.03±0.2	0.6418±0.0007
228	11.4±0.1	0.556±0.001

Table 4.3 Parameters from the fit with Eq. 4.5 of the particle rates measured with UFSD strips vs the dose rate measured with the pinpoint IC

To best appreciate the accuracy reached by this analysis, the same results are show in terms of the ratio $f_{meas}/f_{estimated}$, and reported in Fig.4.23 as a function of the estimated input frequency f_{input} separately for each beam energy.

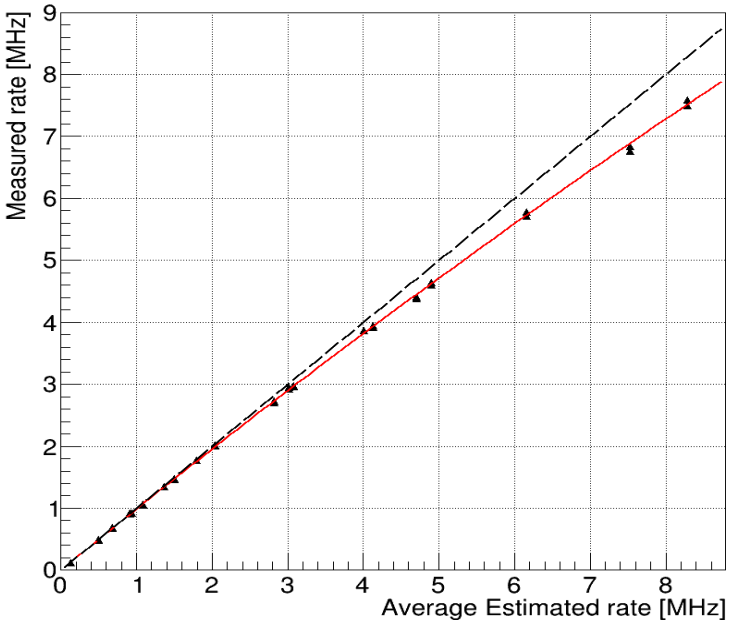

Figure 4.22 Measured rate vs. average estimated input rate for all the runs collected at the PTC of Trento with one UFSD strip

It has to be remarked again that the goal for the counting prototype developed for the MoVe-IT project is to count with a 1÷2 % error at fluxes up to 10^8 p/(cm^2·s), corresponding to a particle rate on one strip of 2 MHz. The results of these measurements demonstrate that this goal is achievable with the sensors developed for this application.
However, novel algorithms have been developed to mitigate the inefficiency effects and push the maximum measurable flux to higher values. These algorithms and their performance when applied to the set of data collected at CNAO and TIFPA are described in the following chapter.

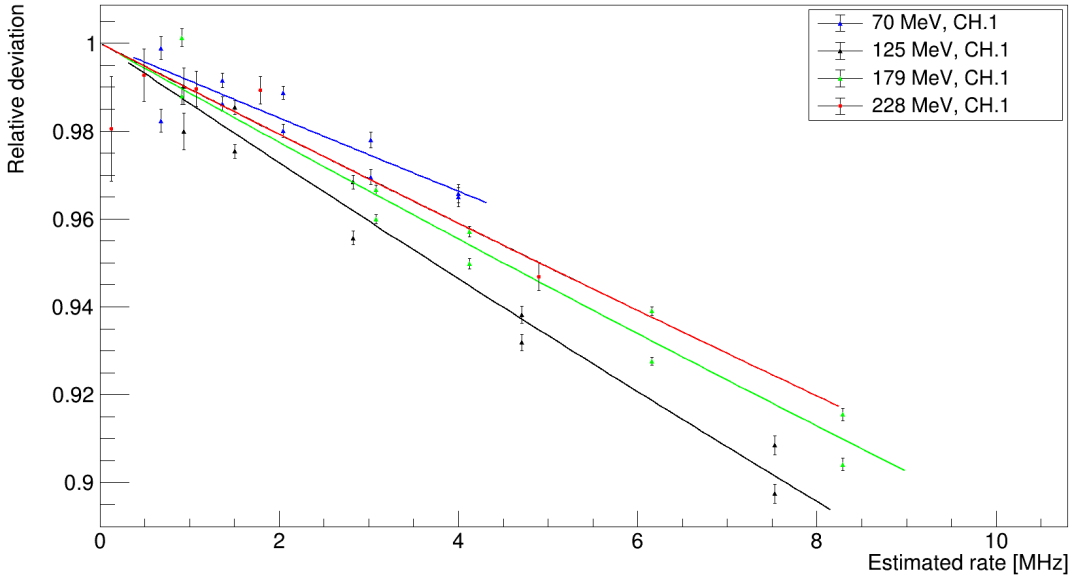

Figure 4 23 Relative efficiency f_{meas}/f_{input} as a function of the average estimated input rate for data collected at Trento.

4.5.3 Poisson distribution of the beam particles

An independent estimation of the mean particle input rate has been obtained by studying the distribution of the time difference between two consecutive proton signals in one strip. Under the assumption of a Poisson distribution for the particle flow, the probability density function to observe a second particle after a time Δt from the previous one is given by:

$$\frac{dP}{dt}(\Delta t) = e^{-f \cdot \Delta t} \qquad \textbf{(4.6)}$$

where f is the particle rate.

The distribution of the time difference between two consecutive counts for 228 MeV protons is shown in Fig.4.24.

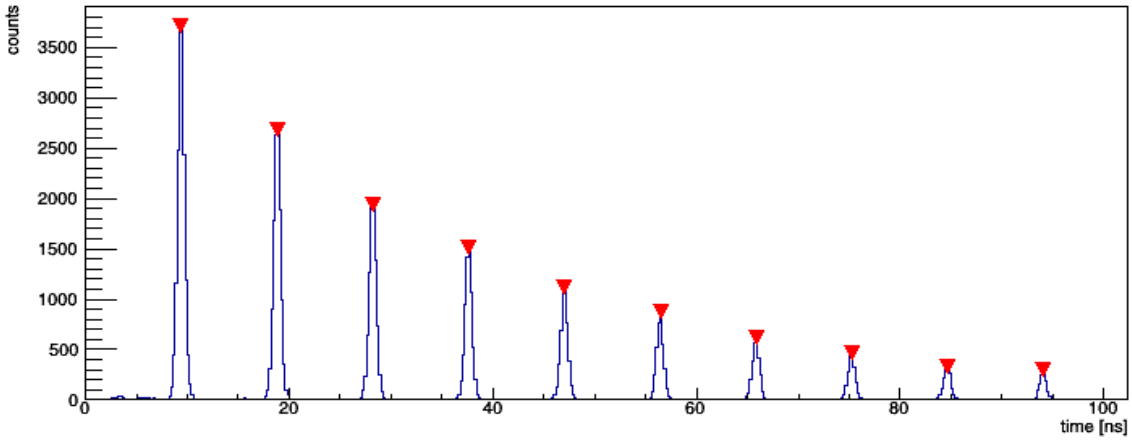

Figure 4.24 Time difference between two consecutive counts in one strip for 228 MeV protons

The Δt distribution has several peaks separated by 9.4 ns because of the beam structure of the IBA cyclotron already discussed in the previous sections. The number of particles contributing to each peak has been measured and reported in Fig. 4.25, where the result of an exponential fit was superimposed.

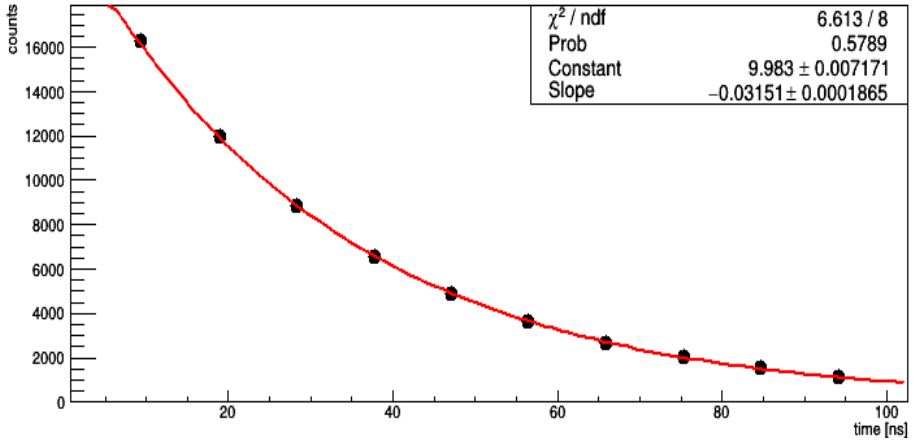

Figure 4.25 Number of counts vs the time difference with respect to the previous count with the result of an exponential fit

The fact that the distribution in the time difference between two peaks is well described by an exponential function demonstrates that the beam protons in the PTC of Trento are randomly distributed in time with a Poisson distribution within each 10 ms bunch.

The frequencies are estimated with the exponential fit described above for each run and compared with the mean input rates estimated as described in the previous section using the measurements of the pinpoint chambers. The two independent estimations of the input particle rates are compared in Fig 4.26 where the input rate from the exponential fit is shown as a function of the input rate estimated with the data from PTW chamber. The points include all the energies and beam currents used in the test.

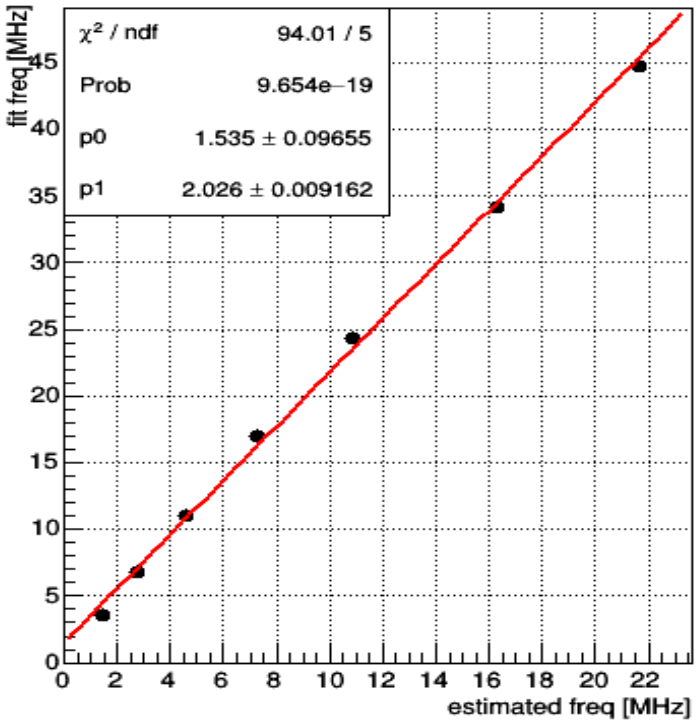

Figure 4.26 Particle rate in one strip extracted from the time difference distribution vs the input particle rate estimated from IC

Even if not perfect, a good linearity between the two estimations of the input beam rate is observed. The slope of the linear interpolation is compatible with a value 2: this is expected, because the particle rate estimated from the pinpoint chamber is a mean value averaged over all the acquisition time, while the frequency estimated from the time difference distribution is the instantaneous frequency inside a 10 ms spill. The first value is a factor 2 lower due to the spill structure of the beam shown in Fig.4.17, with a duty cycle of 50%. The good agreement between the two input rates is a proof that the procedure used to evaluate the counting inefficiency is correct.

Chapter 5

Correction of counting inefficiencies

5.1. Introduction

The results shown in the previous chapter indicates that the developed counting system based on UFSD sensors segmented in strips is able to measure the number of beam particles up to a maximum mean fluence rate of about 10^8 p/(cm^2·s) with an error of about 1%, according to the design goal. Above this value of the fluence rate, inefficiency effects due to the superposition of two signals close in time deteriorates the counting capabilities of the device, and the accuracy of the system is no more compatible with the requirements.

Inefficiency effects on the particle counting depend not only on the segmentation and the dead-time of the sensors and of the readout electronics, but also on the time distribution of the particles in the beam. In general, the beam time structure is not poissonian, but particles are concentrated in bunches or bursts, depending on the extraction mechanism employed in a given accelerator. In the previous chapter, examples of the bunch structure were shown for the proton beam measured at CNAO and at the Proton Therapy Center of TIFPA. For non poissonian beams, the counting inefficiencies of each strip depend on the instantaneous particle rate inside a bunch, that could be much higher than the mean counting rate measured for time periods above the inter-bunch period.

As the time structure of the beam at a few ns level affects the counting capabilities of a monitoring device, we decided to study and develop algorithms to correct inefficiency effects and make the system more robust against particle bursts and to extend the measurable fluence rate to higher values. These algorithms, described in the present chapter, are based on the logical combination of signals from two adjacent strips, and in some cases, on assumptions on the dead-time dependence of the system. The correction algorithms have been carefully studied with simulations assuming both poissonian and bunched beams, and therefore applied to the data collected at CNAO and at the Proton Therapy Center of Trento.

5.2. Modelling of inefficiency effects

Pulse counting in random processes is always subjected to inefficiencies, due to the deadtime of the counting system. The deadtime τ (often also called "recovery time") is the minimum separation between two pulses for a correct detection of both the pulses, which depends on the intrinsic behavior of the detector (the signal duration due to the charge collection time) and on the losses in the following electronics and processing chain (amplification shaping time, sampling frequency, etc.). When the interval between two pulses is shorter than the deadtime τ, only the first pulse is detected while the second pulse is lost. In the following the loss of counts due to two signals close in time is also called "pile-up".

When the arrival times of the pulses is random, or equivalently the number of pulses in a short time interval follows the Poisson distribution, two idealized models are often considered to quantify the counting losses: the "paralyzable" model and the "non-paralyzable" model [53].

In the paralyzable (or "extending") model, if a second event arrives during the deadtime produced by a previous event, the second event is not detected and the deadtime is extended. We are confident that the sensor studied in this work behaves according to this model for the intrinsic nature of the charge collection and signal formation in silicon. An example of deadtime extension is depicted in the top part of Figure 5.1: in this example 3 over the 6 input pulses are counted, while the pulses arriving during the extended deadtime periods are not detected.

In a non-paralyzable (or "non-extending") model, the second event is not counted, but the deadtime is not extended. For example, ADC devices used in nuclear physics measurements typically have a conversion period on the order of tens of microseconds, when any further input is ignored, but it is ready to process another signal as soon as the previous conversion in completed.
The bottom part of Figure 5.1 shows an example of non-paralyzable system: in this example 4 of the 6 input pulses are detected and counted.

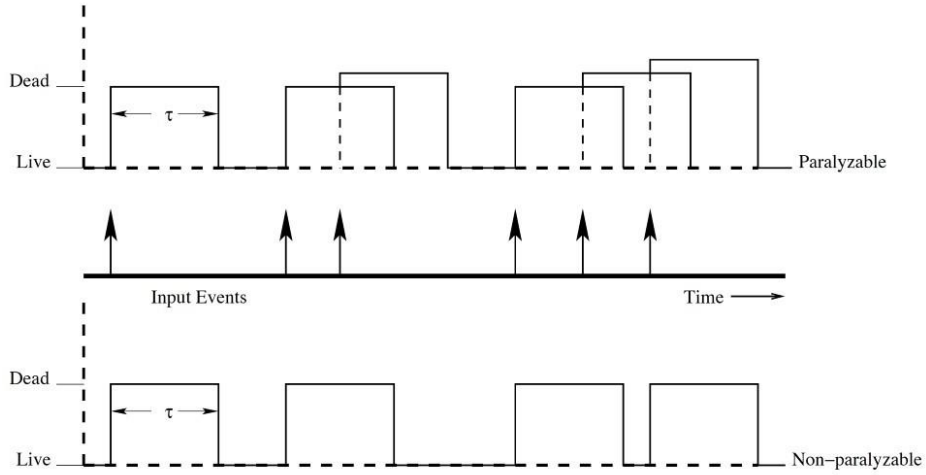

Figure 5.1 Example of deadtime behavior in a paralyzable model (top) and non-paralyzable system (bottom). The arrows indicate the time of arrival of input pulses. Pulses within the deadtime periods are not detected.

The two models describe how the number of detected pulses N_{out} depends on the number of original input pulses N_{in} and on the deadtime τ (assumed fixed), as follows:

- Paralyzable model:

$$N_{out} = N_{in} \cdot \exp(-\tau N_{in}) \quad \textbf{(5. 1)}$$

- Non-paralyzable model:

$$N_{out} = \frac{N_{in}}{1 + \tau N_{in}} \quad \textbf{(5. 2)}$$

The same equations apply to the relation between the measured counting frequency f_{out} and the input counting frequency f_{in}. The behavior of the output counting rate as a function of the input counting rate is shown in Figure 5.2 for the two models. As the name suggests, when the input rates increase, the rate of the output pulses in the paralyzable model tends to zero because the deadtime is continuously extended.

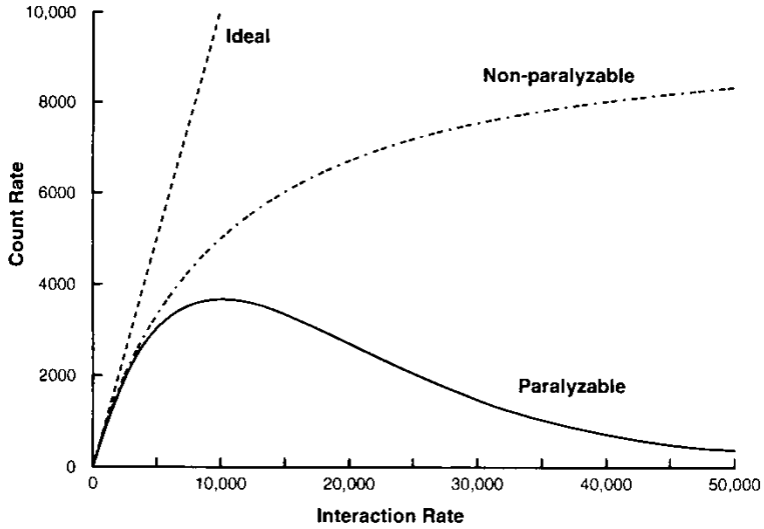

Figure 5.2 Example of the output rate vs input rate for ideal case with no count loss, for a non-paralyzable system and for a paralyzable system.

A correction algorithm for inefficiency effects could simply be based on the estimation of the system deadtime τ, and the inversion of the previous equations to estimate the number of input pulses. However, the estimation of the system deadtime is not trivial and, in addition, the system behavior could not be described by an ideal paralyzable or non-paralyzable model. Hybrid models have been introduced in the past [54] [55] [56], but they are mathematically more complex with one additional unknown parameter to be estimated.

In the following two algorithms are proposed for correction of count losses. The first algorithm (OR method) is based on number of pulses detected after the logical OR of two signals from two strips and on the assumption of ideal paralyzable or non-paralyzable models. The second algorithm (AND method) is based on the measurement of the total time duration of individual pulses from the two strips and on the time duration of pulses of the logical AND combination of the two signals. In both the cases, the two signals are assumed to be produced by two neighboring strip channels and that the time distributions of input particles in the two strips are independent.
Both the methods are intended to be applied to the system that is going to be implemented for the counting prototype described in the previous chapters, where the output current signals from two detectors are amplified and discriminated with respect to a fixed threshold. The discriminator provides an output logical signal whose duration is assumed to be equal to the time interval for which the amplified signal is over threshold. The output logical signals are therefore sampled in a FPGA with a fast clock, thus providing a

flow of two logical vectors of which the logical OR and AND combinations are performed. The pulses are detected as 0-1 transition of the logical vectors of the two channels and of their OR combination. The time duration of the input signals and of their AND combination is proportional to the number of clocks corresponding to number of 1 in the logical vector. Several counters are incremented with the number of pulses or clocks for each of the two channels or for their logical combination. A scheme of the system is shown in Figure 5.3.

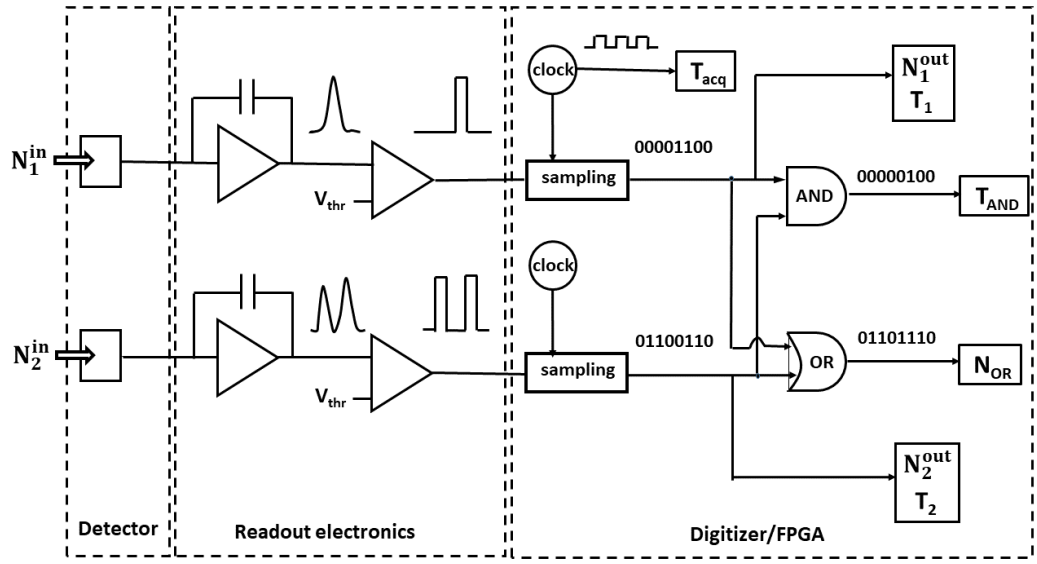

Figure 5.3 A schematic of the acquisition system for the counting device, with the logical signals from two channels sampled in a FPGA and combined in OR and AND combinations.

The quantities shown in Figure 5.3 are defined as follows:

- N_1^{in}, N_2^{in}: number of input particles in the two detector channels
- N_1^{out}, N_2^{out}: number of detected pulses in the two channels
- N_{OR}: number of pulses detected in the OR combination of the signals from the two channels
- T_1, T_2: signal duration for the signals from the two channels (number of FPGA clocks with active signal)
- T_{AND}: duration of the AND logical signal (number of clocks with active AND signal)
- T_{acq}: total acquisition time (total number of clocks).

These quantities will be used in the following sections. To describe the two correction methods, an infinite sampling frequency is assumed at the generated beginning, corresponding to a perfect measurement of all the signal durations and no pile-up effect introduced by the FPGA sampling.

5.3 The OR correction method

The OR correction method is based on the measurement of the number of output pulses from the signals of two independent detector channels, and of the number of pulses of their logical OR combination. It is assumed that the random distributions of the input times in the two channels are independent, and that the system behaves following a paralyzable model or a non-paralyzable model.
Assume that the mean number of particles arriving at the two detector channels are linearly proportional, with N_1^{in} the number of input pulses in the first channel and

$$N_2^{in} = k \cdot N_1^{in} \quad \textbf{(5. 3)}$$

the number of input pulses in the second channel

The proportionality factor k in Eq. 5.3 takes into account different geometrical acceptances of the two channels or, in case of a therapeutic beam, a different local flux due to the beam shape.

If a paralyzable model of inefficiency effects is assumed with a fixed deadtime τ, the number of detected pulses from the two channels are given by Eq. 5.1:

$$N_1^{out} = N_1^{in} \cdot \exp\left(-\tau \cdot N_1^{in}\right) \quad \textbf{(5. 4)}$$

$$N_2^{out} = N_2^{in} \cdot \exp\left(-\tau \cdot N_2^{in}\right) = k \cdot N_1^{in} \cdot \exp\left(-\tau \cdot k \cdot N_1^{in}\right) \quad \textbf{(5. 5)}$$

The OR combination of the logical signals from the two channels is equivalent to consider a single detection system with $N_1^{in} + N_2^{in}$ input pulses. The measured count of the OR signal is given by:

$$N_{OR} = \left(N_1^{in} + N_2^{in}\right) \exp\left(-\tau\left(N_1^{in} + N_2^{in}\right)\right) \quad \textbf{(5. 6)}$$

$$= (\mathrm{k}+1)\mathrm{N}_1^{\mathrm{in}} \exp\left(-\tau(\mathrm{k}+1)\mathrm{N}_1^{\mathrm{in}}\right)$$

The correction formula of the OR method for a paralyzable system is obtained by combining Equations 5.4, 5.5 and 5.6:

$$N_1^{in} = \frac{(k+1)N_1^{out}N_2^{out}}{kN_{OR}} \quad \textbf{(5. 7)}$$

The number of input particles in channel 2 can be determined from Eq. 5.4.

A similar correction formula can be obtained for a non-paralyzable system starting from Eq.5.2:

$$\mathrm{N}_1^{\mathrm{in}} = \frac{N_{OR}}{N_{OR}\left(\frac{1}{\mathrm{N}_1^{\mathrm{out}}} + \frac{\mathrm{k}}{\mathrm{N}_2^{\mathrm{out}}}\right) - \mathrm{k} - 1} \quad \textbf{(5. 8)}$$

The correction formulas of Eq.5.7 (paralyzable system) and Eq.5.8 (non-paralyzable system) do not depend on the knowledge of the deadtime τ. The value of the deadtime τ can be estimated by inverting Eq.5.4 or Eq.5.5 once the number of input counts are calculated.

In Eq. 5.7 and 5.8, the factor k is assumed to be know: in the following it is assumed to be equal to 1 for two strips with the same area and with the same input rates. In case it could be determined by comparing the measurements of counts with the two detection systems at low rates.

5.4. The AND correction method

The AND correction method employs the measurements of the time duration of the logical signals from two channels under the same radiation field, together with the time duration of their AND combination. The correction method is based on the estimation of the probability that a particle is detected (p_{det}) or lost (p_{lost}). The detection probability for channel 1 or 2 is

$$p_{det} = \frac{N_{out}^{1,2}}{N_{in}^{1,2}} \quad \textbf{(5. 9)}$$

and the probability to lose one count is given by the fraction of time the system is busy, i.e.:

$$p_{lost} = \frac{T_{1,2}}{T_{acq}} \quad \textbf{(5. 10)}$$

Where N_{in} and N_{out} are the number of input particles and of the detected pulses for channel 1 or 2, $T_{1,2}$ are the time durations of the corresponding logical signals after the discriminator, and T_{acq} is the total acquisition time. Considering that $p_{det}+p_{lost}=1$, we obtain:

$$\frac{N_{out}^{1,2}}{N_{in}^{1,2}} = 1 - \frac{T_{1,2}}{T_{acq}} \quad \textbf{(5. 11)}$$

Assuming the time distribution of input particles are completely independent, the probability to have both the detectors dead at the same time is the product of the probabilities that each detector channel is dead:

$$\frac{T_{AND}}{T_{acq}} = \frac{T_1}{T_{acq}} \cdot \frac{T_2}{T_{acq}} \quad \textbf{(5. 12)}$$

The last equation can be written as:

$$\frac{T_1}{T_{acq}} = \frac{T_{AND}}{T_2} \quad \textbf{(5. 13)}$$

Combining Eq.5.11 and Eq 5.13, the number of input particles can be estimated as:

$$N_{in}^1 = \frac{N_{out}^1}{1 - \frac{T_1}{T_{acq}}} = \frac{N_{out}^1}{1 - \frac{T_{AND}}{T_2}} \quad \textbf{(5. 14)}$$

And a similar solution can be found for the correction of the second channel:

$$N_{in}^2 = \frac{N_{out}^2}{1 - \frac{T_{AND}}{T_1}} \quad \textbf{(5. 15)}$$

It is worth to underline that this correction method does not rely on any assumption on the dead-time model being extendable or not extendable.

5.5 Validation of the correction methods with simulations

5.5.1 Simulation of ideal pulses

In order to validate the correction methods described in Sections 5.3 and 5.4, a simulation was performed by generating the time-stamps of input particles following a Poisson distribution at different frequencies f_{in}. A fixed deadtime of τ=1,5 ns was added to each pulse both with extending or non-extending

criteria to provide waveforms of deadtime distributions corresponding to the overlap of boxcar functions with unit amplitude. An example of waveform is shown in Fig. 5.4(left). The number of output pulses corresponds to the number of transitions from 0.

To take into account the effect of non-continuous beam structures, the generated input pulses can be packed in bunches, where the bunches are distributed with a period $T_{bunch}=1/f_{bunch}$ with a duty cycle DC. An example of bunched particle distribution is shown in Fig.5.4(right). The beam parameters used in the simulation of bunched beams are T_{bunch}=1 μs and DC = 0,3, and inside each bunch the particle distribution is Poissonian.

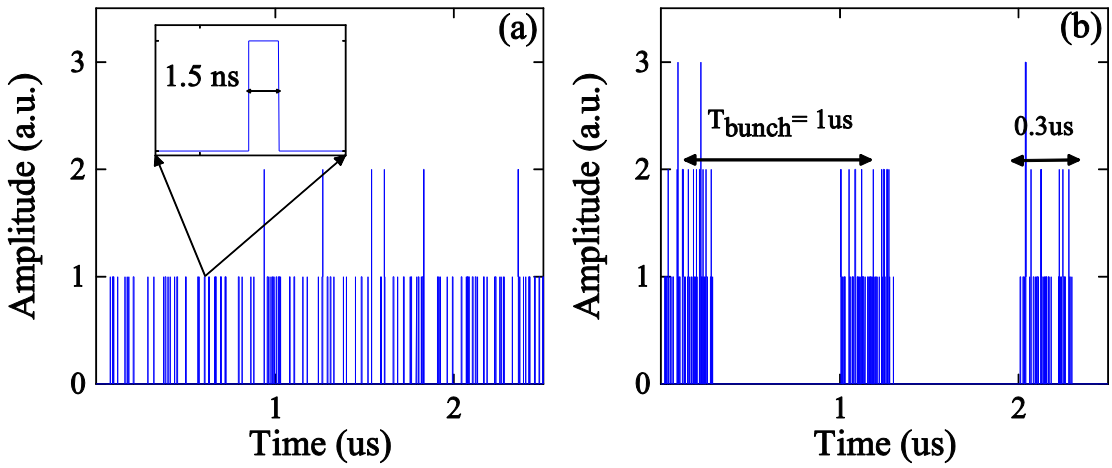

Figure 5.4 Left: simulation of an ideal deadtime waveform for a continuous beam. Right: waveform generated for a beam with a bunch structure.

For each simulation two sets of waveforms with independent probability distributions and the same beam structure (uniform or bunched) are generated, to emulate the outputs from two adjacent UFSD strips. The number of input and detected pulses from the simulated waveforms are converted in input and measured pulse rates for the two channels. Equations 5.6, 5.7, 5.14 and 5.15 are applied to the measured number of counts and pulse times to determine the particles rates corrected for pile-up inefficiencies. In the following only corrections for a paralyzable system will be shown, because the deadtime due to two overlapping signals from a silicon sensor is expected to follow an extending model. The results are shown in Fig 5.5 in terms of the products $\tau \cdot f_{corr}$ and $\tau \cdot f_{meas}$ as a function of the normalized input frequency $\tau \cdot f_{in}$ for a continuous beam (left) and a beam with a bunched structure (right). The black dashed-dotted lines are the measured normalized frequency before the corrections, the red line is the ideal case of perfect correction, the blue points are the normalized

frequencies corrected with the AND method, the red points with the OR method. A very good performance is observed for both the methods applied to a continuous beam. For the simulation of a bunched beam, the AND method works till $\tau \cdot f_{in}=1$, while the OR method fails for $\tau \cdot f_{in}>0.5$. It has to be noticed that $\tau \cdot f_{in}=0,5$ corresponds to a very high input frequency (330 MHz/channel).

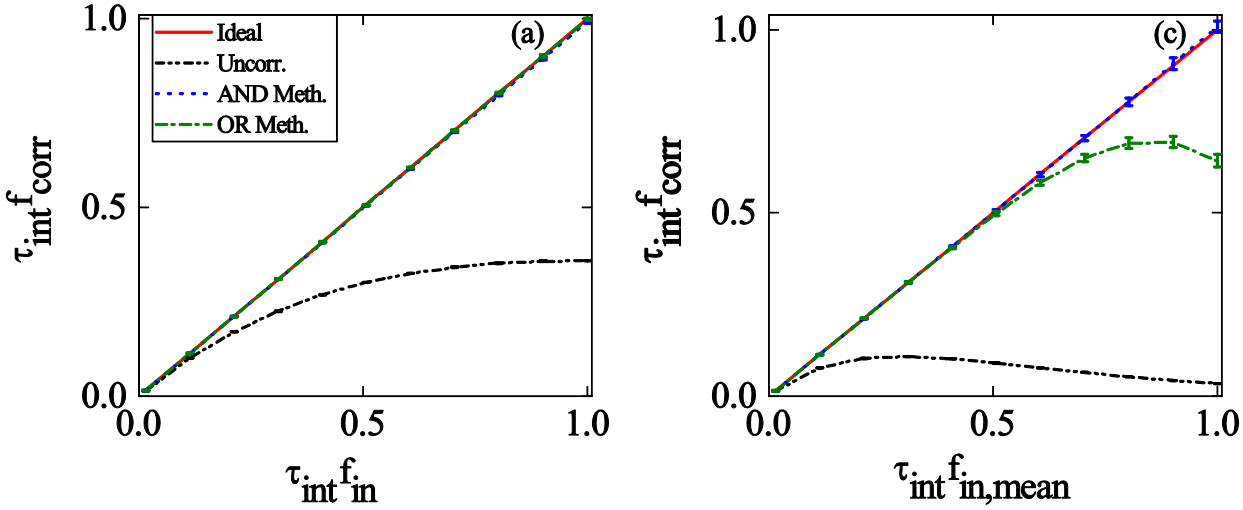

Figure 5.5 Normalized particle rates as a function of the input rate for the ideal case of no pile-up effects (red line), for the output pulses before corrections (black line) and after the corrections with the AND method (blue points and lines) and the OR method (green points and line)

The correction results are better appreciated in Fig. 5.6, where the counting efficiency ($\eta=f_{corr}/f_{in}$) after corrections with the OR (Fig.5.6(a)) and AND (Fig.5.6(b)) methods is shown as a function of the normalized input frequency for continuous and bunched beam and a paralyzable system. The factor τ used to normalize the input frequency is the intrinsic dead time of the system in case of a continuous beam (τ=1.5 ns) and the effective deadtime ($\tau_{eff}=\tau/DC$) in case of a bunched beam. The different normalization factors take into accounts the fact that inefficiency effects and their corrections depend on the instantaneous frequency in case of a bunched beam.

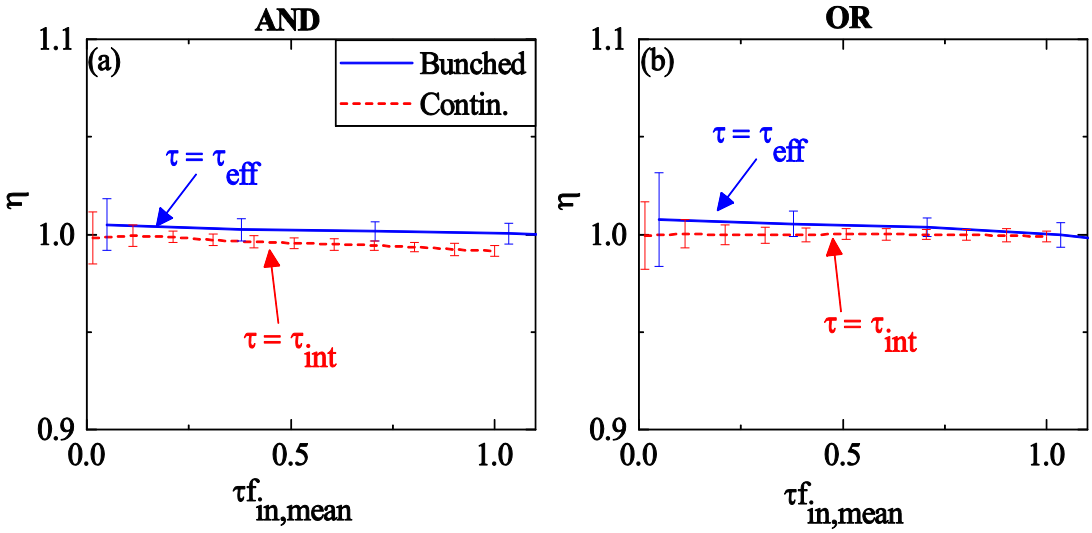

Figure 5. 6 Counting efficiency f_{corr}/f_{in} as a function of the normalized input rate for the AND method (a) and the OR method (b), continuous beam (red) and bunched beam (blue)

From Fig.5.6 it is evident that both the methods work very well in this range of input frequencies, providing a corrected frequency value close to the input particle rate within 1 %. However, in these simulations ideal pulse and deadtime conditions were considered. The following section describes the results obtained from studies with more realistic signals and pulse shapes expected from a silicon detector and simulated with the Weightfield2 package.

5.5.2 Simulation of realistic pulses from UFSD sensors

In order to check the performance of the correction algorithms with simulations of a more realistic scenario, the Weightfield2 software described in Section 2.5 was used to provide a sample of signals expected from a UFSD sensor with 50 μm thickness and gain 10 crossed by minimum ionizing particles (MIPs).

The simulation includes the effect of the Cividec broadband amplifiers employed for the tests described in the previous chapter. For each input frequency, the signals have been distributed randomly in time with Poisson distribution and two set of independent waveforms were generated to simulate the output from two UFSD strips. The waveforms were generated with a sampling frequency of 5 GHz, to simulate the sampling of the CAEN digitizer used to collect data from the UFSD strips at CNAO and TIFPA (Sect 4.3.1).

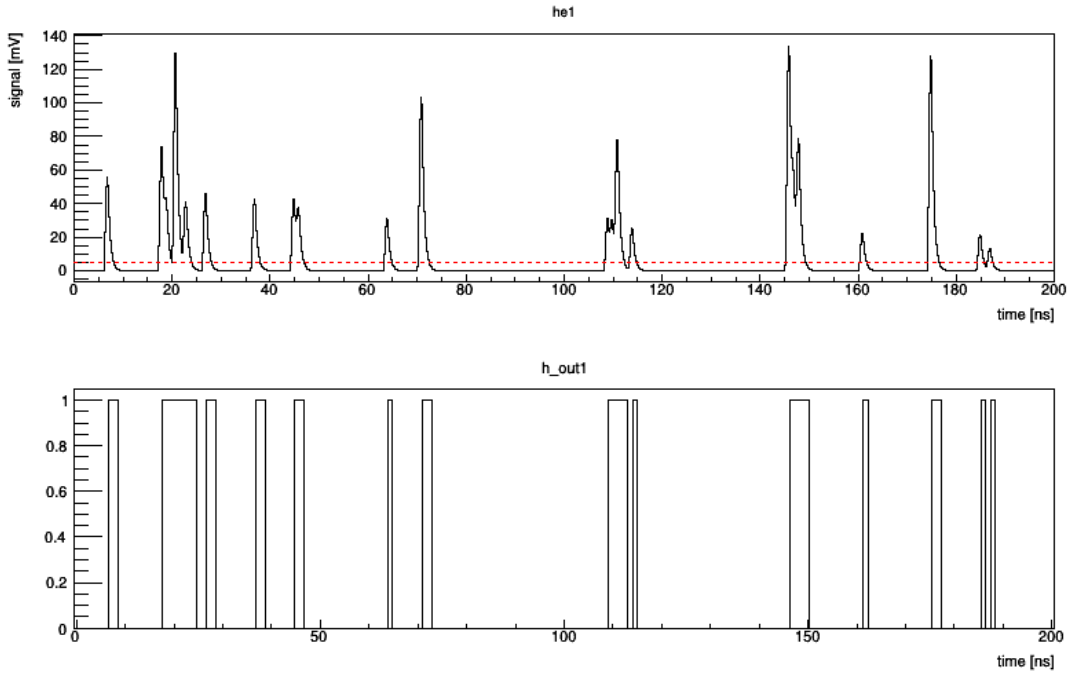

Figure 5.7 Top: a waveform of simulated signals from a 50 μm UFSD sensor at an input rate of 100 MHz. Bottom: corresponding pulses after the discriminator.

A threshold value was chosen to emulate the logical signals in output from a discriminator, assuming that the duration of each output pulse is given by the time the waveform signals are over threshold.

An example of generated signals and corresponding logical pulses after the discriminator are shown in Fig.5.7 for a 204.8 ns waveform generate with an input pulse rate of 100 MHz. The number of measured pulses corresponds to the number of logical pulses in Fig.5.7(bottom).

The amplitude distribution of the signals generated with Weightfield2 used in this simulation is shown in Figure 5.8(left), where the result from a fit with a Landau function is included. From Figure 5.8(left) it can be seen that the lowest amplitude value is 10 mV and the Most Probable Value MPV of the Landau fit is 18.08 mV.

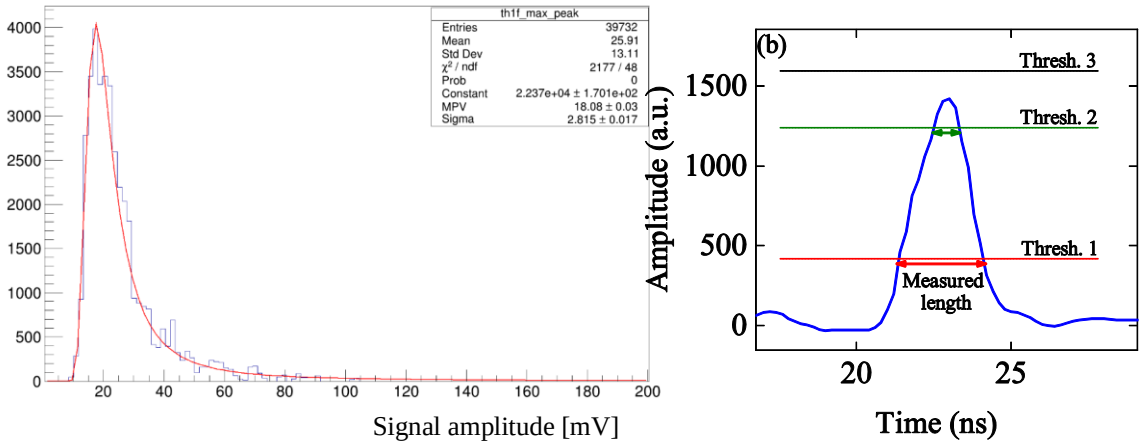

Figure 5.8 Left: amplitude distribution of the simulated signals with a Landau fit. Right: illustration of the impact of the threshold level on the signal detection and pulse duration

It is expected that the system deadtime depends on the value of the threshold. This is evident from Fig.5.8(right), where the different duration of the time over threshold are visualized for different threshold values. At high thresholds the signal is completely lost, while for low threshold levels, the output pulse from the discriminator can be affected by the signal tails. In a first approximation the noise is not included in the simulation: it will be added in a second step.

The simulation of two independent signal flows from two UFSD detectors (or two strips) with the same input rate was used to count the number of logical pulses after the discriminator and the corresponding rates (f_{meas}). The OR and AND combination of the logical pulses and all the quantities needed to apply the correction formula described in Sects. 5.3 and 5.4 are calculated (T_1, T_2, T_{AND}, N_1, N_2, N_{OR}). The same input frequency is used for the two channels and the factor k in Eq. 5.7 is therefore fixed to k=1.

The counting rates $\tau \cdot f_{out}$ obtained with the AND and OR methods are shown in Fig.5.9 as a function of the normalized input frequency $\tau \cdot f_{in}$ for different threshold levels. In the two graphs of Fig.5.9 the colored boxes and circles are the normalized counting rates $\tau \cdot f_{out}$ after the corrections, while the triangles are the normalized counting rates without corrections, with colors corresponding to different threshold values. A deadtime value of τ=1.5 ns (the typical duration of single MIP signals generated from Weightfield2 at half of their amplitude) is used to normalize the input frequency.

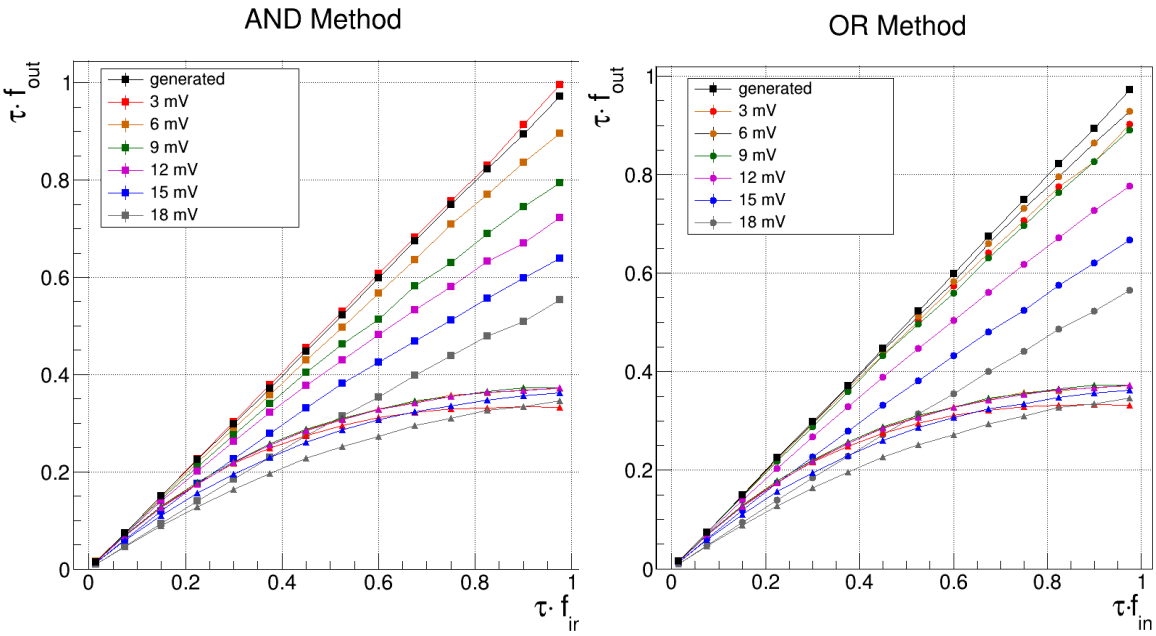

Figure 5.9 Counting rates before (triangles) and after (circles) the corrections with the AND (left) and OR (right) methods as a function of the normalized input frequency $\tau \cdot f_{in}$ for different threshold levels.

The same results are shown in Fig.5.10 in terms of counting efficiency before (f_{meas}/f_{in}) and after the corrections (f_{corr}/f_{in}) as a function of the normalized input frequency, separately for different threshold values.

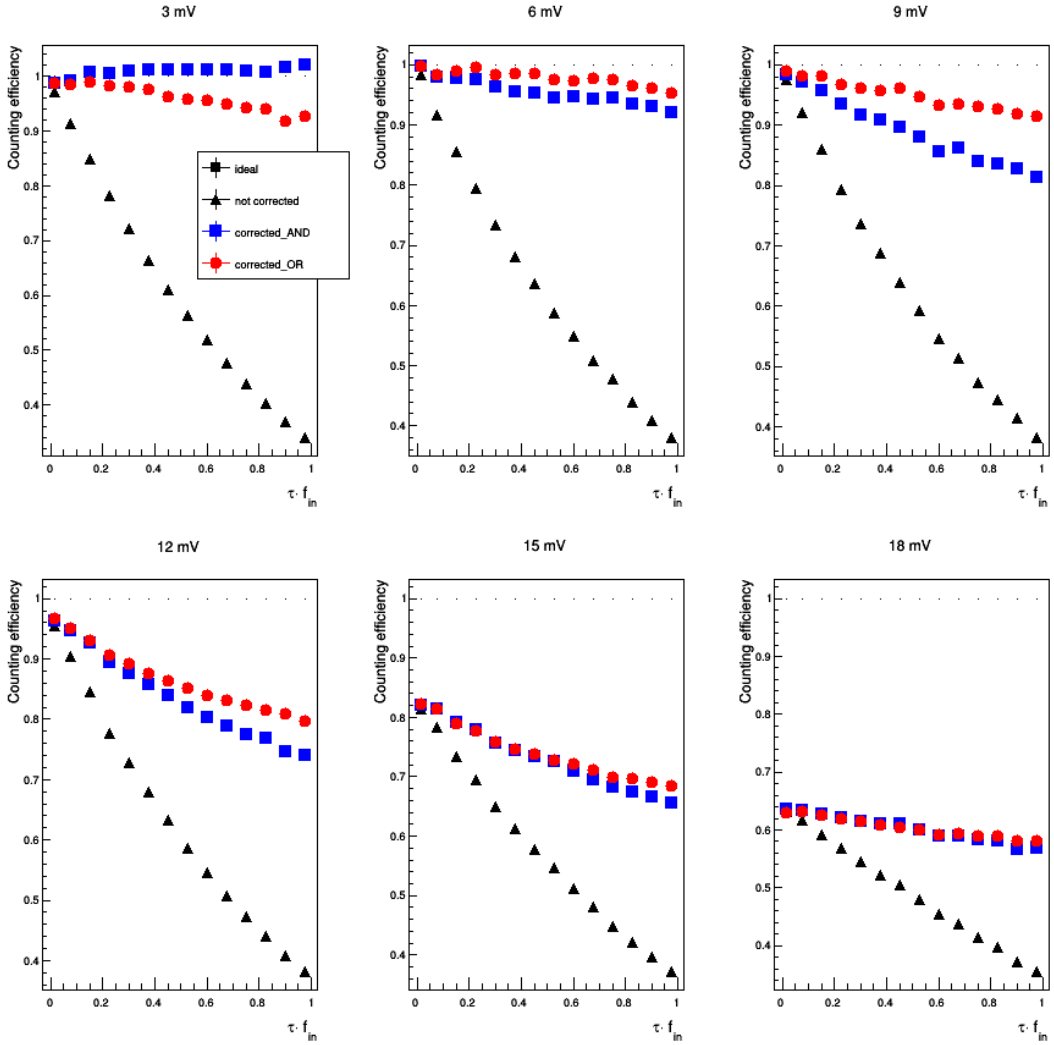

Figure 5.10 Counting efficiencies as a function of the normalized input frequency before the correction (black) and after the corrections with the AND (blue) and OR (red) methods, for different threshold values

At low threshold levels (3 mV) the AND method recovers the counting inefficiencies better than the OR method. For thresholds values greater than 6 mV the OR method looks more promising, while for thresholds equal or greater than 12 mV both the methods are not able to fully recover the count losses even at low input frequencies; this is justified by the fact that a threshold above 10 mV starts to cut some signals with amplitude below the threshold, as can be seen from the amplitude distribution used in the simulation (Fig.5.8). A reasonable threshold level for this simulation is 6 mV.

The readout system depicted in Fig.5.3 requires the acquisition of logical signals from a FPGA, where a deserializer is used to sample the input pulses at a given frequency. Therefore, the effect of the FPGA sampling frequency

on the counting efficiency is studied. The results are shown in Fig.5.11 in terms of counting efficiency dependence on the sampling frequency. In this study signals were generated in two channels with an input rate of 150 MHz (corresponding to $\tau \cdot f_{in}=0.225$), discriminated with a fixed threshold of 6 mV and the output logical pulses are sampled at different frequencies before their logical combinations and the application of the counting and correction algorithms.

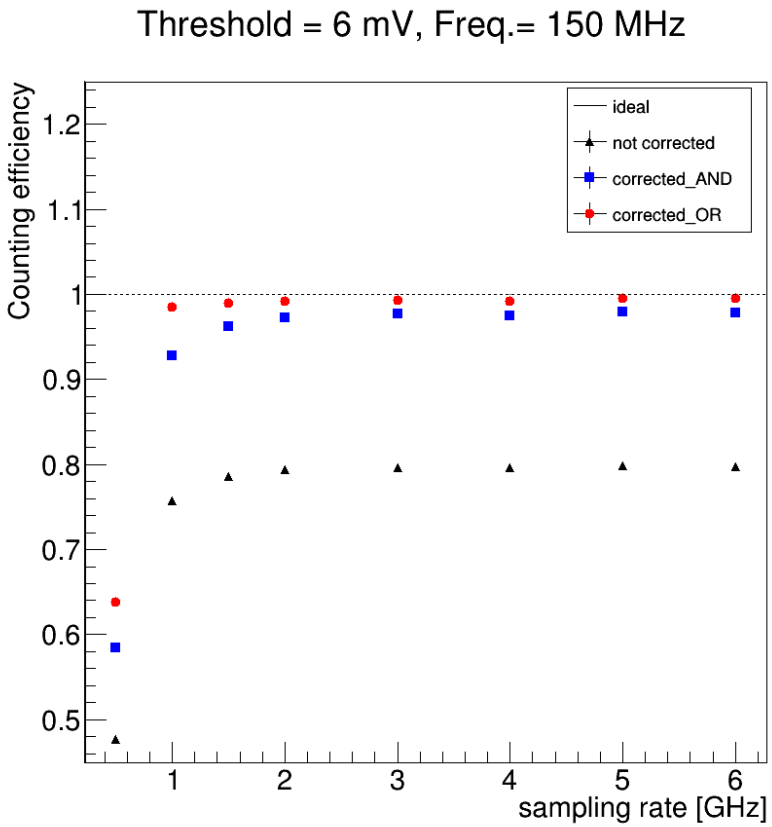

Figure 5.11 Counting efficiency as a function of the sampling rate with no correction (black) and after the corrections with the AND (blue) and the OR (red) methods

The counting efficiencies before and after corrections are stable with respect to the sampling rate for $f_{sampling}$ greater than 3 GHz. For lower sampling frequencies the performance of the recovery algorithms starts to deteriorate, in particular for the AND method. At sampling frequencies below 0.5 GHz the number of samples is not enough to identify all the pulses, and both the counting corrections fail. The OR algorithm is more solid in a readout system based on an FPGAs, which internal clock does not exceed 1 GHz.

Another problem to be taken into account in a counting system based on the logical combination of signals from two neighboring channels is the charge sharing between the two channels. For example, the electron-hole pairs

produced by a particle crossing one strip can be partially collected from the neighboring strip, and this can give rise to a pair of correlated signals in the two channels for the same particle: in particular this charge sharing effect can be produced by particles close to the edge of the strip or hitting the region between the strips. The independence of the signals from the two channels is a basic assumption for the proposed correction algorithms that can be violated if the charge sharing effect is too high.

In order to investigate how the correction algorithms are affected by charge sharing effects, the possibility to have signals in both the channels is introduced in the simulation. For each particle in one channel another signal is generated in the second channel with a probability $P_{sharing}$. The counting efficiency before and after the corrections are shown in Fig. 5.12 as a function of the charge sharing probability $P_{sharing}$. The simulated data used for this analysis were generated with an input frequency of 150 MHz and a threshold of 6 mV was applied.

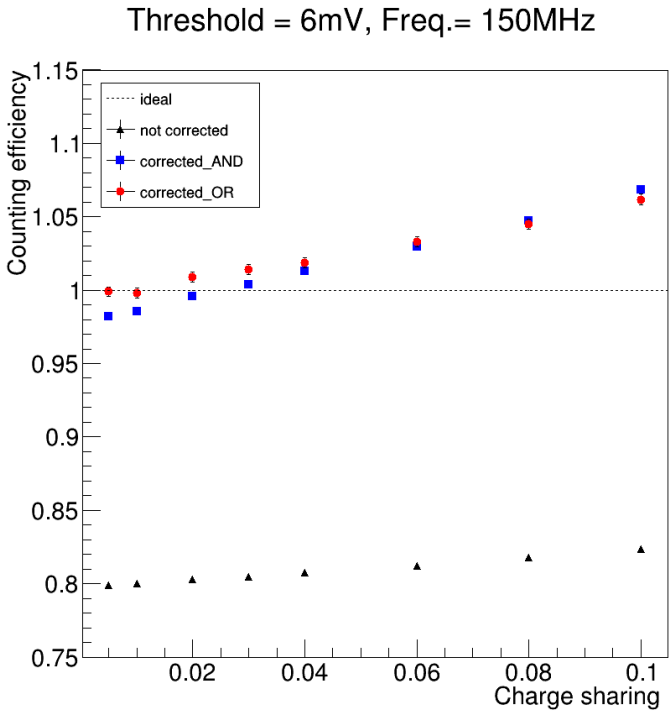

Figure 5.12 Counting efficiency as a function of the charge sharing probability (defined in the text), before the corrections (black) and after the corrections with the AND (blue) and the OR (red) methods

The number of measured counts increase with $P_{sampling}$ in both the detector channels, and the loss of independence does not allow to compensate this effect with the correction algorithms. The output frequency from the AND and OR correction methods overestimate the input frequencies when $P_{sharing}$

increased. A maximum charge sharing probability of 2% seems to be tolerable.

The last effect that was investigated and that affects the performance of the correction algorithms is related to the noise of the electronics. Fake counts due to noise spikes above the threshold are added to the number of counts from real signals, producing counting errors. A random Gaussian noise was added to the samples of the waveforms produced by the simulation, with different values of the root mean square. An example of a waveform of signals generated with a mean frequency of 100 MHz and with the overlap of a noise with rms = 3 mV is shown in Fig. 5.13.

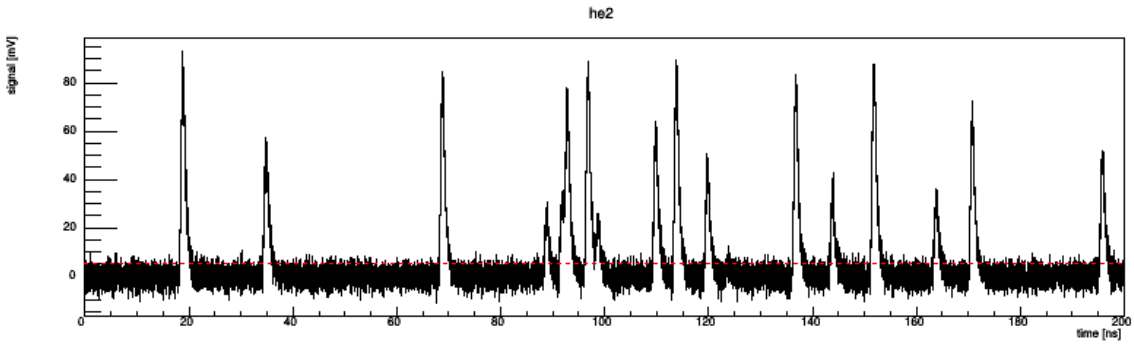

Figure 5.13 Waveform of simulated UFSD signals with the addition of a random Gaussian noise with rms of 3 mV.

The same procedure described before was applied to the waveforms with overlapped noise: a fixed threshold is used to extract logical pulses from two independent channels and the number of counts and the durations of the output pulses and of their logical combinations are used to apply the correction equations. Fig. 5.14 shows the counting efficiency before and after correction for an input frequency of 150 MHz and a threshold of 6 mV as a function of the noise rms value.

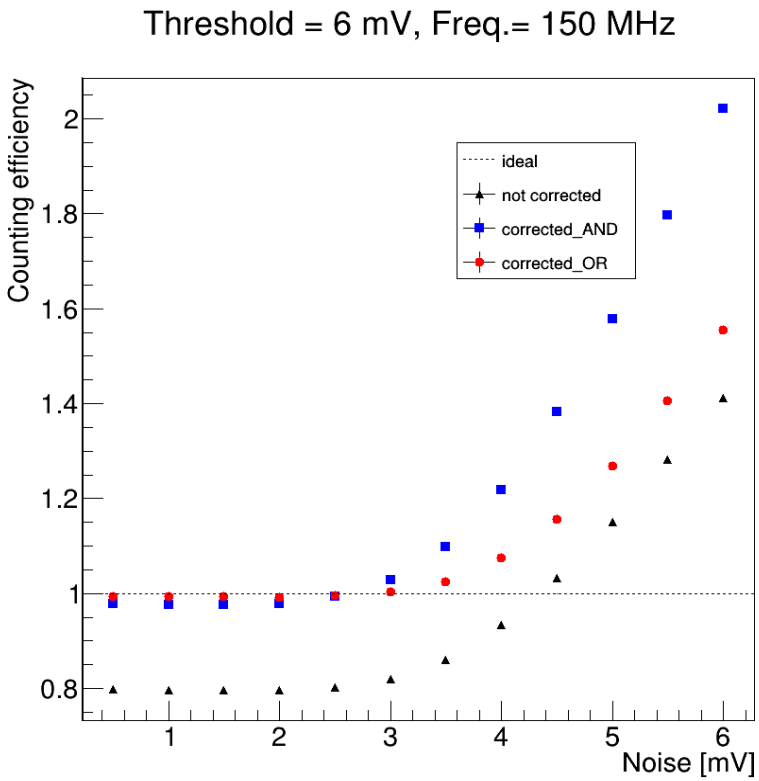

Figure 5.14 Counting efficiency as a function of the noise rms before correction (black) and after correction with the AND (blue) and OR (red) methods.

The ideal counting efficiency of 1 is recovered for both the AND and OR algorithm for a noise rms below 2.5 mV. Above this level of noise, the number of measured counts starts to increase for both the channels, and this excess of counts cannot be corrected. Taking into account the MPV value of 18 mV for the signal amplitudes used in the simulation (Fig 5.8), these results indicate that a minimum signal-to-noise level (SNR) of 7 is needed.

All the results shown above will be used for future studies and optimization of the sensors and the electronics used for beam monitoring based on single particle counting. It has to be underlined that the studies shown in this section are based on the Weightfild2 package that was already validated and proven to reproduce the signal shapes in output from the UFSD strip sensors of MoVe-IT. In addition, the readout electronics based on the ABACUS chip described in Sect.2.6 already exceeds the SNR limit acceptable for counting applications, and its output signal will be collected by a Kintex 7 FPGA with an input deserializer working with a clock of 1 GHz. Therefore, the counting system designed for MoVe-IT will be adequate to apply the correction algorithms described in this chapter and to extend its counting capabilities above the design limit of 10^8 p/cm^{2}·s of particle flux.

5.6 Application of the correction algorithms to the data collected at CNAO and PTC of Trento

The simulations described in the previous section included many parameters (threshold, noise, charge sharing, sampling frequency) influencing the counting efficiency of the system. However, it is impossible to reproduce the harsh ambient and in particular the beam structure of a therapeutic beam.

Therefore, the pile-up mitigation methods described in the previous section have been applied to the data collected with two adjacent strips of the MoVe-IT sensors at CNAO and at the Proton Therapy Center of Trento. The saturation effects due to counting inefficiency at high rates were already shown in Fig.4.16 (CNAO) and Fig.4.22 (Trento) of the previous chapter.

The results of the correction algorithms applied on the data collected at CNAO are shown in Fig. 5.15, where the particle rate and the counting efficiency are shown as a function of the input rate as measured before the corrections (black points) and after the corrections with the AND method (blue points) and the OR method (red points). Results from data collected at different energies are merged in this plot and the input rate was estimated using the charge measured with the pin-hole ionization chamber as described in Sect.4.4.4. The two red dotted lines in Fig. 5.15 corresponds to a counting efficiency of ±1.5 % with respect to the ideal case of perfect counting with efficiency equal to 1.

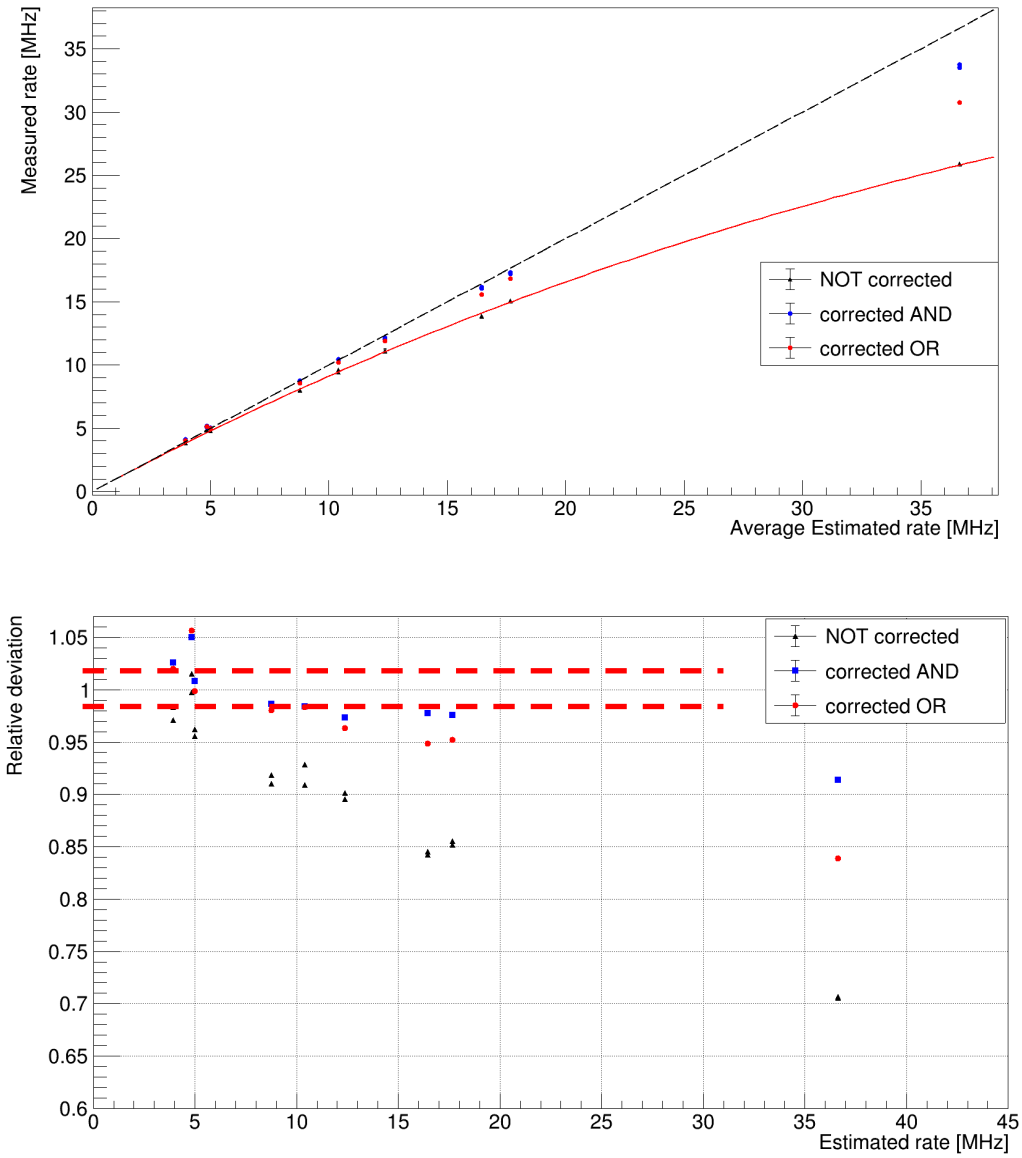

Figure 5.15 Particle rate (top) and counting efficiency (bottom) as a function of the estimated input rate before the correction (black triangles) and after the corrections with the AND method (blue points) and the OR method (red points) for data collected at CNAO.

The good performance of the mitigation algorithms is evident, and reasonable results are achieved for both the method up to a particle rate of about 10 MHz, corresponding to a local fluence rate of about $5 \cdot 10^8$ p/(cm^2·s), well above the goal of the MoVe-IT project. However, some points are outside the error bands, especially for measurements performed at high energy, for which the signal amplitude is lower, the local flux and noise higher, and the discrimination of signals from noise more difficult. In

addition, the run collected at CNAO suffered from low statistics and only three beam intensity values were available for each energy. No measurements were available at beam intensities corresponding to design flux of the counting system.

With the lessons learnt from the previous tests at CNAO, the measurements were repeated at Trento with a higher bias voltage to providing a good signal to noise ratio even with high energetic protons and extra wire bonds were added to ensure connectivity to ground and reduce the noise. In addition, at the Proton Therapy Center of TIFPA low beam intensity were available to test the counting performance at the nominal flux foreseen for MoVe-IT and data have been collected in long runs to collect sufficient statistics.

In Fig. 5.16 the difference in the number of counts measured by the two adjacent strips at the PTC of Trento is shown. A difference of about 1 % is observed, probably due to a variation of the local flux in the two strips due to the lateral beam shape. In principle a scale factor k different than 1 should be estimated and applied in Eq.5.7: however, a correction with respect to the nominal value k=1 was not applied in these analyses, because its effect on the corrected number of counts was estimated to be less than 0.5 %.

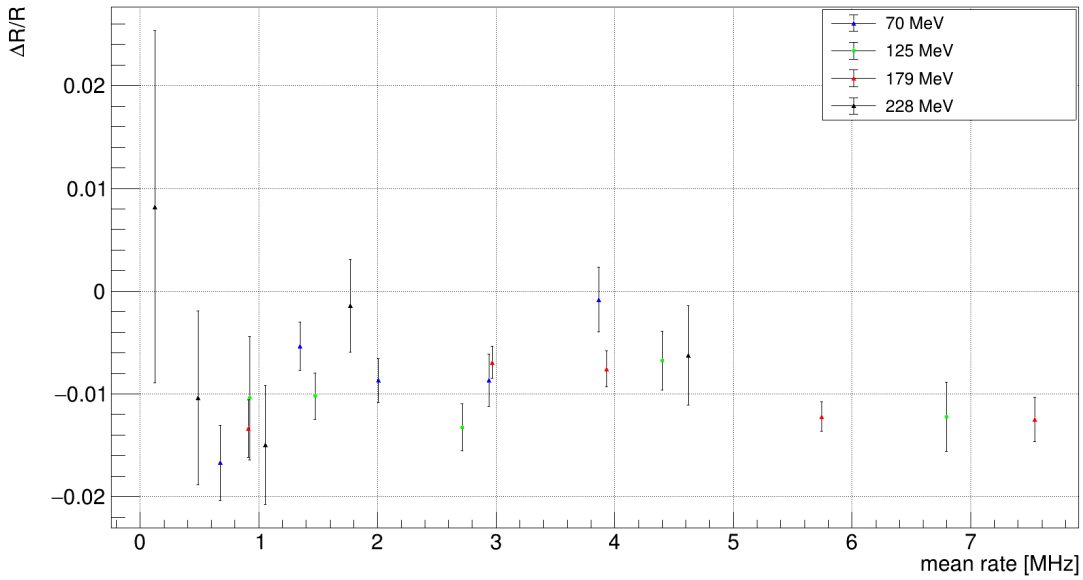

Figure 5.16 Count difference between two adjacent strips from short MoVe-IT sensor

The results of the application of the correction algorithm to the data collected at TIFPA with two strips are shown in Fig.5.17.

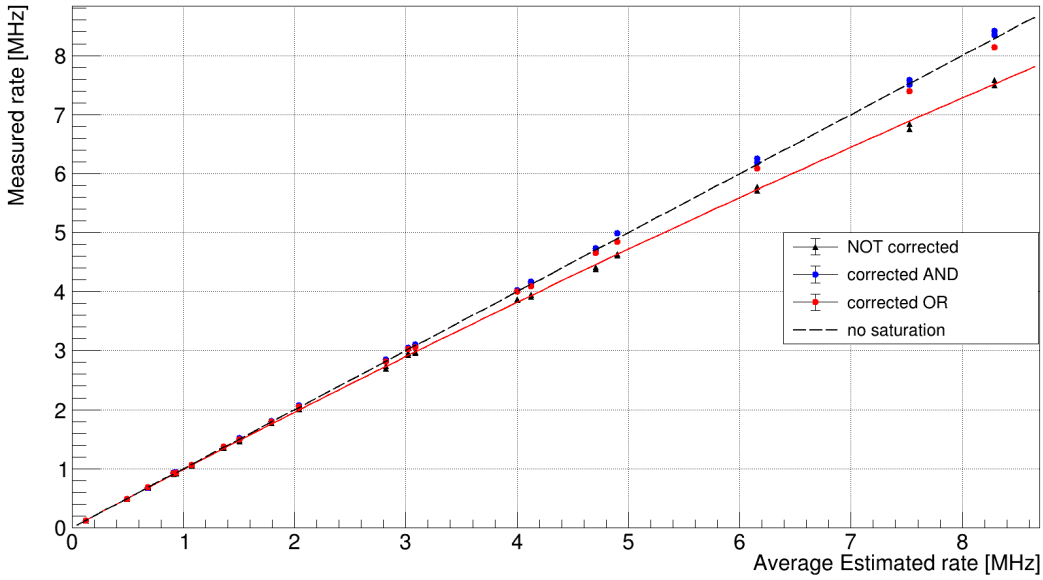

Figure 5.17 Particle rate as a function of the estimated input rate before the correction (black triangles) and after the corrections with the AND method (blue points) and the OR method (red points) for data collected at PTC of Trento

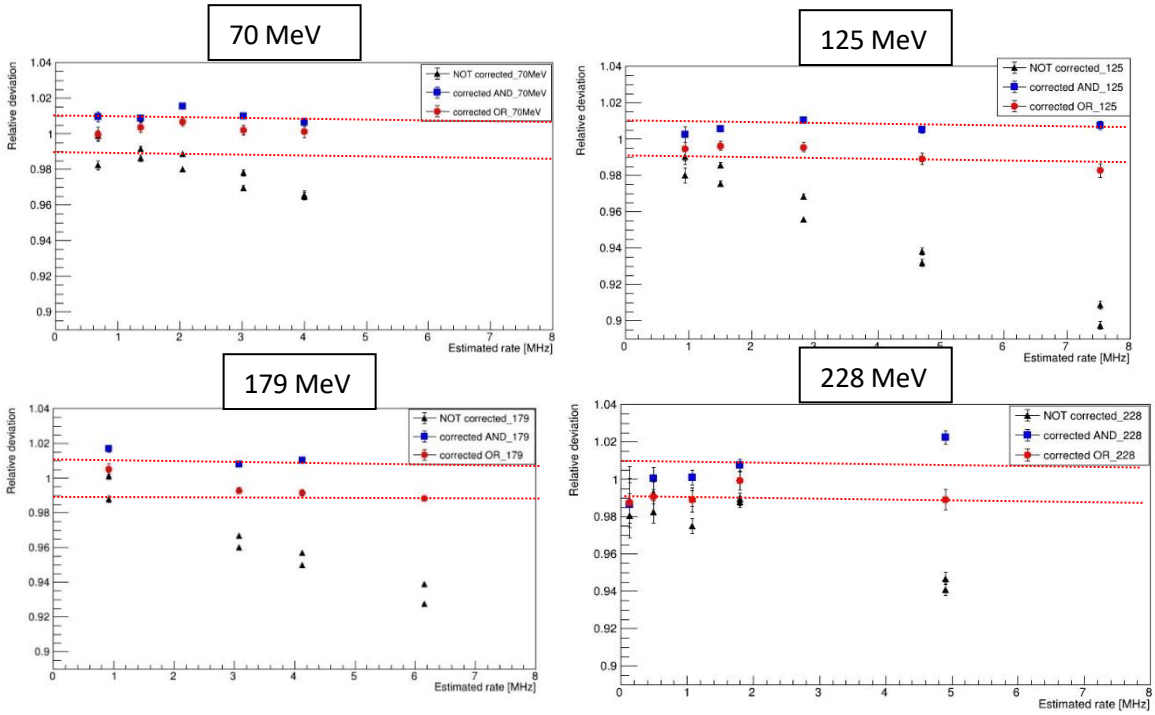

Figure 5.18 Counting efficiency as a function of the input rate for data collected at the Proton Therapy Center of Trento before the corrections (black triangles) and after the corrections with the AND method (blue points) and the OR method (red point) separately for each beam energy used in the test. The horizontal red lines correspond to a ±1 % band around the ideal case of perfect counting.

The same results are shown in Fig. 5.18 in terms of counting efficiency separately for each beam energy used in the test. A ±1 % error band with respect to the ideal case of perfect counting with efficiency equal to 1 is added. In both the figure the measured rates without correction are included as black triangles, while the corrected values are shown with blue and red points for the AND and the OR methods respectively. For the not corrected values the measurements from both the strips are reported.

The results shown in Fig.5.18 show that even without the application of pile-up corrections, the measured counting error was less than 2 % up to 2 MHz/strip, corresponding to the design flux of the MoVe-IT strip sensor of 100 MHz/(cm^2·s). After the application of the correction methods, almost all the points are within the ±1 % limits for all the energies up to 7 MHz/strip (corresponding to a flux of about 3.5x10^8 p/(cm^2·s). The OR method looks to be more robust in the correction, while the AND method tends to overestimate the number of counts at the highest energy and at highest rate, where the counting conditions are more difficult.

In conclusion, it was demonstrated that the counting system designed to monitor the irradiation beam in radiobiological experiment meets the requirements of the MoVe-IT project. Solid correction algorithms, based only on data collected by two strips without the need of a priori knowledge on the beam structure or on the system deadtime, have been developed and proven to be able to enhance the counting capacities of the device.

Chapter 6

Conclusions and future perspectives

This thesis reported the author's Doctoral research activity in the period October 2017- September 2019, performed within the medical physics group of Torino University and INFN. The activity concerned the investigation of innovative silicon detectors with controlled internal gain (named LGAD or UFSD) for their use as beam monitors in charged particle therapy. The work consisted in the testing and characterization of dedicated UFSD strip sensors in laboratory and in test beams performed at two Italian treatment facilities. In particular the author was involved in the preparation of the acquisition setup, in data collection and analysis.

The thesis work was performed within an INFN project named MoVe-IT. The MoVe-IT project is an Italian collaboration working for a cohesive upgrade of modeling and verification techniques for treatment planning in particle therapy. In particular, the Torino medical physics group is in charge of developing a detector prototype based on thin LGAD silicon detectors for single ion discrimination and counting in particle beams, to be used as beam monitor in radiobiological experiments.

The results of this thesis work demonstrated the capability of the strip sensors developed for MoVe-IT to count the number of beam particles at the designed flux of 10^8 p/(cm^2·s) with an error of about 1 %. Moreover, mathematical algorithms developed by the medical physics group of Torino and applied on the collected data have proven to mitigate counting inefficiencies due to pile-up effects and to extend the counting capability of the system to higher beam fluxes.

The construction of the prototype for particle counting will be completed in the next months to be available for monitoring of beams during radiobiological experiments at the Italian facilities by the end of 2020. At this moment a 24-channels ASIC chip (named ABACUS) dedicated for the readout of the MoVe-IT strips was produced and tested at INFN Torino. The results of the tests show that the readout chip is able to count with full efficiency up to 100 MHz/channel with acceptable noise.

The final counting prototype will cover an area of about 3x3 cm^2 with two planes of UFSD strip sensors to measure the number of beam particles and the beam profiles in two orthogonal directions. The final prototype requires

the construction of new UFSD sensors with larger area and higher number of strips. The design of the new strip sensors was already completed by FBK and the production is foreseen for the next months. A wafer layout with the 3x3 cm^2 new sensors is shown in Fig.6.1. They will have 146 strips with a pitch of 180 µm to be easily adapted to the pitch of the chip input pads. They will be produced in 12 wafers with two different doping doses, with 7 sensors hosted in each wafer where 1 additional sensor without gain layer and other smaller structures are also included.

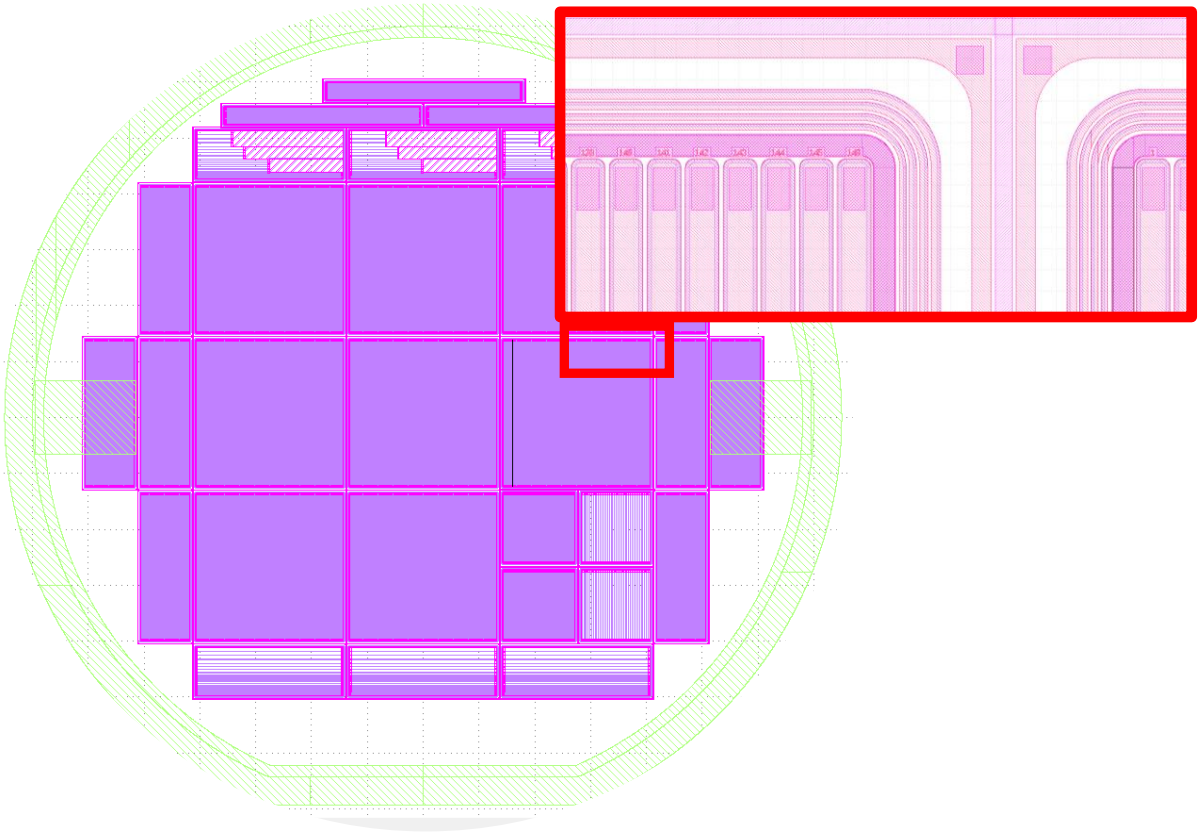

Figure 6.1 Wafer layout with the new strips sensors designed by FBK for the final prototype of beam particle counter.

In parallel, a dedicated readout board was designed by INFN Torino. The board, shown in Fig. 6.2, will host 6 ABACUS chips to connect all the 146 strips of a 3x3 cm^2 sensor positioned at the center of the board. The board will distribute the output pulses from the readout chips to 3 external FPGAs of the Xilinx Kintex 7 family, for which a firmware was already implemented to count the number of pulses and apply the correction algorithms to mitigate counting inefficiencies at high rates. The same FPGAs will manage the DACs integrated in the board and in the chip to set the discriminator thresholds.

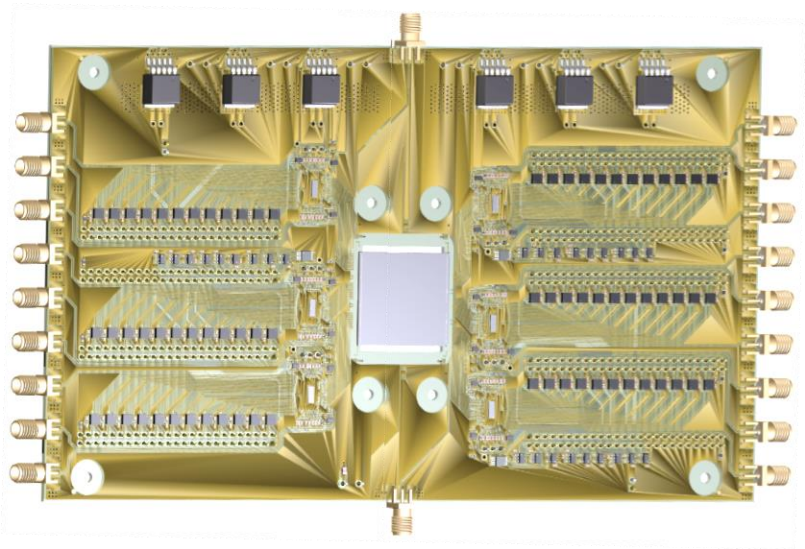

Figure 6.2 Design of the readout board for the final beam counting prototype

In addition to their applications in radiobiological experiments, the beam monitor prototype developed for the MoVe-IT project is intended to be a demonstrator for the possible future use of solid-state detectors for beam monitoring in clinical treatments with charged particles, overcoming the limitations of ionization chambers in terms of speed, sensitivity and spatial resolution.

However, this technology has to face many challenges before it can be used for clinical purposes. In particular, the typical flux of a clinical beam is an order of magnitude higher than the flux the MoVe-IT prototype based on strip sensors can achieve. To be able to count at a clinical proton flux of $10^{9} \div 10^{10}$ $cm^{-2} \cdot s^{-1}$ a smaller area is needed for each sensor channel, requiring the use of detectors segmented in small pixels. Taking into account the typical field of a monitor chamber of at least 20x20 cm^2, the number of channels will become of the order of $10^{5} \div 10^{6}$. The same number of channels is required for the electronics, that must be bump-bonded to the sensors pads, and cannot be mounted externally like in the MoVe-IT prototype. This means that the electronic chip suffers from the same radiation dose of the sensors, and that it contributes to the total thickness of the device, perturbing the beam quality for the multiple scattering in the material. In addition, a cooling system is needed to dissipate the heat produced by the readout chips. A possible solution to limit the material thickness could be to employ novel monolithic processes where the sensor and the electronics are integrated in the same wafer. The technology to build monolithic devices with standard CMOS manufacturing processes exists [57] [58], but it is still not mature enough for production of large area detectors.

Another problem to be addressed for the clinical use of silicon detectors for beam monitoring is their limited radiation resistance. It is expected that a beam monitoring device in a clinical proton therapy facility is exposed to total fluence of about 10^{15} p/cm^2 per year. The damage produced in LGAD sensors at this dose level is such to reduce its signal output due to the acceptor removal mechanism. However, the study of irradiated UFSD sensor has already improved their radiation resistance, in particular by adding carbon and with narrower gain layer profiles produced with low diffusion thermal cycles, as shown in Sect. 3.7. In addition, the signal reduction in a LGAD sensor can be compensated with the increase of the bias voltage and the breakdown voltage limit increases with the radiation dose. The possibility to cope with the increased leakage current of a detector irradiated with 10^{15} protons/cm^2 and operated at room temperature has not been studied yet.

At last, it has to be mentioned a second task of the Torino group in the MoVe-IT project, related to the development of a prototype device for the online measurement of the beam energy. In this device the energy of a proton beam is determined by measuring the time of flight for the particles to cross two sensors with well-known separating distance. Again, the high time resolution of the UFSD sensors are employed, and dedicated UFSD sensors were designed and produced for this application. The sensors were thinner to low thicknesses to minimize the multiple scattering and maximize the efficiency to detect the same particles in the two sensors placed at a large distance (of the order of 1 m). The development of the readout electronics was challenging, because a very good rise time, wide dynamic range, fast baseline restoring and small noise are required.
Even if not the subject of this thesis, the author was involved in the characterization and test of several prototypes of active electronic boards dedicated to the reading of the UFSD sensors for the energy measurement.

REFERENCES

[1] WHO report on cancer: setting priorities, investing wisely and providing care for all, 2020.

[2] Agnes Schipler and George Iliakis, DNA double-strand–break complexity levels and their possible contributions to the probability for error-prone processing and repair pathway choice, Nucleic Acids Res. 2013 Sep; 41(16): 7589–7605..

[3] M. B. a. K. P. M. Regler, Medical Accelerators for Hadrontherapy with Protons and Carbon Ions, *CERN Accelerator School, 2002. 757: p.,1-29.*

[4] Amaldi, U. and G. Kraft, Radiotherapy with beams of carbon ions. Reports on Progress in Physics, 2005. 68(8): p. 1861-1882..

[5] Degiovanni, A. and U. Amaldi, History of hadron therapy accelerators.EJMP Physica Medica, 2015. 31(4): p. 322-332..

[6] Archambeau, J.O., et al., Proton Radiation Therapy. Radiology, 1974. 110(2): p. 445-457..

[7] Ma, C.-M.C. and T. Lomax, Proton and carbon ion therapy. 2013, Boca Raton: Taylor & Francis..

[8] Kanai, T., Spot scanning system for proton radiotherapy. Medical Physics, 1980. 7(4): p. 365..

[9] Haberer, T., et al., Magnetic scanning system for heavy ion therapy. Nuclear Instruments and Methods in Physics Research Section A: Accelerators, Spectrometers, Detectors and Associated Equipment, 1993. 330(1–2): p. 296-305..

[10] Giordanengo et al., Design and characterization of the beam monitor detectors of the Italian National Center of Oncological Hadron-therapy (CNAO).

[11] Sothmann T et al. Real time tracking in liver SBRT: comparison of CyberKnife and Vero by planning structure-based γ-evaluation and dose-area-histograms. Physics in Medicine and Biology (2016) 61(4).

[12] Hartmann, F., Silicon tracking detectors in high energy physics, Nucl.Instr.Meth.A 666 (2012) 25-46.

[13] S. Vasile ; P. Gothoskar ; R. Farrell ; D. Sdrulla, Photon detection with high gain avalanche photodiode arrays,IEEE,volume45.

[14] B. DOLGOSHEIN, SILICON PHOTOMULTIPLIERS IN PARTICLE PHYSICS: POSSIBILITIES AND LIMITATIONS, The Science and Culture Series — PhysicsInnovative Detectors for Supercolliders, pp. 442-456 (2004).

[15] G. Pellegrini et al, Technology developments and first measurements of Low Gain Avalanche Detectors (LGAD) for high energy physics applications, Nucl.Instrum.Meth. A765 (2014) 12-16.

[16] N. Cartiglia, et al., Design optimization of ultra-fast silicon detectors, NIM A, vol. 796, pp. 141-148, 2015..

[17] Cartiglia et al. Beam test results of a 16 ps timing system based on ultra-fast silicon detectors, Nucl.Instr.Meth.A 850 (2017) 83-88.

[18] H. F.-W. Sadrozinski, Exploring charge multiplication for fast timing with silicon sensors, 20th RD50 Workshop, Bari, Italy, May 30 – June 1, 2012.

[19] F. Cenna et al. TOFFEE: a full custom amplifier-comparator chip for timingapplications with silicon detectors. In: Journal of Instrumentation 12 (2017).

[20] https://www.tifpa.infn.it/projects/move-it/.

[21] https://www.synopsys.com/silicon/tcad.html.

[22] M.Ferrero et al. Developments in the fbk production of ultra-fast silicon detectors. In IEEE Nuclear Science Symposium and Medical Imaging Conference, 2017..

[23] http://personalpages.to.infn.it/~cartigli/Weightfield2/Main.html.

[24] F. Cenna, et al., Weightfield2: a fast simulator for silicon and diamond solid state detector, NIM A 796 (2015) 149-153..

[25] https://geant4.web.cern.ch/.

[26] Design and characterization of a 64 channels ASIC front-end electronics for high-flux particle beam detectors - Fausti et al., Nucl Instr Meth A 867 (2017).

[27] https://www.keysight.com/en/pc-2111602/b1505a-power-device-analyzer-curve-tracer-series?nid=-32851.0.00&cc=IT&lc=ita&cmpid=zzfindb1505a.

[28] https://www.tek.com/keithley.

[29] https://www.ni.com/it-it/shop/labview/labview-details.html.

[30] https://cividec.at/electronics-C2-HV.html.

[31] https://www.nktphotonics.com/lasers-fibers/product/pilas-picosecond-pulsed-diode-lasers/.

[32] Cartiglia et al., Radiation resistant LGAD designs, Nucl.Instr.Meth.A 919 (2019) 16-26.

[33] Rossi, S., The Status of CNAO, The European Physical Journal volume 126 (2011) 78.

[34] Rossi, S., The National Centre for Oncological Hadrontherapy (CNAO): Status and perspectives. Physica Medica, 2015. 31(4): p. 333-351..

[35] S. Giordanengo M. A. Garella , The CNAO dose delivery system for modulated scanning ion beam radiotherapy, medical physics, 2016.

[36] Mirandola A1, Molinelli S1, Dosimetric commissioning and quality assurance of scanned ion beams at the Italian National Center for Oncological Hadrontherapy, 2015.

[37] https://protonterapia.provincia.tn.it/.

[38] https://iba-worldwide.com/.

[39] F.Tomassino et.al, Proton beam characterization in the experimental room of the Trento Proton Therapy facility, Nuclear Inst. and Methods in Physics Research, A 869 (2017) 15–20, p1.

[40] https://www.tifpa.infn.it/.

[41] https://www.caen.it/subfamilies/desktop-up-to-15-kv-reversible-polarity/.

[42] https://www.caen.it/products/geco2020/.

[43] https://cdn.teledynelecroy.com/files/pdf/waverunner-6zi-datasheet.pdf.

[44] https://www.caen.it/products/dt5742/.

[45] https://www.caen.it/products/a2818/.

[46] https://www.caen.it/products/caen-wavedump/.

[47] https://www.ptwdosimetry.com/en/products/pinpoint-ion-chambers-31014-31015/.

[48] https://www.ptwdosimetry.com/en/products/unidos-e/.

[49] http://rdg.imb-cnm.csic.es/.

[50] https://www.hamamatsu.com/eu/en/product/index.html.

[51] https://root.cern.ch/.

[52] (Galloway et al., Properties of HPK UFSD after neutron irradiation up to 6e15 neq/cm2, Nucl.Instr.Meth.A 940 (2019) 19-29)..

[53] S. Usman and A. Patil, Radiation detector deadtime and pile up: A review of the status of science, Nucl. Eng. Technol., 2018..

[54] J. W. Müller, Generalized dead times, Nucl. Instruments Methods Phys. Res. Sect. A Accel. Spectrometers, Detect. Assoc. Equip., vol. 301, no. 3, pp. 543–551, 1991..

[55] S. H. Lee and R. P. Gardner, A new G–M counter dead time model, Appl. Radiat. Isot., vol. 53, no. 4–5, pp. 731–737, 2000..

[56] A. Patil and S. Usman, Measurement and application of paralysis factor for improved detector dead-time characterization, Nucl. Technol., vol. 165, no. 2, pp. 249–256, 2009..

[57] Pancheri et al., A 110 nm CMOS process for fully-depleted pixel sensors, Journal of Instrumentation, Vol.14, Issue 06 (2019) C06016..

[58] GIUBILATO ET AL. MONOLITHIC PIXELS ON MODERATE RESISTIVITY SUBSTRATE AND SPARSIFYING READOUT ARCHITECTURE, Nucl.Instr.Meth. A.